ABSTRACT

Title of Dissertation DIFFUSIVE CHARGE TRANSPORT IN GRAPHENE

Jianhao Chen, Ph.D. 2009

Directed By: Distinguished University Professor,
Ellen D. Williams, Department of Physics

The physical mechanisms limiting the mobility of graphene on SiO_2 are studied and printed graphene devices on a flexible substrate are realized. Intentional addition of charged scattering impurities is used to study the effects of charged impurities. Atomic-scale defects are created by noble-gas ions irradiation to study the effect of unitary scatterers. The results show that charged impurities and atomic-scale defects both lead to conductivity linear in density in graphene, with a scattering magnitude that agrees quantitatively with theoretical estimates. While charged impurities cause intravalley scattering and induce a small change in the minimum conductivity, defects in graphene scatter electrons between the valleys and suppress the minimum conductivity below the metallic limit. Temperature-dependent measurements show that longitudinal acoustic phonons in graphene produce a small resistivity which is linear in temperature and independent of carrier density; at higher temperatures, polar optical phonons of the SiO_2 substrate give rise to an activated, carrier density-dependent resistivity. Graphene is also made into high mobility transparent and

flexible field effect device via the transfer-printing method. Together the results paint a complete picture of charge carrier transport in graphene on SiO_2 in the diffusive regime, and show the promise of graphene as a novel electronic material that have potential applications not only on conventional inorganic substrates, but also on flexible substrates.

DIFFUSIVE CHARGE TRANSPORT IN GRAPHENE

By

Jianhao Chen

Dissertation submitted to the Faculty of the Graduate School of the
University of Maryland, College Park, in partial fulfillment
of the requirements for the degree of
Doctor of Philosophy
2009

Advisory Committee:
Distinguished University Professor Ellen D. Williams, Chair
Associate Professor Michael S. Fuhrer
Assistant Professor Min Ouyang
Professor Janice E. Reutt-Robey
Professor Romel D. Gomez

© Copyright by
Jianhao Chen
2009

Dedication

To my parents Yaohui Chen and Rongsu Ren, my wife Jiangwei Cui and my daughter Yinglan (Cheryl) Chen.

谨以此文献给我的父亲陈耀辉，母亲任荣苏，我的妻子崔江薇和女儿陈颖蓝。

Acknowledgements

First of all, I’d like to express my deep appreciation to my advisor, Professor Ellen D. Williams. She is very knowlegable and very insightful, and has pointed me to the right direction many many times; she has also been very supportive of my research and has given me a lot of freedom, even when I seemed to be just wandering around (or “exploring”, so to speak) or spending too much time on side projects; in addition to guiding me through my projects, she also coached me on paper writing and presentations skills, which could be as important as doing good research; last but not least, she cared about my personal well-being as well as that of my family’s, which is a noble quality that does not usually display by busy professors.

I would also like to thank Professor Michael S. Fuhrer, from whom I learnt most of my knowledge of electronic transport, especially on graphitic systems (CNT, Graphene, etc.). His intuition has landed me in very favorable grounds as he guided me through my projects / experiments. I also benefited a lot from his hacking of the text I wrote (and the much higher quality text he put in) when we are co-authoring papers, and from the beautiful Power Point slides I borrowed for my presentations.

I’d like to thank Professor Masahiro (Masa) Ishigami, who was a postdoc in Ellen’s group, and who practically changed me from a theorist to an experimentalist. Despite having a Japanese ancestry, Masa has always put efficiency at the first place and (uncritical) quality second, which turned out to be very important in a highly competitive field. He taught me all the practical skills of doing experiments from the use of lab notebook to how to tighten bolts, from how to do e-beam lithography, how to grow Carbon Nanotube, to how to build custom parts for an experiment and how to

take measurements. He also set up the UHV transport measurement stage so that most of my works could be done, and he involved in many of the experiments I'm going to discuss in the main text as well.

I'd like to thank Dr. William G. Cullen, who is the most knowledgable person I know on ultra-high vacuum and periphery systems and any other hardware that one would ever use in our lab. He can usually solve experimental issues (in a second!) that could not be figured out in a day by, say, two Ph.D. students, and he will usually have the best way to implement an experimental idea I have. Despite the fact that helping graduate students and fixing equipments that nobody else can fix have taken up a lot of his time, Bill has managed to do serious scientific research, with the latest work I proudly collaborated.

I'd also like to thank Chaun Jang, who is a graduate student from Michael's group. He started doing experiments one year later than me but he coauthored most of the paper I wrote. He has the curious ability to produce a lot of graphene samples in a short period of time, without whom many of my experiments would have progressed much slower. He is usually working in a faster pace which often reminds me to speed up. He is also very easy to work with and has been upbeat most of the time, which helps a lot especially in a bad day.

I'd like to thank Shudong Xiao, who is a graduate student from Michael's group and who has provided me with a single layer graphene sample in time of great need. We also shared similar experiences outside of research, such as the hardship to take care of a baby as a graduate student.

I'd like to thank Dr. Brad Conrad, who was same year graduate student with me and with whom I spent the same four years in the same group. It is always reassuring to have someone that knows definitely when the group meeting is going to happen or what most stuff in the lab is (if Bill was not in). And I have never need to worry about organizing group party as long as Brad was around. Brad has also been very helpful when I need any other helps.

In order to be able to finish my thesis on time, my acknowledgement to the rest of the people will be disproportionally and unfairly shortened which I do apologize. I'd like to thank Dr. Daniel R. Hines for teaching me (and allowing me) to use the transfer printing machine, and help with device making. I'd like to thank Dr. Vince Ballarotto for his help in my ongoing project. I'd like to thank Mahito Yamamoto for his great gift of diapers and for being a good helping hand. I'd like to thank Dr. Shaffique Adam, Dr. Euyheon Hwang, Dr. Enrico Rossi for stimulating discussions and share of theoretical insights. I'd also like to thank the rest of the Williams group and the rest of the Fuhrer group for being nice to me and offered to help whenever I needed. And I'd like to extend my appreciation to all my friends which have made my graduate experience much more rewarding.

Table of Contents

Dedication ii
Acknowledgements iii
Table of Contents vi
List of Figures vii
Chapter 1: Introduction: from graphite to graphene 1
Chapter 2: Graphene: relativistic Dirac Fermions in two dimensions 5
2.1 Graphene and its band structure 5
2.2 Charge transport in graphene: early experiments 10
Chapter 3: Theories of carrier scattering in graphene 15
3.1 Charged impurities 15
3.2 "White-noise" disorder 17
3.3 Vacancy Defects 17
3.4 Corrugations of the graphene sheet 18
3.5 Phonons 19
Chapter 4: Experimental techniques 21
4.1 Graphene Field Effect Device Fabrication 21
4.2 The Helitran ultra-high vacuum compatible LT-3B open cycle cryostat 24
4.3 The JEOL ultra-high vacuum scanning probe microscope 28
4.4 The Transfer-printing technique 32
4.5 Transport measurements and experimental setup in ultra-high vacuum 35
Chapter 5: Charged impurity scattering in graphene 40
Chapter 6: Defect scattering in graphene 55
Chapter 7: Phonon scattering and performance limits of graphene on SiO_2 67
Chapter 8: Printed graphene circuits 80
Chapter 9: Summary and future outlook 90
9.1 Summary 90
9.2 Future outlook 92
A1: Atomic structure of graphene on SiO_2 95
A2: Corrugation effects of graphene on SiO_2 106
A3: Tuning the effective fine structure constant in graphene 109
A4: Supplementary information for Chapter 6 121
A5: Supplementary information for Chapter 7 124
Bibliography 127

List of Figures

2.1.1 The honeycomb structure of graphene lattice ... 6
2.1.2 The tight-binding band structure of graphene ... 7
2.1.3 1D schematics of the graphene energy band near the K point ... 9
2.2.1 Conductivity of graphene as a function of the back gate voltage. ... 11
2.2.2 Resistivity, carrier density and mobility of graphene vs. gate voltage ... 12
2.2.3 The "universal" minimum conductivity ... 13
2.2.4 Variations of minimum conductivity for different graphene samples ... 13
2.2.5 Correlation between lower mobility, larger threshold shift, and broader plateau ... 14
2.2.6 Schematics of the transport characteristic of graphene ... 14
4.1.1 Optical Micrograph of exfoliated graphene layers on 300 nm thick SiO_2 substrate ... 22
4.1.2 Optical Micrograph of a patterned exfoliated graphene device on 300 nm thick SiO_2 substrate ... 22
4.1.3 Three dimensional schematic of a graphene field effect device ... 23
4.1.4 Micro-Raman spectra of a single layer graphene ... 24
4.1.5 A graphene device before and after removal of PMMA residue ... 25
4.2.1 The LT-3B ultra high vacuum compatible cryostat ... 26
4.2.2 The assembly drawing of the LT-3B cryostat with dimensions ... 28
4.2.3 Schematics of the internal structure of the LT-3B ultra high vacuum compatible cryostat ... 28
4.3.1 The JEOL ultra-high vacuum scanning probe microscope ... 30
4.3.2 The viewport look of the measurement stage of the JEOL SPM ... 31
4.3.3 SEM micrograph of the AFM/STM tip over a graphene field effect device ... 32
4.4.1 The NX-2500 Imprintor from Nanonex Inc ... 33
4.4.2 The schematics of the transfer printing method ... 34
4.4.3 Procedure for making flexible and transparent graphene field effect device ... 35
4.5.1 Schematics of a DC measurement of the electronic properties of graphene ... 37
4.5.2 Schematics of a quasi-DC measurement of the electronic properties of graphene ... 38
4.5.3 Schematics of experimental setup for in situ electronic transport measurement in ultra-high vacuum ... 39
5.1 Optical micrograph and Raman spectrum of a graphene device ... 41
5.2 Potassium doping of graphene ... 43
5.3 Inverse electron mobility $1/\mu_e$ and hole mobility $1/\mu_h$ vs. doping time ... 45
5.4 Shift of minimum conductivity point with doping ... 46
5.5 Change in behavior near minimum conductivity point with doping ... 49
6.1 Raman spectra for pristine and irradiated graphene ... 58
6.2 Conductivity vs. gate voltage curves for pristine and irradiated graphene ... 59
6.3 Inverse mobility and density-independent resistivity vs. ion dosage ... 61
6.4 $|\Delta V_{g,min}|$ and σ_{min} vs mobility ... 62
6.5 Temperature dependence of the conductivity of pristine and irradiated graphene ... 65

7.1 Temperature-dependent resistivity of graphene on SiO_2 68
7.2 Room temperature performance limits of graphene on SiO_2 74
7.3 Temperature dependence of the mobility in graphene and graphite 76
8.1 Schematics of printing procedure and the printed graphene device 81
8.2 Optical and atomic force micrograph of graphene on SiO_2 and
optical micrograph of printed graphene device 84
8.3 Conductivity of printed graphene device vs gate voltage 86

Chapter 1: Introduction: from graphite to graphene

Graphite, the most prevalent allotrope of carbon, has been a very important industrial material [1-3], and a subject of scientific research for a long time [4, 5]. The layered crystal structure and the highly delocalized π electrons make graphite one of the best lubrication materials and a very good conductor. The same structure also makes graphite and its derivatives, such as graphite intercalated compounds, a quasi-two-dimensional electronic system that is of great scientific interest [6-11]. Synthetic graphite such as highly ordered pyrolytic graphite (HOPG) provides a highly ordered and inert surface (the (0001) surface) which has been a perfect substrate to study two-dimensional phase transitions [12, 13], adsorptions [14] and electronic structure of organic molecules [15]. A single layer of graphite, graphene, which has been predicted to have peculiar electronic and mechanical properties, has been used as a theoretical model to understand the properties of graphite for sixty years [6-8]. However, free standing graphene sheet, which is supposedly a two-dimensional (2D) crystal and thus thermodynamically unstable [16-18], was not expected to be found in isolated form[1].

Monolayer graphene which is strongly bonded to a substrate, however, is not subject to the thermodynamics arguments for 2D crystals and can indeed exist [19-21]. The general method to synthesize ultra-thin graphite, which could be down to one atom layer thick, mimics one of the natural processes of graphite formation, e.g., self-assembly of carbon atoms on a catalytic surface such as the surface of Ni, Pt, a

[1] Such argument (that graphene was not expected to exist) was not found before 2004, when the first graphene devices were made.

transition metal carbide, or silicon carbide, with a suitable temperature maintained [21]. The source of carbon atoms can be from above the surface or below. The former case is a chemical vapor deposition process (CVD), in which a carbon-containing stock gas, such as benzene, ethane and methane undergoes a dehydrogenation process on the catalytic surface and the carbon atoms rearrange into a honeycomb lattice [20, 22]. The latter case is a segregation process in which carbon diffuse from the bulk to the surface of the substrate [23]. The merit of the CVD method is that the growth rate of graphene is lowered by 1/10 – 1/100 once the first layer is formed and the catalytic surface largely passivated, which makes it possible to obtain a single layer of graphene; the carbon segregation method inevitably results in multilayer graphene [23, 24]. The drawback of both methods is that strong graphene-substrate interaction has an enormous impact on the electrical properties of graphene and, in the case of metallic substrates, precludes the realization of a graphene device.

To the surprise of the scientific community, it was recently discovered that graphene can be extracted from bulk graphite and be deposited on the surface of potentially any bulk material (crystalline or amorphous) with which it has only van der Waals interaction [25]. The graphene crystal can even be partially suspended, given that at least part of its edge is bonded to a substrate [26-28]. The weak graphene-substrate interaction makes it possible to retain some intrinsic characteristics of graphene, such as its band structure, its mechanical strength, etc. The potential choice of substrate makes it possible to fabricate field effect devices, mechanical resonators, photonic devices, etc. with various configurations. The high

charge carrier mobility [27], high intrinsic mechanical strength [29], and the strong interaction of electrons in graphene with incident photons [30] make graphene a very promising device material. Thus graphene has spurred enormous interest in the scientific and technical communities and explosively increasing research efforts in fabrication, isolation, characterization and application of the novel material.

Among the various novel properties of graphene, the exceptional carrier mobility of the electronic material has attracted the most attention. Much of the interest has arisen from the prospect of fabricating graphene into high speed electronic devices. However, to date, graphene devices fabricated on silicon dioxide substrate have shown field effect mobilities ranging from 0.1 to 2 m^2/Vs [31], much lower than the carrier mobility in its parent material (typically Kish graphite or highly ordered pyrolytic graphite), which have mobilities close to 100 m^2/Vs at low temperature [32]. Understanding the scattering mechanisms that limit device performance is thus of vital importance. In this work, the various possible charge scattering sources in graphene are investigated by the controlled addition of different types of scatterers to cleaned exfoliated graphene devices on SiO_2 substrate in UHV and the measurement of the changes in the transport properties of graphene *in situ* [33-36]. Using the results, the relative contributions of these scattering sources to the conductivity σ

$$\sigma^{-1} = \sigma_{ci}^{-1} + \sigma_{sr}^{-1} + \sigma_{mg}^{-1} + \sigma_{LA}^{-1} + \sigma_{PO}^{-1} + \sigma_{corr}^{-1} \tag{1.1}$$

are determined. In equation 1.1 the subscripts indicate the contributions due to charged impurities (ci), short-range scatterers (sr), midgap states (mg), longitudinal

acoustic phonons (LA), polar optical phonons (PO) and surface corrugations (corr). The results reveal the path for improving the mobility of substrate-bound graphene.

Transferring weakly-bound graphene from one substrate to another provides a completely new way to manipulate graphene and control the charge carrier scatterers in the graphene device [37]. The realization of high mobility graphene devices on flexible substrates shows exciting application possibilities of the novel electronic material [37].

In Chapter 2, the band structure of graphene and its implications are discussed and early experimental results in the transport properties of graphene are briefly reviewed. Chapter 3 describes the theories on various possible scattering sources in graphene. Chapter 4 lays out the experimental techniques in this work. Chapter 5 is devoted to the effect of charged impurities in graphene [34]. Chapter 6 presents a study of charge scattering by lattice defects induced by low energy incident ions [33]. Chapter 7 covers the effects of phonons in graphene as well as the effects of polar optical phonons on the surface of the SiO_2 substrate [35]. Chapter 8 demonstrates a high mobility graphene field effect device printed on a flexible substrate [37]. Chapter 9 is the summary. The study of atomic structure of graphene on SiO_2 is shown in Appendix A1 [38]; Appendix A2 shows the estimate of possible effect of surface roughness in scattering electrons in grahene, using data from A1 [36, 38]; the effects of dielectric screening are shown Appendix A3 [39], which shows that increase dielectric screening leads to an increase in conductivity caused by Coulomb scattering and a decrease in conductivity due to short-range scattering.

Chapter 2: Graphene: relativistic Dirac Fermions in two dimensions

2.1 Graphene and its band structure

Graphene consists of a single layer of carbon atoms arranged in a honeycomb lattice, with two sublattices, illustrated as two different types of dots in Figure 2.1.1 [40]. The grey area in Figure 2.1.1 is the extended Brillion zone (BZ). Each carbon atom has four atomic orbitals involved in bonding with the other carbon atoms in the graphene plane. The *2s*, $2p_x$ and $2p_y$ orbitals hybridize to form three sp^2 orbitals, while the $2p_z$ orbital which is perpendicular to the graphene surface remains essentially unchanged. Thus graphene has six σ bands (three bonding and three anti-bonding bands) formed by the sp^2 orbitals, and two π bands (the π band and the π* band) formed by the $2p_z$ orbital. The π bands are much closer to the Fermi surface than the σ bands, thus determining the transport properties of graphene. The subsequent discussion of band structure of graphene includes only the π bands.

A simple tight-binding calculation gives the graphene band structure as (consider only nearest neighbor hopping of the theory in Ref. [6])

$$E(k_x, k_y) = \pm\gamma_1\sqrt{1 + 4\cos(\frac{3a_0k_y}{2})\cos(\frac{\sqrt{3}a_0k_x}{2}) + 4\cos^2(\frac{\sqrt{3}a_0k_x}{2})}\,, \qquad (2.1)$$

where a_0 = 1.42Å is the nearest neighbor distance, and γ_1 = 2.9 eV is a constant from first order perturbation [40]. The calculated band structure is shown in Figure 2.1.2(a). The peculiar feature of such a band structure is that, near the *K* points, which are at the corners of the First BZ, the valence band and the conduction band

form two cone-like structures, with the tip of the two cones touching each other at the *K* points (Figure 2.1.2(b)). This creates a zero-gap semiconductor with linear dispersion relation near the *K* points. In undoped graphene, the electrons just fill up the valence band (the blue part of the cones in Figure 2.1.2(b)), resulting in zero area of the Fermi surface.

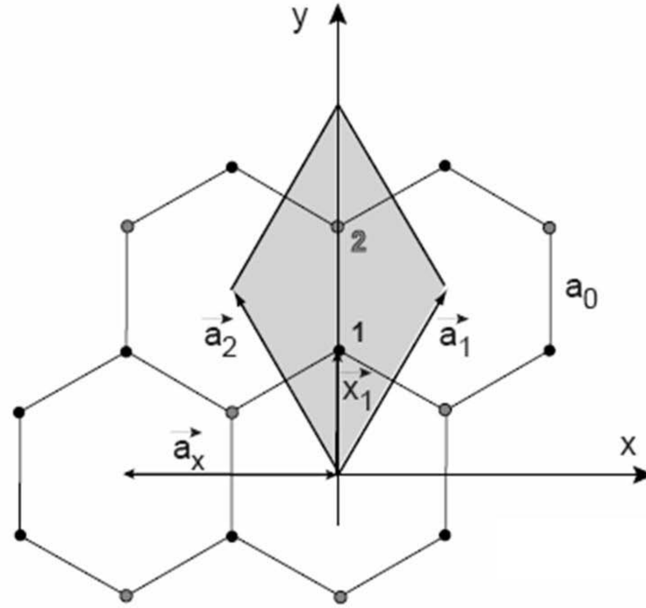

Figure 2.1.1 The honeycomb structure of graphene lattice. The solid black dots and the hollow grey dots represent two equivalent sublattices. $a_1 = a_0\sqrt{3}(1/2, \sqrt{3}/2)$ and $a_2 = a_0\sqrt{3}(-1/2 + \sqrt{3}/2)$ is the lattice vector of the graphene, where a_0=1.42Å is the nearest neighbor distance. Figure form Ref. [40].

Near the *K* and *K*' point ($|E_F| < 1$ eV), electronic states can be described by the Dirac-like Hamiltonians, equation 2.2a (near *K* point) and equation 2.2b (near *K*' point), respectively [41, 42]

$$H = \frac{hv_F}{2\pi}\begin{pmatrix} 0 & k_x - ik_y \\ k_x + ik_y & 0 \end{pmatrix} = \frac{hv_F}{2\pi}\sigma \bullet \vec{k}\,, \tag{2.2a}$$

$$H = \frac{hv_F}{2\pi}\begin{pmatrix} 0 & k_x + ik_y \\ k_x - ik_y & 0 \end{pmatrix} = \frac{hv_F}{2\pi}\sigma^* \bullet \vec{k}\,, \tag{2.2b}$$

where $v_F = \frac{3\pi\gamma_1 a_0}{h} \approx 10^6\, m/s$ is the Fermi velocity, $\vec{k}$ is the quasi-particle (the charge carrier quantum, given by a point in the dispersion relation) momentum, σ is the 2D Pauli matrix and σ^* is the complex conjugate of the 2D Pauli matrix.

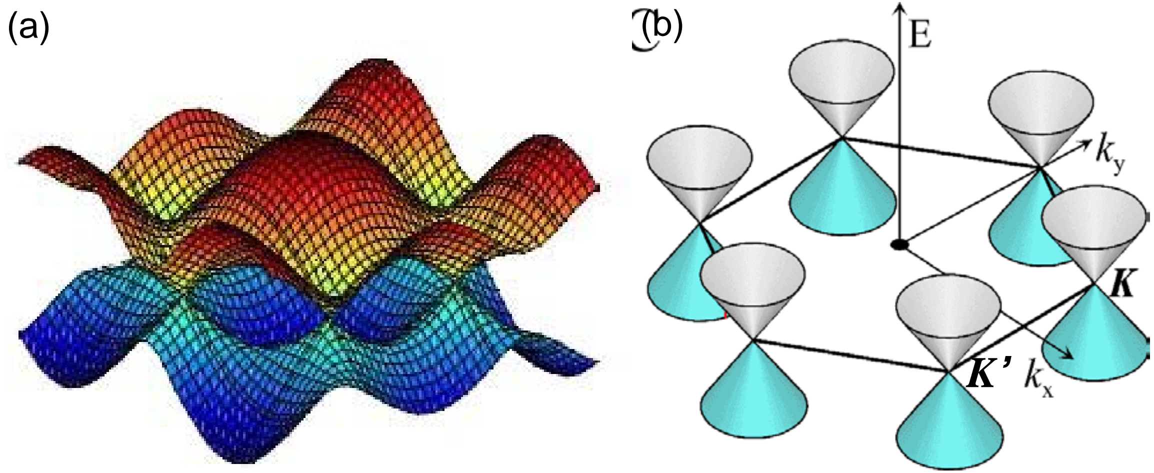

Figure 2.1.2 (a) The tight-binding band structure of graphene. (b) The close up of the band structure in (a) at the *K* points, where is the Fermi level lies. Because the linear dispersion relation near these *K* points is described well by the Dirac equation, these *K* points are also called the "Dirac points". Note that the two sublattices in graphene give rise to two distinct *K*-cones (named *K* and *K*' cones.).

The eigenvectors of such Hamiltonians can be written as

$$\left|k\right\rangle = \frac{1}{\sqrt{2}} e^{i\vec{k}\bullet\vec{r}} \begin{pmatrix} -ibe^{-i\theta_k/2} \\ e^{i\theta_k/2} \end{pmatrix} \tag{2.3a}$$

$$\left|k\right\rangle = \frac{1}{\sqrt{2}} e^{i\vec{k}\bullet\vec{r}} \begin{pmatrix} ibe^{i\theta_k/2} \\ e^{-i\theta_k/2} \end{pmatrix} \tag{2.3b}$$

where b = 1 for electrons and -1 for holes, and θ_k is the angle of the momentum of the quasiparticle with respect to the Y-axis in Figure 2.1.2(b). From equation 2.3 it is apparent that the electrons possess a two-component vector that determines the amplitude of the electronic wave function on the two sublattices atoms. This vector can be viewed as a "pseudospin", in analogy to the two-component spinor describing the electron's physical spin. A closer look at equation 2.3 reveals that the pseudospin is tied to the k vector such that one could define the direction of the pseudospin as having a fixed angle with respect to k, in which the angle is usually set to zero for states around the K point and π for states around the K' point. The concept of the pseudospin facilitates arguments for selection rules for transitions between electronic states. When 1) intervalley scattering (the scattering of electrons between K and K' cone) can be neglected, and 2) for a scattering potential that does not couple to the pseudospin portion of the electron wave function (which is the case when the potential range is larger than the lattice constant of graphene), the matrix element between the initial state and the final state in a scattering process can be written as [43]:

$$\left|\langle k'|V(r)|k\rangle\right|^2 = |V(k-k')|^2 \cos^2\left[\left(\theta_k - \theta_{k'}\right)/2\right]. \quad (2.4)$$

An immediate consequence of equation 2.4, as shown in Figure 2.1.3, is that intraband backscattering of an electron is forbidden [40, 42, 43]. An inelastic backscattering process (the interband scattering indicated as blue arrow in figure 2.3) is in principle allowed, but because the scattered electron has to become a hole in this process, the scattering does not lead to an increase in the resistivity [40]. Other intraband scattering processes (other than backscattering) are allowed, but the

scattering amplitude is suppressed by the cosine squared term in equation 2.4 for large angle scattering processes. Thus graphene is expected to have large mean-free paths and very low electric resistances, which is indeed observed [44].

The dispersion relation of the quasi-particles can be obtained by putting equation 2.3 into equation 2.2, as

$$\varepsilon = bhv_F \left|\vec{k}\right| / 2\pi , \tag{2.5}$$

which has the same form as a photon, indicating quasi-particles in graphene are moving with velocity $v_F \approx c/300$ where c is the speed of light. Similar to equation 2.3, b = 1 for electrons and -1 for holes.

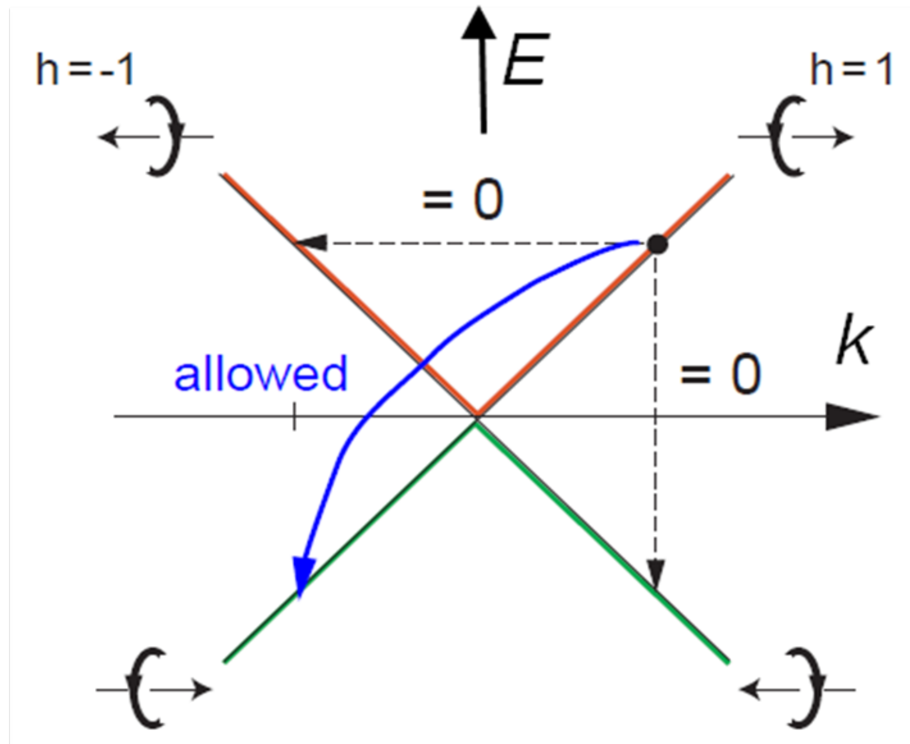

Figure 2.1.3 1D schematic of the graphene energy band near the *K* point, and the selection rule of intravalley transition, which could be explained by the prescription of conservation of the pseudo-spin. Figure from Ref. [40].

2.2 Charge transport in graphene: early experiments

The first graphene field effect devices were made by Novoselov *et al.* from the University of Manchester [45]. The graphene devices were made using the now famous mechanical exfoliation method[25], basically using Scotch tape to thin down a thick layer of graphite deposited on a thin silicon dioxide layer over doped silicon. This method turned out to be much more efficient than the much more sophisticated method of attaching graphite to an AFM tip and using the AFM piezo to controllably rub the graphite surface to a silicon dioxide surface [46].

It was found that graphene is an exceptional conductor with very high charge carrier mobility (μ) [44, 45, 47] (see Figure 2.2.1 and Figure 2.2.2). The conductivity of graphene is carrier-density (n) dependent, which could be tuned by electric field gating (V_g) through a dielectric layer [44, 45, 47]. A general feature of the transport characteristic of graphene, shown in figure 2.2.1, is that the conductivity is symmetric, ambipolar and linear in carrier density [44], with electron conduction at positive gate voltages and hole conduction at negative gate voltages. At higher gate voltage, the conductivity is often found to be slightly sublinear in carrier density for high mobility samples [34].

At low carrier density, at the transition between electron and hole conduction, the conductivity of graphene does not go to zero, but rather, shows a minimum. Such minimum conductivity (σ_{min}) is found by some group to be very close to $4e^2/h$ [44, 48] (see Figure 2.2.3), which was claimed to be the universal value for massless Dirac fermions; other groups found a wider range of the distribution of the minimum conductivity [31] (see Figure 2.2.4).

The minimum conductivity usually occurs near zero gate voltage ($V_{g,min}$) for good quality samples. A conductivity plateau also exists within a range of gate voltage near the minimum conductivity point, in which the conductivity does not change too much. Tan *et al.* [31] have reported the most extensive data on the range of behaviors observed for graphene devices on SiO_2, which are fabricated under the same conditions, and noted a phenomenological correlation between lower mobility, larger threshold shift, and broader minimum conductivity region (plateau region) (see Figure 2.2.5).

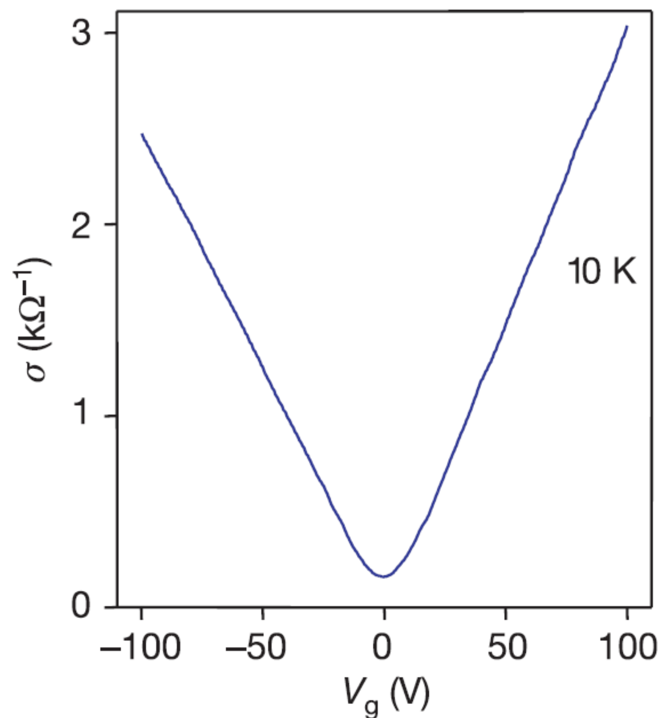

Figure 2.2.1 Conductivity of graphene as a function of the back gate voltage which is applied from a heavily doped silicon substrate through a thin layer of silicon dioxide as gate dielectric. Figure from Ref. [44].

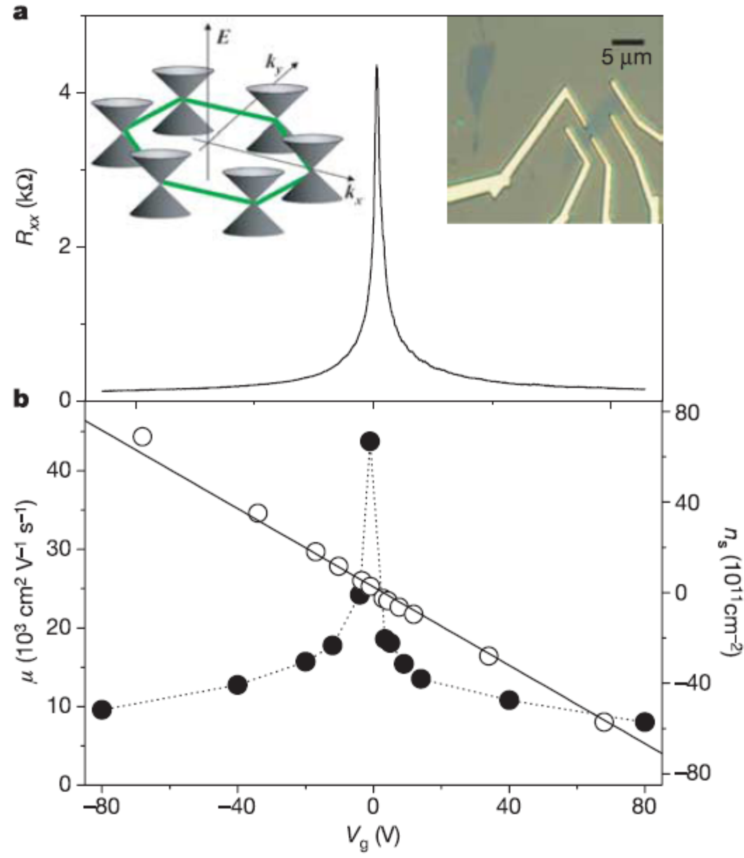

Figure 2.2.2 Resistivity (a), carrier density and mobility (b) of a graphene device on SiO_2 substrate as a function of gate voltage. Figure from Ref. [47].

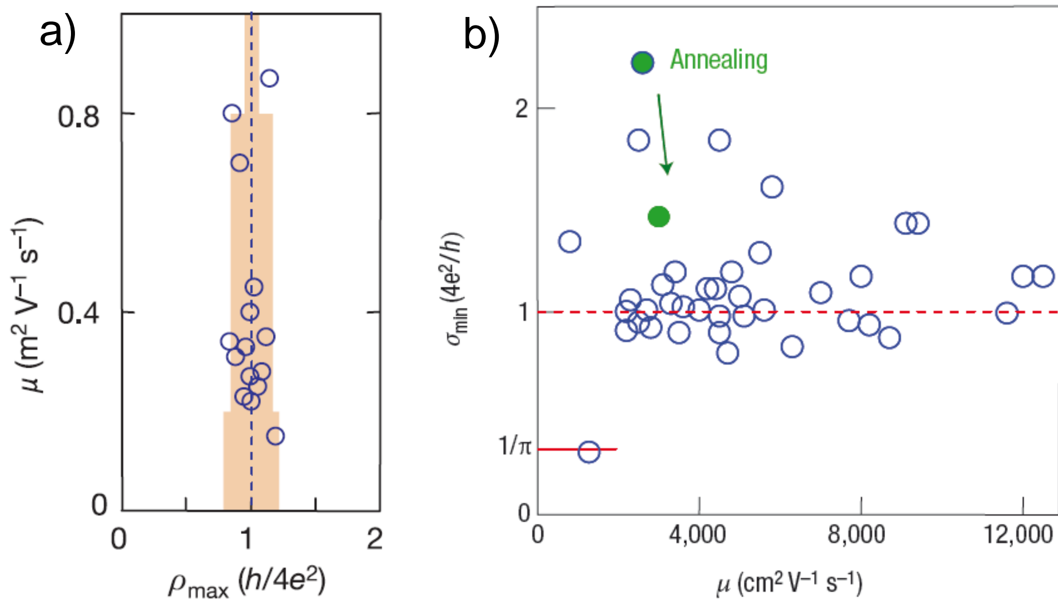

Figure 2.2.3 The "universal" minimum conductivity (maximum resistivity) reported by the Manchester group. Figure (a) from Ref. [25] and (b) from Ref. [48]

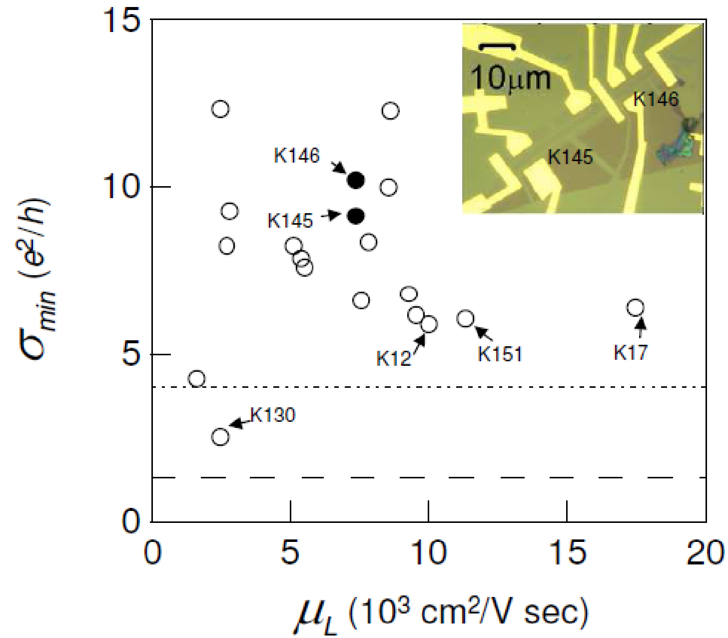

Figure 2.2.4 Variations of minimum conductivity for different graphene samples with different mobilities. Figure from Ref. [31].

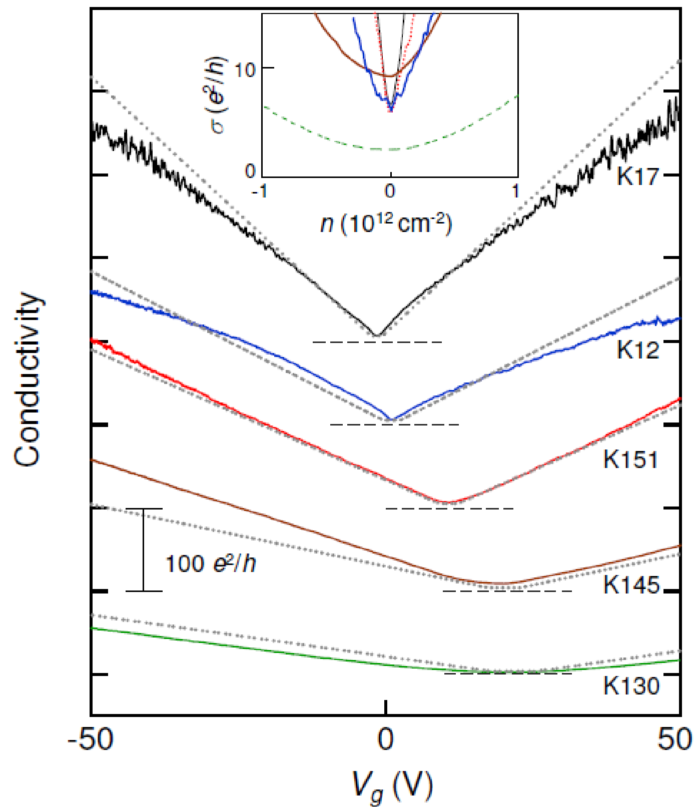

Figure 2.2.5 Phenomenological observation of the correlation between lower mobility, larger threshold shift, and broader minimum conductivity region (the plateau region). Figure from Ref. [31].

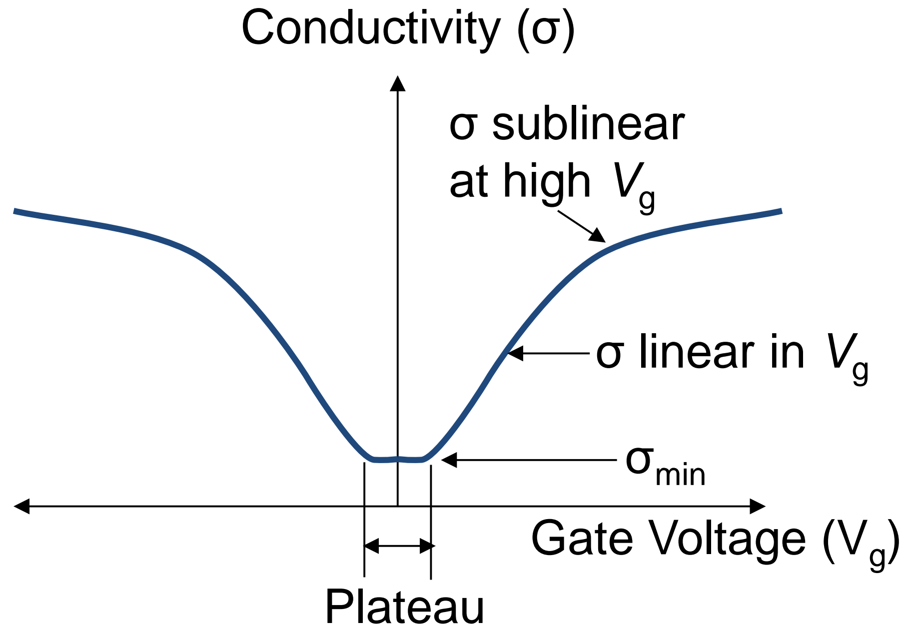

Figure 2.2.6 Schematics of the transport characteristic of graphene.

The overall transport characteristic of graphene is summarized in Figure 2.2.6, in which graphene shows a minimum conductivity over a small range of gate voltages (plateau region) at the transition between electron conduction and hole conduction; at not very high carrier density, the conductivity is linear in gate voltage (carrier density); at high gate voltage, for a high mobility sample, a sublinear dependence of the conductivity on gate voltage is often observed.

Chapter 3: Theories of carrier scattering in graphene

A striking aspect of graphene charge transport, observed since the earliest studies[31, 44], is the linear dependence of conductivity on charge carrier density $\sigma(n) \propto n$ over a wide range of carrier densities. Another feature is the minimum conductivity $\sigma_{\min}$, occurring at the transition between the electron conduction and hole conduction regime, which is thought to be a "universal" value by some groups [44] and otherwise by other groups [31, 33, 34, 37]. For graphene devices with high field effect mobilities, a sublinear dependence of the conductivity on carrier density is also observed [31, 34]. Theories on carrier scattering in graphene in zero magnetic field at low temperature (section 3.1-3.4) have been proposed to understand these characteristics. For understanding behavior at higher temperature, the theoretical predictions of the effects of phonons are described in section 3.5.

3.1 Charged impurities

Charged impurities are predicted to have dramatic effects on the transport properties of graphene. Several groups [49-53] have shown theoretically that charged impurity scattering in graphene should produce a conductivity linear in charge density and inversely proportional to impurity density, i.e.

$$\sigma_{ci}(n) = C_{ci} e \left| \frac{n}{n_{imp}} \right| \tag{3.1}$$

This is equivalent to a constant mobility, inversely proportional to charged impurity density $\mu = C/n_{\text{imp}}$. The linear $\sigma_{ci}(n)$ results from the $1/q$ dependence of the Coulomb potential on wavevector q; leading to a $1/k_F$ dependence of the scattering rate. A

unique aspect of graphene, as opposed to other two-dimensional electron systems (2DES) is that the $1/k_F$ dependence is preserved even for a *screened* Coulomb potential in graphene [52], creating a clear dichotomy in graphene between long-range and short-range scattering potentials. Hwang, et al. [52] calculated the screened Coulomb potential within the random phase approximation (RPA), and used the results to determine $C_{ci} \approx 5 \times 10^{15}$ V^{-1}s^{-1}. Novikov [54] noted that, beyond the Born approximation used in Ref. [52], an asymmetry in C_{ci} for attractive vs. repulsive scattering (electron vs. hole carriers) is expected for Dirac fermions.

In the present of charged impurities, at low carrier density, the conductivity does not vanish linearly, but rather saturates to a constant value, the minimum conductivity $\sigma_{\min}$, over a plateau of width ΔV_g [50, 52, 53]. Numerical calculations [50, 52] showed a finite conductivity of order $4e^2/h$ at zero charge density, which persisted over a plateau width roughly determined by the impurity density. Adam *et al.* [53] calculated the plateau width ΔV_g analytically; they also found analytically the dependence of the minimum conductivity on the charged impurity density, which ranges from $4e^2/h$ to $20\ e^2/h$, and calculated the carrier density at which the minimum conductivity occurs ($V_{g,\min}$), adapting the theory of semiconductor band tails [55] to this problem. They predict that $\sigma_{\min}$ occurs not at the carrier density which neutralizes n_{imp}, but rather the carrier density at which the average impurity potential is zero [53]. This prediction suggests that the gate voltage of the minimum conductivity $V_{g,\min}$ would have an effective power law dependence on n_{imp}, with an exponent functionally of the distance of the charged impurities to graphene, and is not equal to one [53]. The minimum conductivity problem was also treated by Cheianov *et al.* [51]; the

results are qualitatively consistent with Adam, *et al.* [53], but they made no quantitative prediction on the magnitude or charged-impurity-density dependence of the minimum conductivity.

3.2 "White-noise" disorder

Earlier theoretical work [56, 57] on massless Dirac fermions using the Kubo formalism showed that the conductivity at the Dirac point for vanishing short-ranged disorder is $4e^2/\pi h$. The minimum conductivity on the order of $4e^2/\pi h$ in graphene in the absence of disorder has been verified by others using the Kubo [58] and Landauer formalisms [58, 59]. However, experimentally, the minimum conductivity of graphene rarely goes below $4e^2/h$ [31, 34, 44], except for when intervalley scattering is turned on [33].

The addition of point scatterers gives a finite conductivity at finite carrier density which is *independent* of carrier density [42]. Attempts [50, 60] to extrapolate between the high- and zero-density limits of scattering from short-range disorder have given a square-root dependence of conductivity on density, in contradiction with the experimentally-observed linear dependence.

3.3 Vacancy Defects

Hentschel *et al.* [61] proposed that vacancy defects in graphene give rise to bound states at the Dirac point, which are also called mid-gap states. Mid-gap states are strong carrier scatterers with short range interaction, which strongly perturb the

system such that the Klein-paradox [62] is not at work, and the scattering potential give rise to a conductivity in graphene of the form that is similar to a non-relativistic electron gas [61, 63]:

$$\sigma_{mg}(n) = C_{mg} e \left| \frac{n}{n_d} \right| \left[\ln\left(\sqrt{\pi n} R_0 \right) \right]^2 \tag{3.2}$$

where C_{mg} is a constant, n_d is the vacancy defect density and R_0 is the effective radius of the vacancy (on the order of the bond length in graphene). The logarithmic term leads to a slightly sub-linear dependence of conductivity on charge density.

3.4 Corrugations of the graphene sheet

Another proposal to explain the linear $\sigma(n)$ has been the effect of geometric corrugation of graphene (i.e. "ripples"), present due to contact with a rough substrate [38] or as a result of proposed thermally-activated out-of-plane motion of the graphene sheet [64, 65], or the presence of local modification of the bonding in graphene [66]. Katsnelson and Geim [65] have suggested that ripples in graphene produce a conductivity of the form

$$\sigma_{corr}(n) = C_{corr} e n^{2H-1} \tag{3.3}$$

where C_{corr} is a constant which is proportional to $(r/z)^2$ where r is the radius and z is the height of the ripple, and the exponent $2H$ is given by the distance dependence of the height-height correlation function of a corrugated surface, e.g. $g(r) \propto r^{2H}$ at small r, where $g(r) = \left\langle (h(r_0 + r) - h(r_0))^2 \right\rangle$. In this scenario, scattering by ripples would produce a linear $\sigma(n)$ for $2H = 2$, a situation that would, in principle, occur for

equilibrium fluctuations of a flexible membrane in a planar confining potential [67]; or a constant $\sigma(n)$ for $2H = 1$, typical of the much more common case of a non-equilibrium structure with short-range correlations [68]; or a conductivity which has very weak density dependence, for $1 < 2H < 2$ (see Appendix A1&A2 for experimental details).

The magnitude of the scattering from ripples can be made by estimating C_{corr}. Cullen *et al.* [36, 69] pointed out that the relationship, $C_{corr} \propto \left(r/z\right)^2$ can be better formulated as $C_{corr} \propto \left(qA(q)\right)^{-2}$, where q is the wavevector of the Fourier spectrum of the corrugation and $A(q)$ is the Fourier amplitude which is a function of q. Cullen *et al.* argued that, the maximum value of $qA(q)$, readily obtained from the Fourier spectrum, should set an upper bound to the additional resistivity associated with the rippling of graphene [36, 69] (see Appendix A2 for experimental details).

3.5 Phonons

Longitudinal acoustic (LA) phonon scattering in graphene is expected [63, 70-72] to give rise to a resistivity independent of carrier density and linear in temperature, i.e.

$$\rho_{LA} = \left(\frac{h}{e^2}\right)\frac{\pi^2 D_A^2 k_B T}{2h^2 \rho_s v_s^2 v_F{}^2}, \tag{3.4}$$

where k_B is the Boltzmann constant, $\rho_s = 7.6 \times 10^{-7}$ kg/m^2 is the 2D mass density of graphene, $v_F = 10^6$ m/s is the Fermi velocity, $v_s = 2.1 \times 10^4$ m/s is the sound velocity for LA phonons, and D_A the acoustic deformation potential.

For substrate-bound graphene devices, however, in addition to LA phonon in graphene, the polar optical phonons of the SiO_2 substrate are also expected to scatter electrons in graphene through remote interfacial phonon (RIP) scattering [73-75]. The two strongest surface optical phonon modes in SiO_2 are calculated to have $\hbar\omega \approx$ 59 meV and 155 meV, with a ratio of coupling to the electrons of 1:6.5 [74, 75]. RIP results in a long-ranged potential, which gives rise to a density-dependent resistivity in graphene, similar to charged impurity scattering. Specifically, in the simplest case, the electron-phonon matrix $|H_{\mathbf{kk'}}|^2$ element is proportional to q^{-1} where q is the scattering wavevector, and the resistivity is proportional to $k_F^{-1} \propto V_g^{-1/2}$. However, finite-$q$ corrections to $|H_{\mathbf{kk'}}|^2$ lead to a stronger dependence of $\rho_B(V_g,T)$ on V_g [75], such that the resistivity arising from polar optical phonon scattering is

$$\rho_{PO}(V_g,T) = C_{PO}V_g^{-\alpha}\left(\frac{1}{e^{(59meV)/k_BT}-1}+\frac{6.5}{e^{(155meV)/k_BT}-1}\right) \tag{3.5}$$

where C_{PO} is a constant defining the strength of the scattering, α is the exponent on the density dependence, both of which can be experimentally determined; the terms in the brackets are the Bose-Einstein terms from the two strong polar optical phonons and the coupling radio of 1:6.5 is determined by the oscillator strength and energy of these phonon modes [74].

Chapter 4: Experimental techniques

This chapter outlined the experimental techniques used in subsequent chapters. Section 4.1 described the process to fabricate clean graphene field effect devices on SO_2 substrate, which will be the starting point for experiments covered by chapter 5 – 7; Section 4.2 presents the Helitran ultra-high vacuum (UHV) compatible open cycle cryostat, which will be used in experiments in chapter 5 – 7; Section 4.3 described the JEOL UHV scanning probe microscopy (SPM), which is used to study the morphology of graphene on SiO_2 (details in Appendix A1 and A2); Section 4.4 covers the transfer-printing technique which is used in chapter 8; Section 4.5 is devoted to charge transport measurement schemes which is used throughout the rest of the thesis. The experimental setup of the UHV transport measurement, detailed in section 4.5, is used in chapter 5 – 7.

4.1 Graphene Field Effect Device Fabrication

Graphene is obtained from Kish graphite by mechanical exfoliation [25] on 300nm SiO_2 over doped Si. The doped silicon is subsequently used as the gate electrode (back gate) and the SiO_2 as the gate dielectric. Optical microscopy is used for preliminary identification of graphene as shown in Figure 4.1.1. Electrodes are defined by electron-beam lithography and thermal evaporation of 3 nm of Chromium (sticking layer) and 60 nm of Gold (see Figure 4.1.2). Sometimes a second lithography step is performed to pattern the graphene into a Hall-bar shape to allow

for more accurate measurement of the conductivity with less contact effects (see Figure 4.1.2). The resulting field effect device is illustrated in Figure 4.1.3.

After device fabrication, Raman spectra are obtain from these samples, in which the single Lorentzian D' peak confirms that the samples are single layer graphene [76] (see Figure 4.1.4).

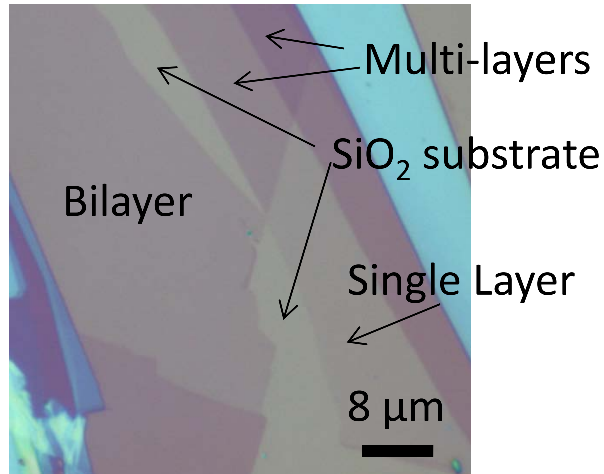

Figure 4.1.1 Optical Micrograph of exfoliated graphene layers on 300 nm thick SiO_2 substrate. The bare silicon dioxide area, single layer graphene, bilayer graphene and multilayer graphene are marked by arrows. Areas that show bright blue colors are thick graphite flakes.

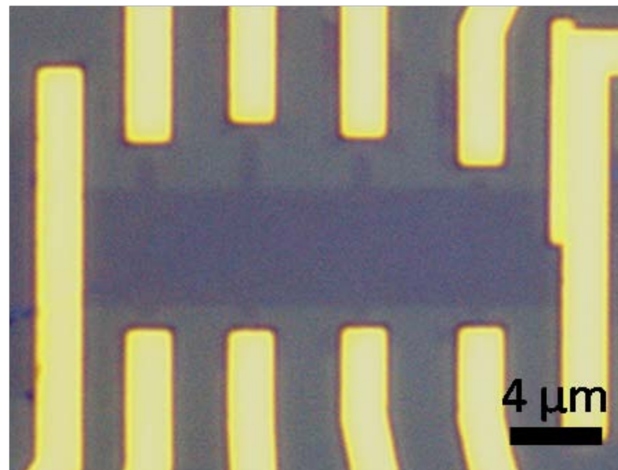

Figure 4.1.2 Optical Micrograph of a patterned exfoliated graphene device on 300 nm thick SiO_2 substrate. The golden parts are Cr/Au electrodes, graphene have been patterned into Hall-bar shape (middle region) using an additional lithography step and reactive ion etch.

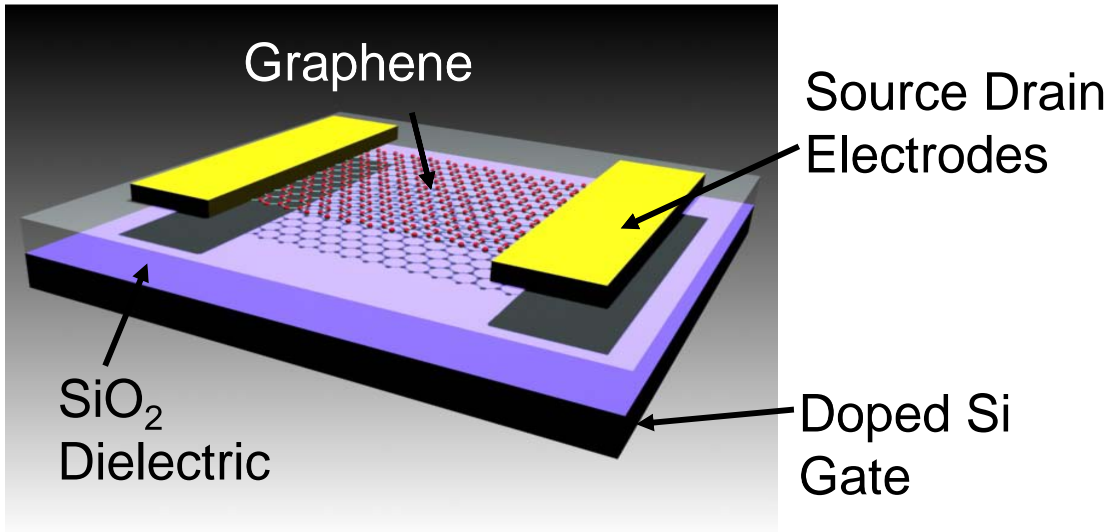

Figure 4.1.3 Three dimensional schematic of a graphene field effect device on a 300 nm thick SiO_2 substrate with doped Si back gate.

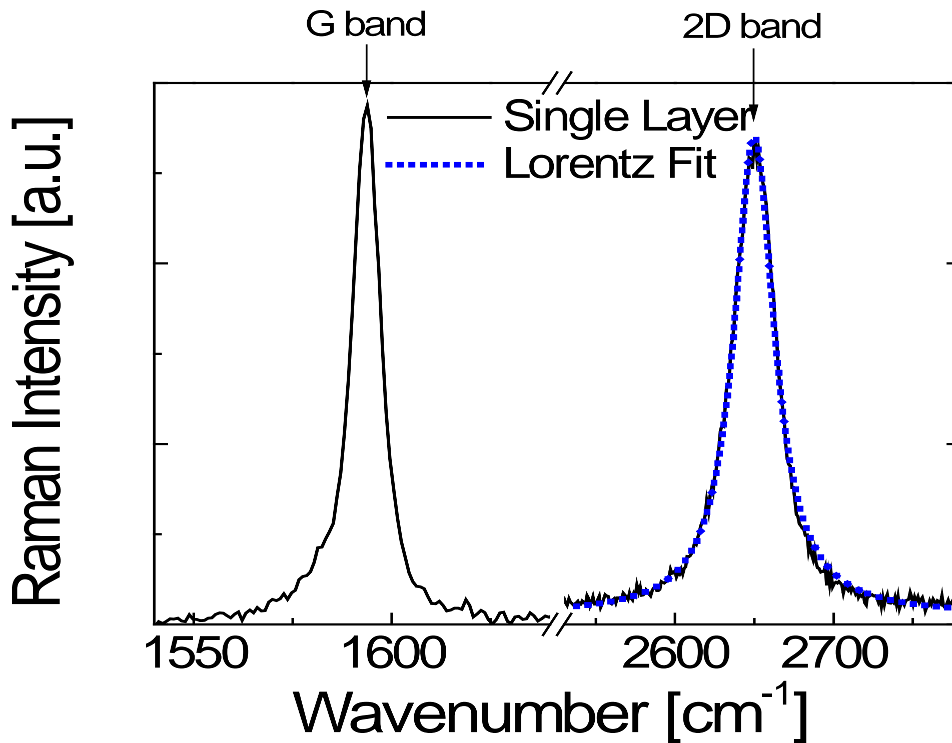

Figure 4.1.4 Micro-Raman spectra of a single layer graphene. The single Lorentzian 2D band is the signature for single layer graphene.

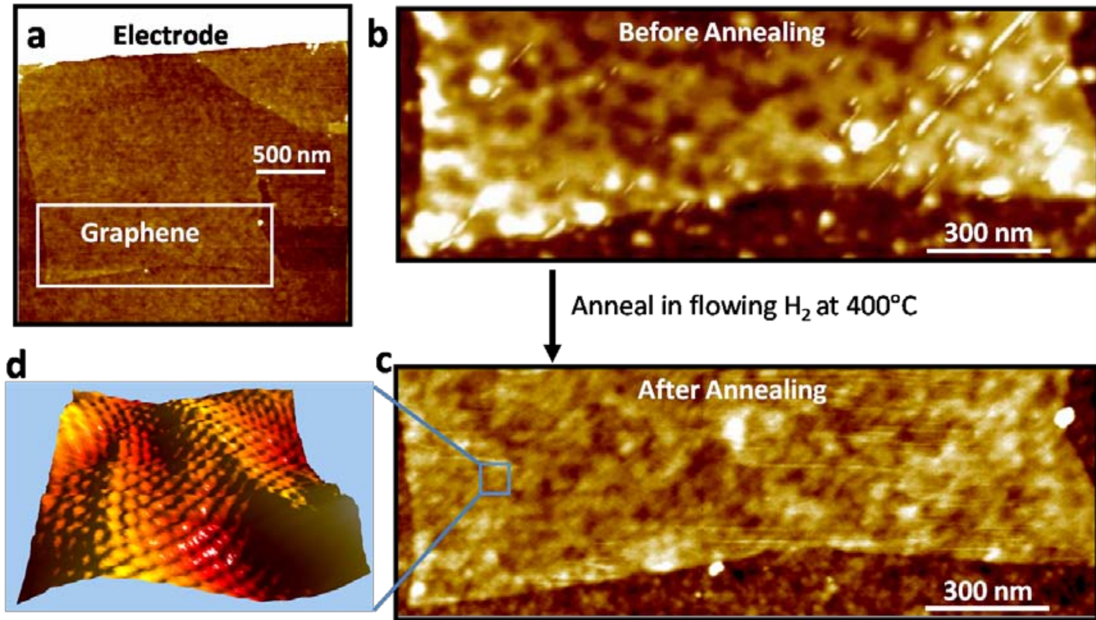

Figure 4.1.5 A graphene device before and after removal of PMMA residue. a) Non-Contact AFM micrograph of clean graphene device on SiO_2 substrate; b)&c) Zoomed-in AFM micrograph of graphene on SiO_2 (white rectangle in Fig.3.5a) before (b) and after (c) removal of PMMA residue; d) atomically-resolved STM micrograph of cleaned graphene surface.

Before measurements in ultra high vacuum (UHV), the devices are annealed in flowing H_2 and Ar (flow rate: H_2 1700 ml/min, Ar 1900 ml/min) at 300 ℃ for 1 hour to remove resist residues [34, 38] (see Figure 4.1.5), with additional bake-outs up to 490 K following insertion into UHV to remove residual absorbed gases [34].

4.2 The Helitran ultra-high vacuum compatible LT-3B open cycle cryostat

The Helitran UHV compatible LT-3B open cycle cryostat is designed and manufactured by Advanced Research Systems Inc. It operates with liquid helium in the 2-300K range[2] and with liquid nitrogen in the 77- 300K range. A heater is also

[2] The lowest temperature actually achieved in experiment is about 10K, higher than the specification of 2K, possibly due to additional thermal load by the electrical measurement wiring and the custom sample stage.

installed near the sample mount to enable temperature control above 300K . The use of high temperature brazing materials and internal welds in the cryostat allows bakeout temperatures of up to 500 K, which is essential for degassing the graphene sample as well as temperature-dependent measurements up to 500K. It has multi-pin UHV instrumentation feedthroughs to allow electrical signals in and out of the chamber.

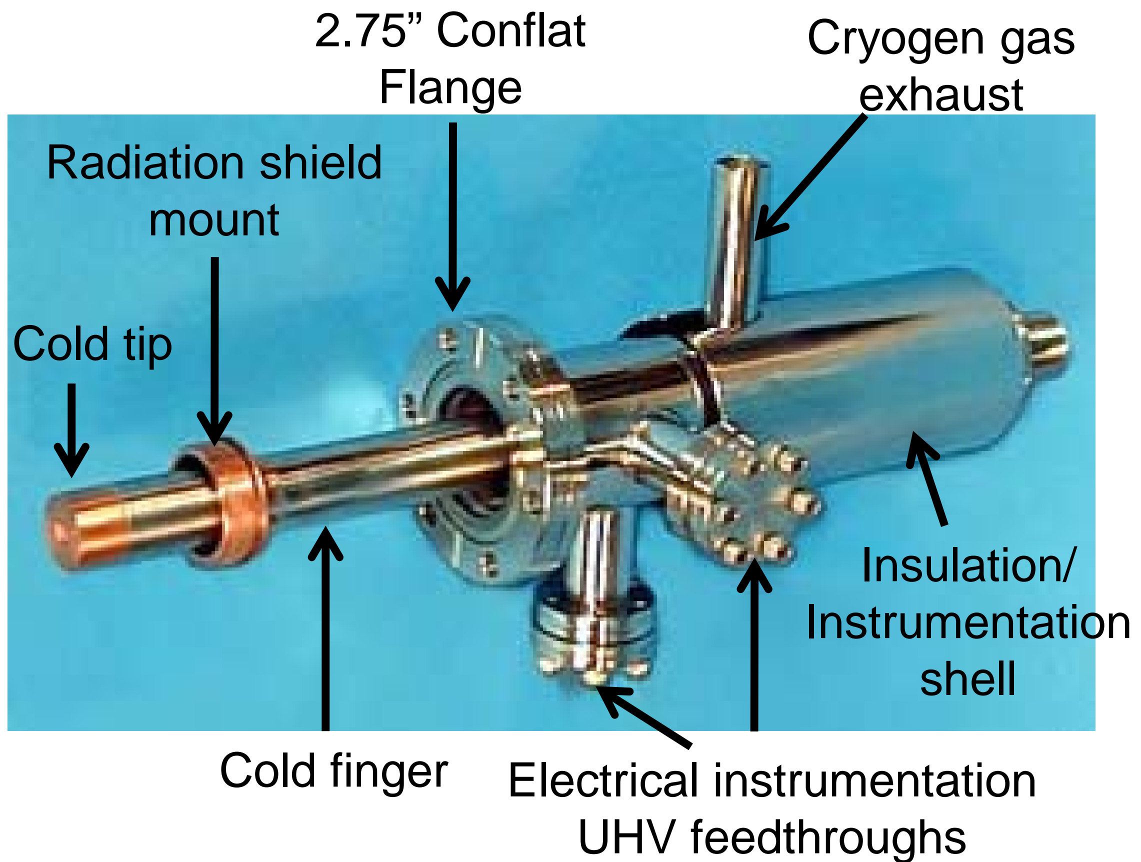

Figure 4.2.1 The LT-3B ultra high vacuum compatible cryostat (electrical instrumentation and custom sample mount not shown). Figure adopted from Ref. [77].

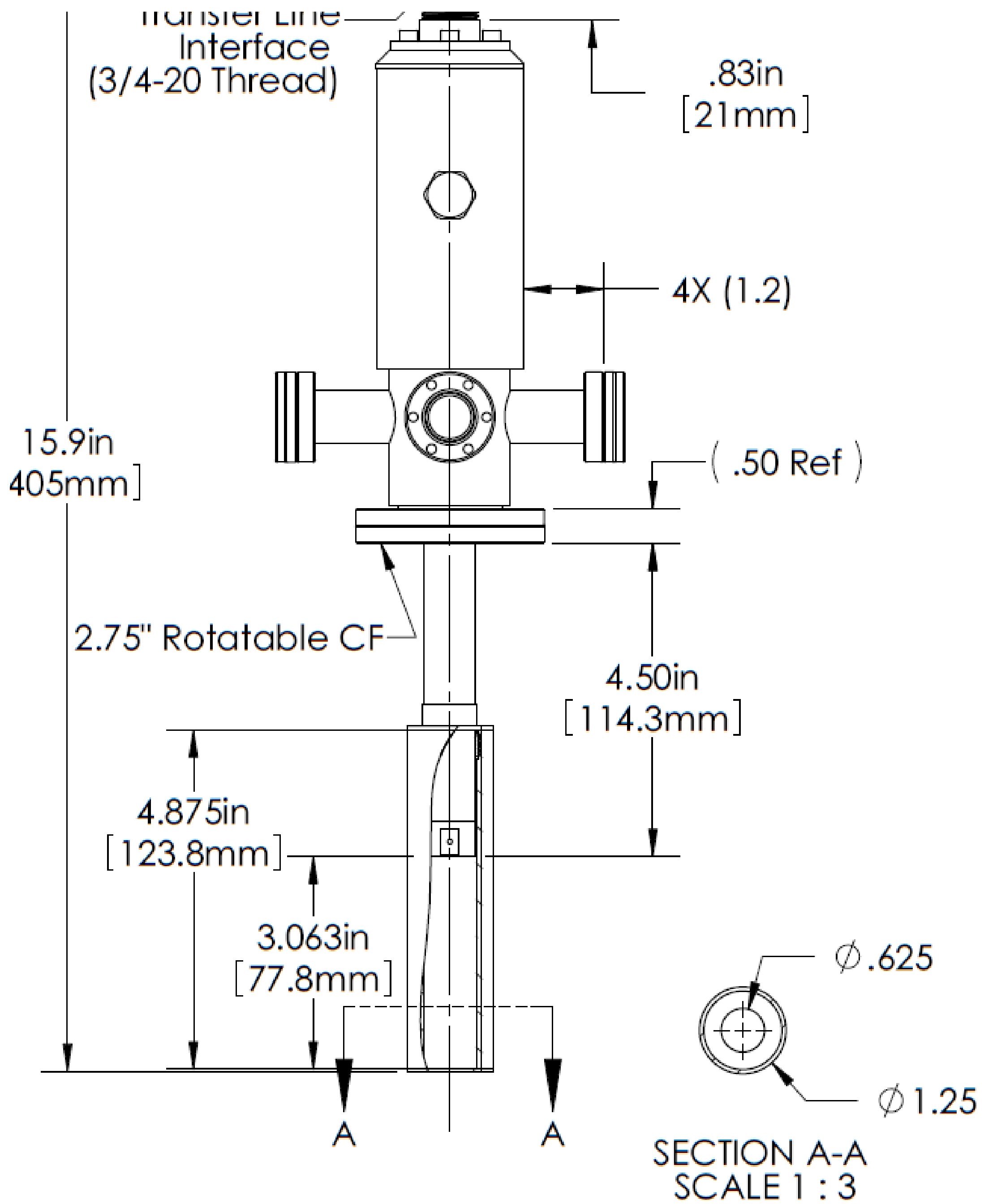

Figure 4.2.2 The assembly drawing of the LT-3B cryostat with dimensions. The drawing is with the radiation shield mounted on the cold finger. Drawing from Advanced Research Systems, Inc.

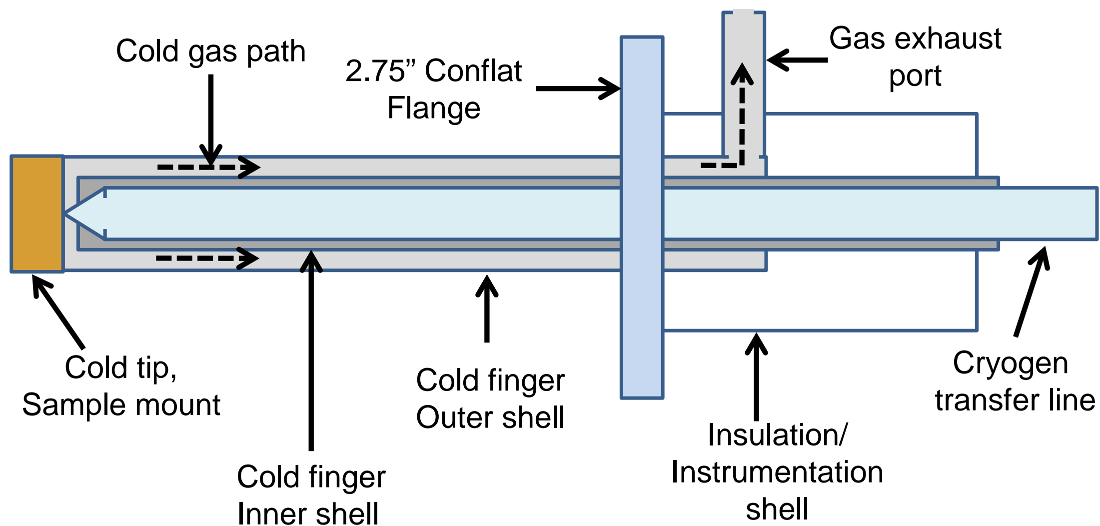

Figure 4.2.3 Schematic of the internal structure of the LT-3B ultra high vacuum compatible cryostat (electrical instrumentation and custom sample mount not shown).

The open cycle cryostat works as liquid Helium or liquid Nitrogen is continuously evaporated at the cold tip (see Figure 4.2.2), and the cold Helium / Nitrogen gas runs from the top of the cold finger to the bottom before coming out from the exhaust port, thus cooling the whole cold finger with high efficiency. The electrical wires are all thermally anchored to the cold finger so that they do not act as a significant heat source to the sample at the cold tip. The cold tip and thus the sample mount are completely exposed to the UHV environment, which is important for most of my UHV transport measurements.

4.3 The JEOL ultra-high vacuum scanning probe microscope

The JEOL ultra-high vacuum scanning probe microscope (JSPM 4500A) is designed and manufactured by the Japan Electron Optics Laboratory, Inc. It is a highly capable scanning probe instrument which combines a scanning electron

microscope (SEM), an atomic force microscope (AFM) and a scanning tunneling microscope (STM) in UHV environment (see Figure 4.3.1). An important feature of the system is that a conducting AFM tip is used for both AFM mode and STM mode, and the two modes can be switched back and forward without losing the tip position. This feature is used to precisely position the tip, for STM imaging, on a very small conducting area surrounded by large insulating area, which enables imaging exfoliated graphene on a device configuration [38, 69]. In addition, electrical instrumentation at the stage allows *in situ* transport measurements of the devices during SEM imaging or SPM imaging, greatly expanding the list of possible experiments that the system can accomplish. The sample can also be cooled to about 35K using liquid Helium.

The samples and the AFM/STM tips can be transferred into the system using the load-lock marked in Figure 4.3.1. Then an UHV bake-out can be made in the sample preparation chamber before the samples and the tips are transferred to the measurement chamber using a magnetic manipulator. The SEM can be used to position the tip over small features and to observe the tip approach process (see Figure 4.3.3). The AFM has been used to study the morphology of graphene devices, and also to further position the tip to a desired location with nanometer precision.

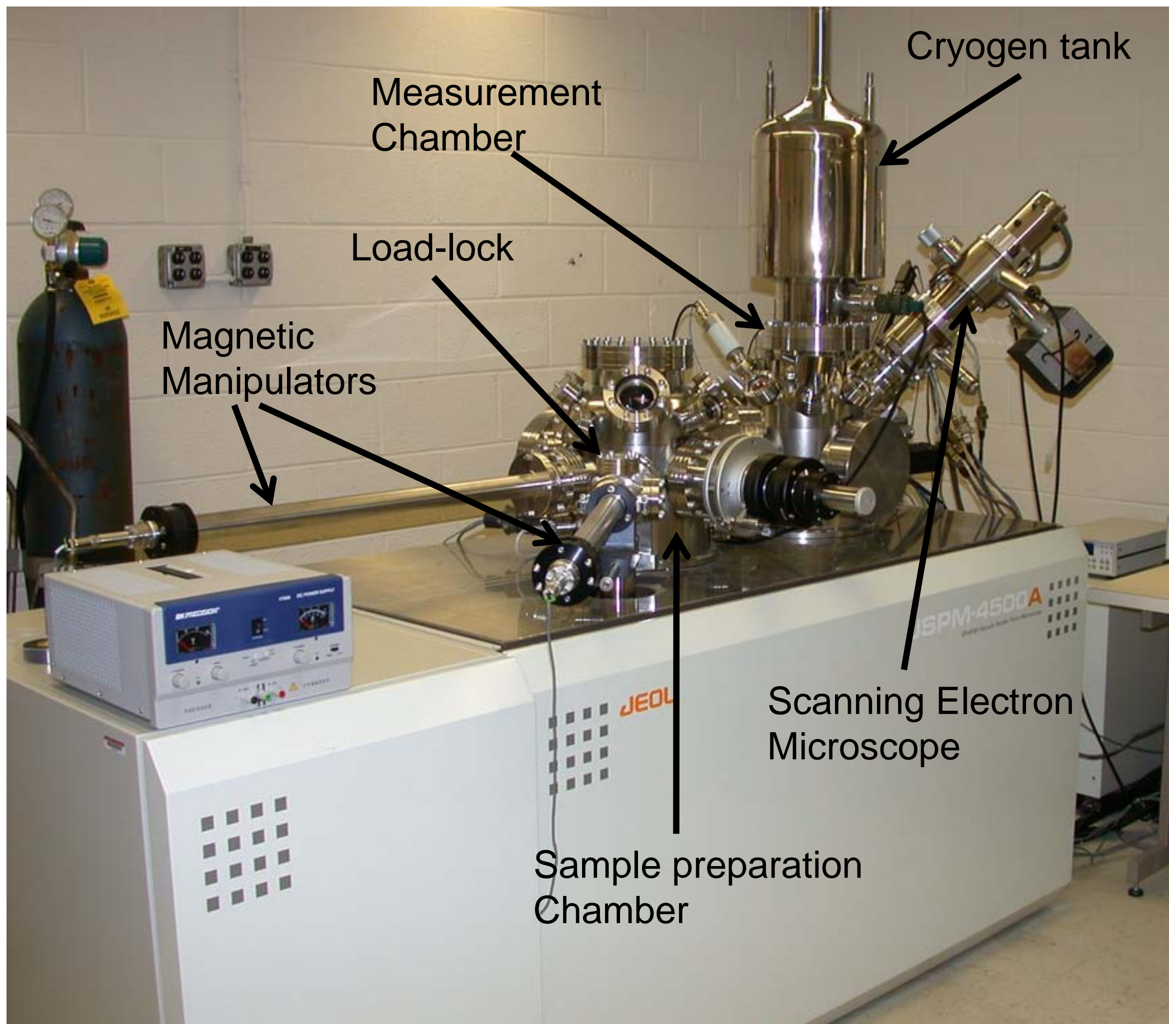

Figure 4.3.1 The JEOL ultra-high vacuum scanning probe microscope.

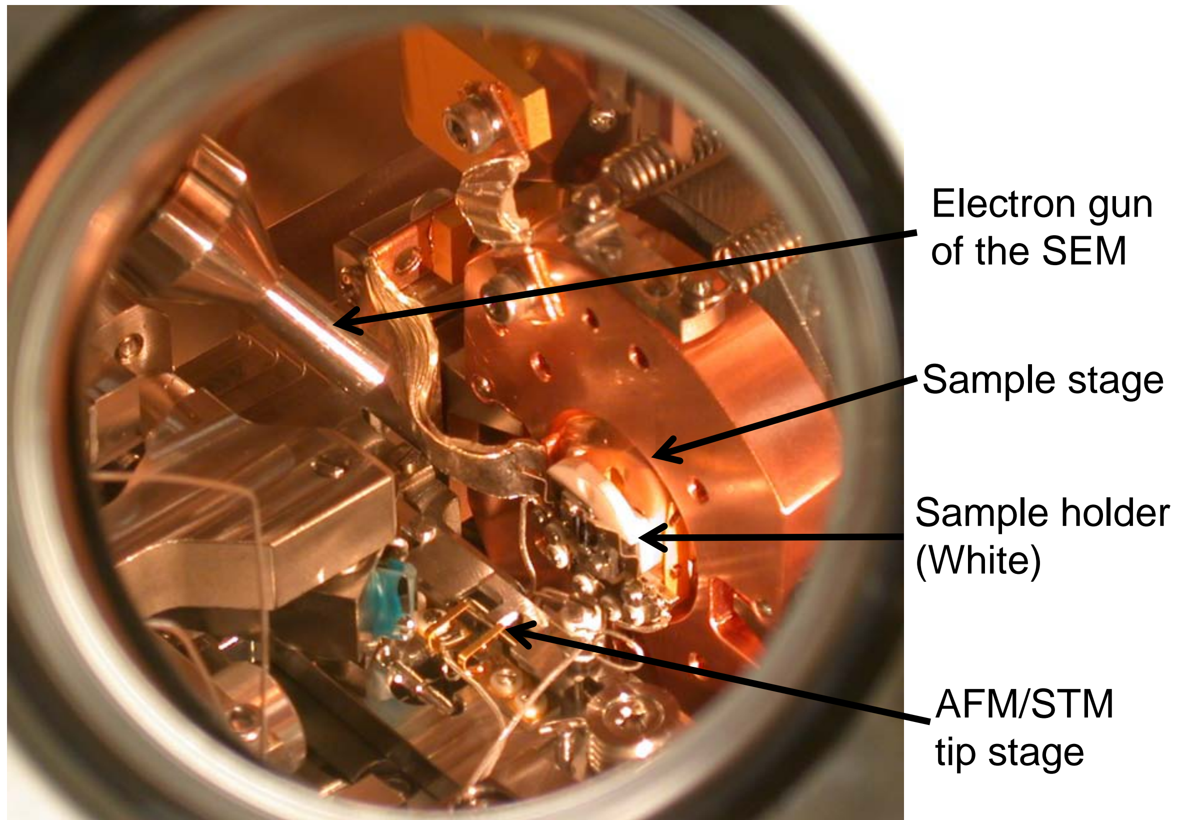

Figure 4.3.2 The viewport look of the measurement stage of the JEOL SPM.

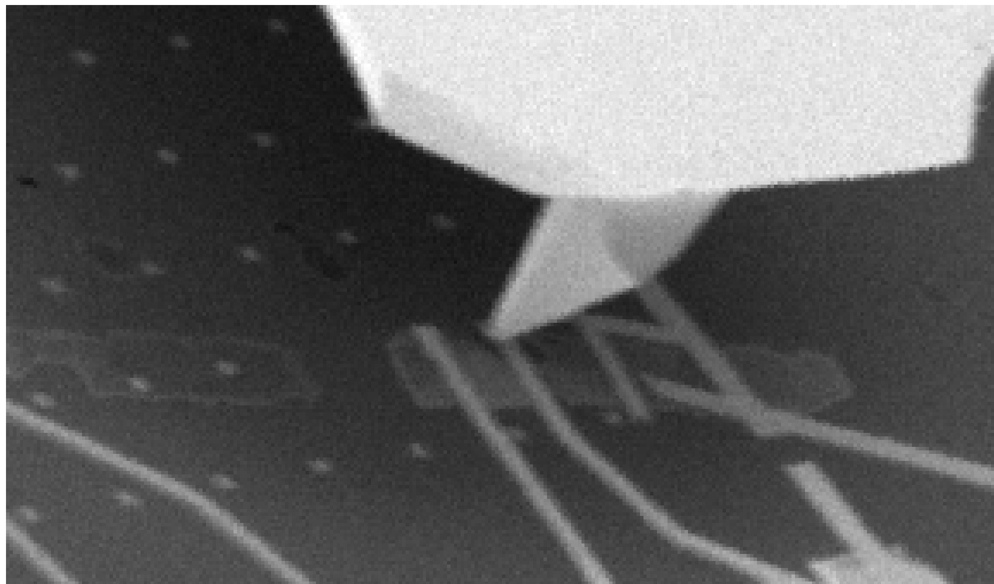

Figure 4.3.3 SEM micrograph of the AFM/STM tip over a graphene field effect device. The flake-like feature right below the tip is a 30 × 8 μm graphene flake connected by gold electrodes and the dots on the upper left corner of the micrograph are the alignment markers.

4.4 The Transfer-printing technique

The transfer printing technique is closely related to the Nano-Imprint Lithography (NIL), in which a hard mold is pressed again a softer target substrate leaving a dent on the target substrate, with the shape defined by the mold. In my experiment, a NIL tool, the NX-2500 Nano-Imprintor with optical alignment (see Figure 4.4.1), designed and manufactured by Nanonex, Inc., is used to transfer print graphene, the electrodes and the dielectric layer to form a field effect device on a flexible Polyethylene Terephthalate (PET) substrate.

The transfer printing technique primarily relies on differential adhesion of a printable layer that is pressed between two substrates [78, 79], which enables the printable layer to be transferred from one substrate of lower adhesion (transfer substrate) to another substrate of higher adhesion (device substrate). The process is depicted in Figure 4.4.2. To facilitate the transfer or increase the adhesion of the printable layer to the device substrate, pressure and heat is usually used (Figure 4.4.2(b)). The process is relatively simple and compatible with many different materials, including graphene, and can be used to "assemble" graphene field effect devices on flexible and transparent substrates, which will be described in detail in Chapter 8.

Before the assembling process, graphene on a transfer substrate has to be prepared. Here we use SiO_2/Si substrate as the transfer substrate, because it is compatible with the mechanical exfoliation method [25] and the adhesion energy between graphene and the SiO_2 substrate is not too strong. In addition to graphene sample, the source-drain electrodes, the gate electrodes and gate dielectrics are also

pre-fabricated on separate silicon chips (transfer substrates), which are then printed onto the device substrate one by one to fabricate a device. The procedure for making graphene is shown in Figure 4.4.3.

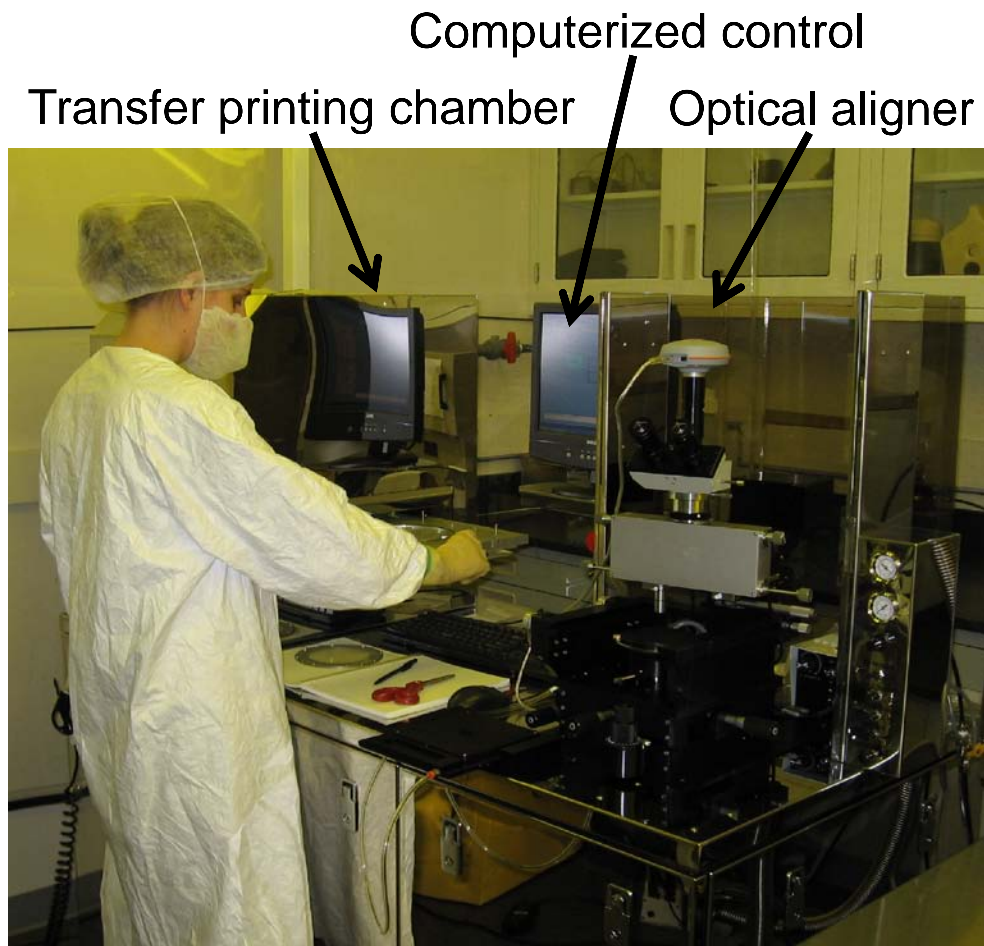

Figure 4.4.1 The NX-2500 Full-Wafer Imprintor with optical Alignment from Nanonex Inc. Picture courtesy of Tracy Moore.

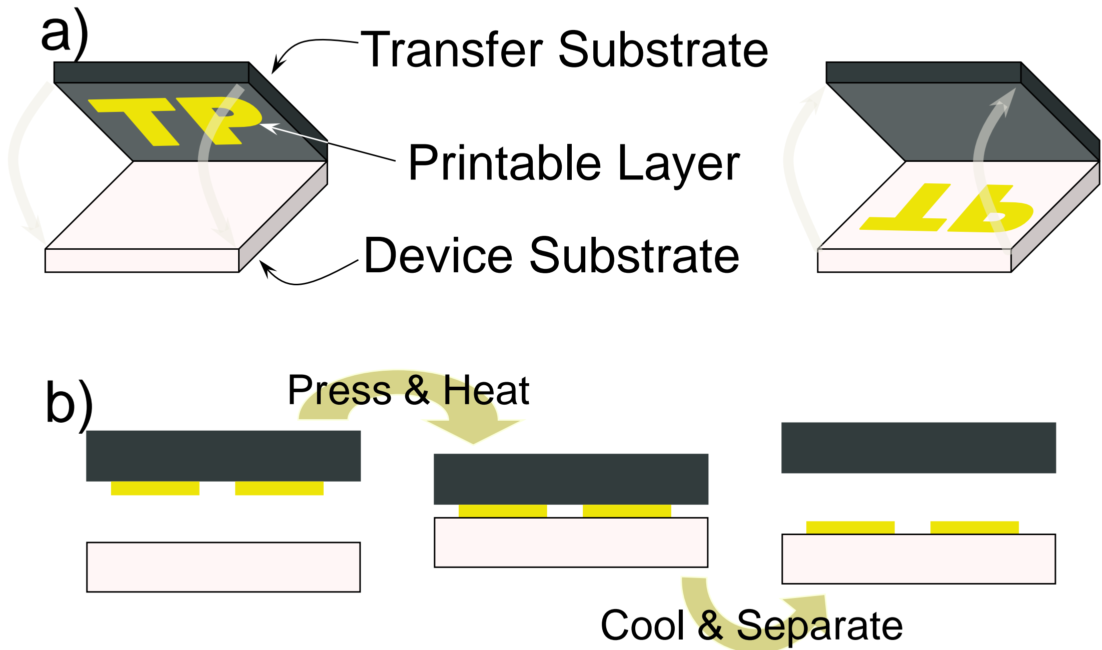

Figure 4.4.2 The schematics of the transfer printing method. a) A transfer printing step; b) pressure and heat are use to facilitate the transfer. Courtesy of Dr. Daniel R. Hines.

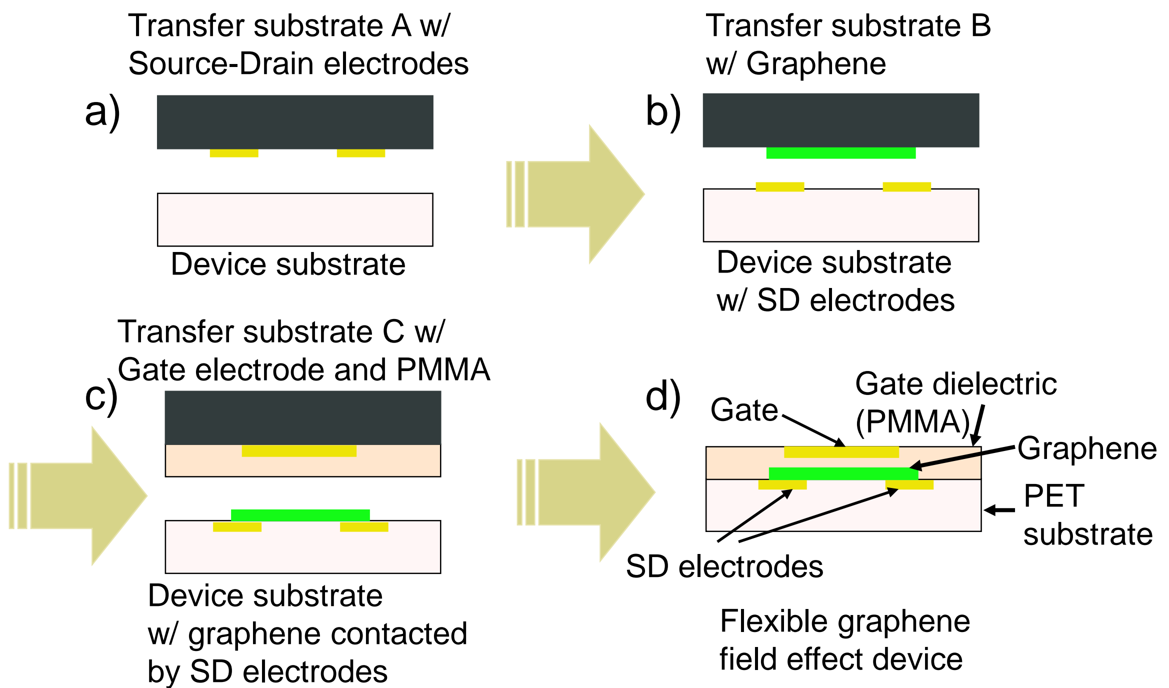

Figure 4.4.3 Procedure for making flexible and transparent graphene field effect device.

4.5 Transport measurements and experimental setup in ultra-high vacuum

With the graphene device fabricated on SiO_2 substrates or on PET substrates, transport measurements are carried out to characterize these devices. I used measurement schemes which fall into two categories: the DC measurement and the quasi-DC (low frequency AC) measurement.

For two-probed measurements, in which current and voltage are measured between the same two electrodes of the device, DC measurement are used in my earlier experiments (Chapter 8); quasi-DC measurements are performed with two-probed and four-probed configurations, in which current and voltage are measurement using a separate pair of current and voltage probes, in order to exclude contact resistance from the measured data, in later experiments (all other transport measurements shown in this article).

Figure 4.5.1 shows the schematics of the DC measurement. The resistors R_1 and R_2 act as a voltage divider, dividing up to 10 volts from the Nation Instrument DAC-board, and R_g acts as a current-limiting protection resistor in the case of a short circuit between the graphene and the gate. The divided voltage is applied to the one of the source-drain electrodes, with the other source-drain electrode connected to the virtual ground of a current preamplifier. The current that flows through the device to the virtual ground is then converted into a voltage signal and amplified. The voltage from the preamplifier is input to the DAC-board, which digitizes the signal and transmits it to a computer. A Keithley source meter is used to provide a gate voltage which tunes the carrier density in graphene. The disadvantages of such measurement scheme are 1) the intrinsic inability of DC measurements to filter out electrical noise;

2) the resistivity of graphene R_{device} typically ranges from 100Ω to 6kΩ depending on carrier density, thus limiting the resistance range of the voltage divider, whose proper functioning requires that $R_2 << R_{\text{device}}$.

In the quasi-DC measurement scheme, shown in Figure 4.5.2, a lock-in amplifier is used to act as a low frequency signal source and phase-sensitive signal amplifier. Phase-sensitive detection of a AC signal with known frequency gets rid of the electrical noise that has a frequency that is not close to the signal frequency [80]. The voltage signal generated by the lock-in amplifier is converted to a current signal determined by R_s, given that $R_s >> R_{\text{device}}$, which is usually easily achieved in measuring graphene. Two voltage probes, A and B in Figure 4.5.2, are connected to the voltage electrodes of the graphene device and the voltage difference is detected by the lock-in amplifier and then transmitted to the DAC-board. Similar to the DC measurement scheme, a Keithley source meter is used to provide a gate voltage which tunes the carrier density in graphene. The typical values of the resistors are: R_s = 1MΩ, R_g = 100MΩ, and a typical AC frequency used is 287.1 Hz.

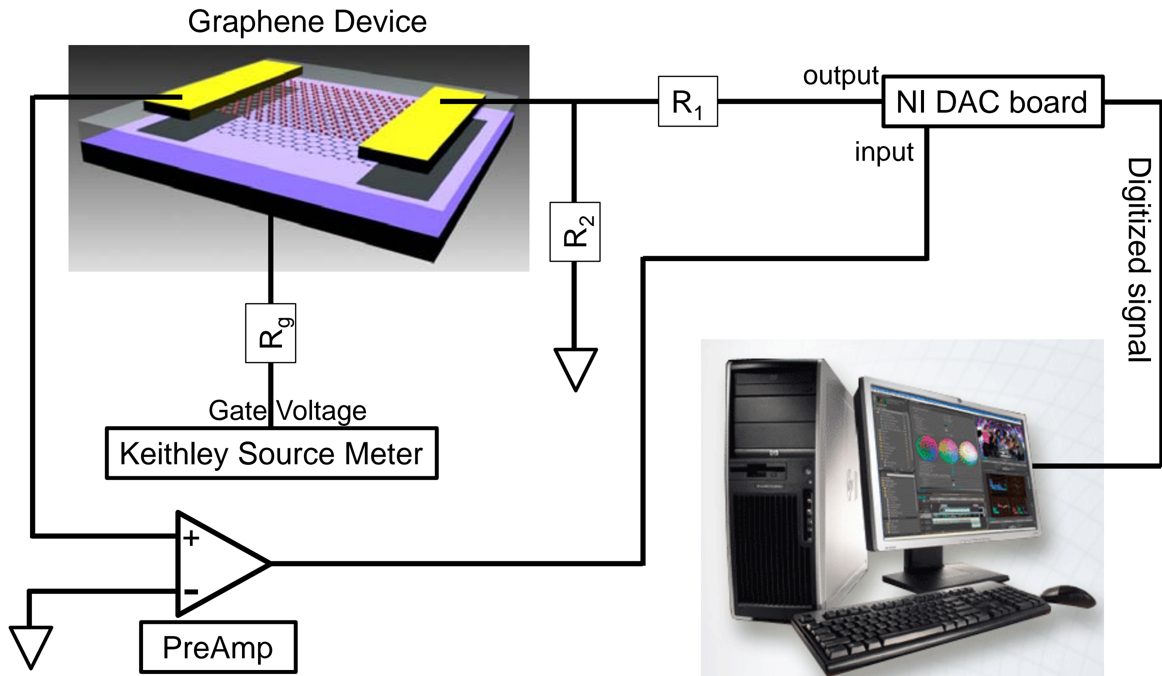

Figure 4.5.1 Schematics of a DC measurement of the electronic properties of graphene. Typical values for the resistors are: R_1 = 1kΩ, R_2 = 10 Ω, R_g = 100MΩ. Here R_1 and R_2 are used as a 100:1 voltage dividers, with R_2 << the device resistance, which usually ranges from 100Ω to 6kΩ, depending on carrier density in the device.

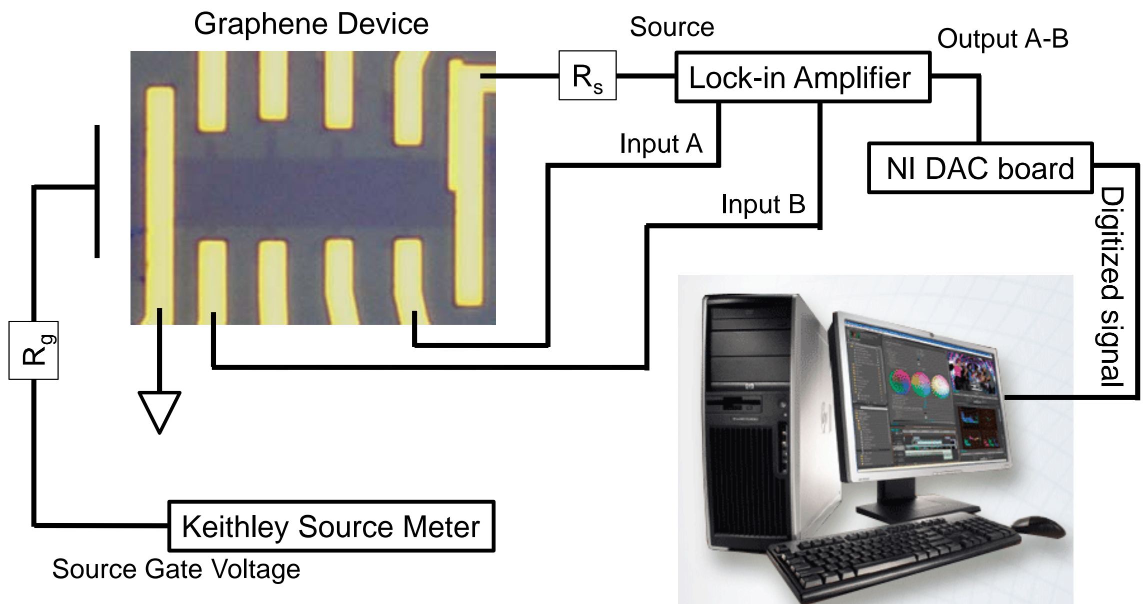

Figure 4.5.2 Schematics of a quasi-DC measurement of the electronic properties of graphene. A low frequency AC voltage applied through the resistor R_s is acting as a current source; R_g is a protection resistor in case a short circuit happened between the device and the gate. Typical values for the resistors are: R_s = 1MΩ, R_g = 100MΩ.

The experimental setup for *in situ* electronic transport measurements in ultra-high vacuum is shown in Figure 4.5.3. The graphene field effect device is mounted on the variable temperature stage (the LT-3B cryostat, see Figure 4.2.1 and Figure 4.2.2) with its cleaned surface exposed in the UHV chamber, and its electrical contacts connected to a lock-in amplifier outside of the chamber. A Potassium getter is mounted on the opposite side of the chamber to deposit controlled amounts of potassium on the graphene device to study the effects of charged impurities scattering (details in Chapter 5); a sputter gun is used with very low pressure of noble gas, introduced by a leak valve, to produce low density and low energy ions to create atomic-scale defects in graphene (details in Chapter 6); water molecules could be leaked in to the chamber an adsorbed on graphene at low temperature to study the effect of increased screening (details in Appendix A3). The temperature of the device can be controlled by the variable temperature stage to study the effect of phonons (details in Chapter 7). The Mass Spectrometer (Residual Gas Analyzer 200 from Stanford Research Systems) is used to monitor the gas species in the chamber, the deposition rate of potassium and the pressures of noble gas and water. The Faraday Cup is used to measure the ion flux to the sample.

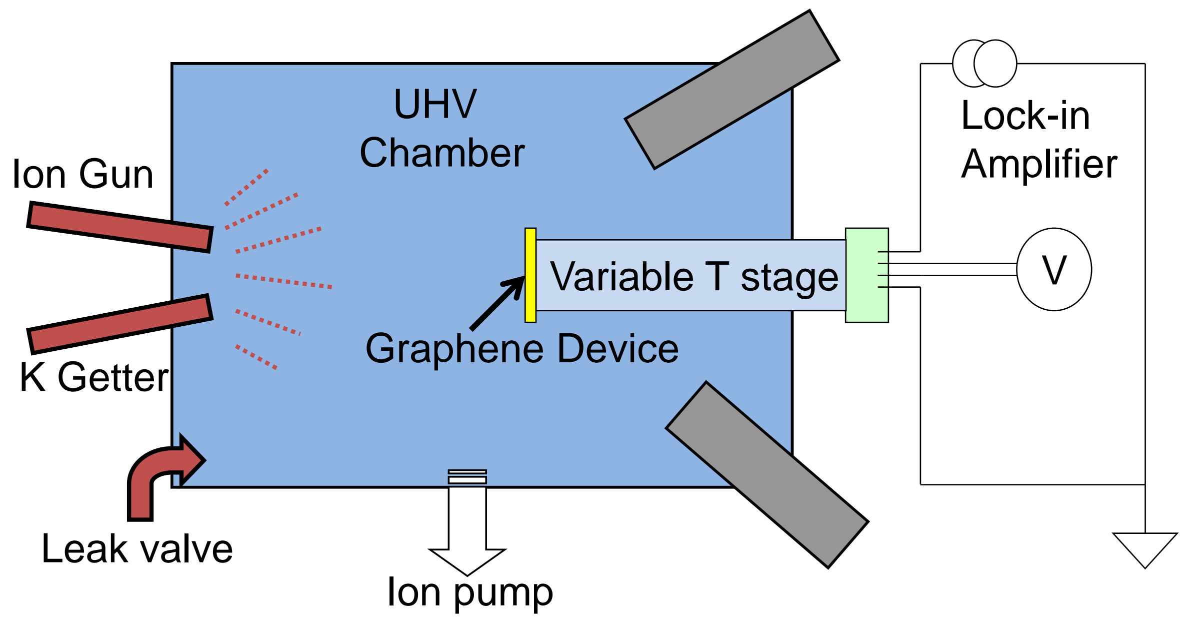

Figure 4.5.3 Schematics of experimental setup for *in situ* electronic transport measurement in ultra-high vacuum with variable temperature and surface conditions.

Chapter 5: Charged impurity scattering in graphene[3]

Since the experimental realization of graphene [25], extensive theoretical work has focused on short-range disorder [49, 50, 60, 81], "ripples" [65, 82], or charged impurities [49-54, 83, 84] to explain the experimentally-observed [25, 31, 37, 47, 85] carrier density-dependent conductivity $\sigma(n)$, and its minimum value σ_{min} near twice the conductance quantum $4e^2/h$. Here we vary the density of charged impurities n_{imp} on clean graphene [38] by deposition of potassium in ultra-high vacuum. At non-zero carrier density, charged impurity scattering produces the ubiquitously observed [25, 31, 37, 44, 47, 85] linear $\sigma(n)$ with the theoretically-predicted magnitude. The predicted asymmetry [54] for attractive vs. repulsive scattering of Dirac fermions is observed. σ_{min} occurs not at the carrier density which neutralizes n_{imp}, but rather the carrier density at which the average impurity potential is zero [53]. σ_{min} decreases initially with n_{imp}, reaching a minimum near $4e^2/h$ at non-zero n_{imp}, indicating that σ_{min} in present experimental samples does not probe Dirac-point physics [31, 44, 56, 57] but rather carrier density inhomogeneity due to the impurity potential [50, 52, 53].

Several theoretical works [49-53, 83, 84] have predicted charged impurity scattering in graphene to produce $\sigma(n)$ of the form

$$\sigma(n) = Ce\left|\frac{n}{n_{imp}}\right| + \sigma_{res} \tag{5.1}$$

[3] This chapter was adapted from: J.-H. Chen, C.Jang, S.Adam, M.S. Fuhrer, and E.D. Williams, and M.Ishigami, *Nature Physics* **4**, 377 (2008)

where C is a constant, e the electronic charge, and σ_{res} the residual conductivity at $n = 0$ (this last term was predicted only in refs. [83, 84]). Hwang, et al. [52] first calculated the screened Coulomb potential within the random phase approximation, and use the results to determine $C = 5 \times 10^{15}\ V^{-1}s^{-1}$. Novikov [54] noted that, beyond the Born approximation used in Ref. [52], an asymmetry in C for attractive vs. repulsive scattering (electron vs. hole carriers) is expected for Dirac fermions. Experimentally, the behavior described by equation (1) is ubiquitously observed [25, 31, 37, 44, 47, 85] in graphene, strongly suggesting charged impurity scattering is the dominant scattering mechanism in present samples. Here we provide the first direct verification of equation (1) for charged impurity scattering in graphene, and determine the constant C. We also observe the expected asymmetry for attractive vs. repulsive scattering for Dirac fermions [54].

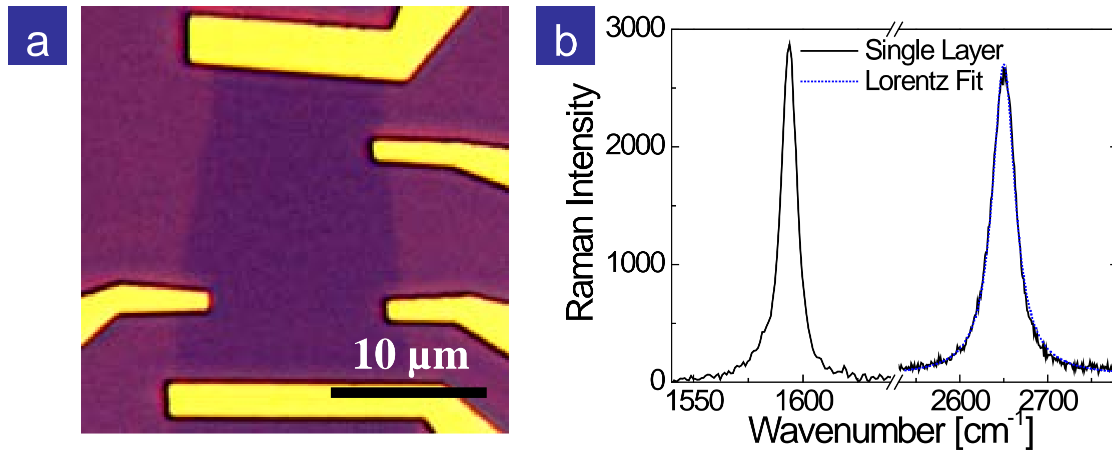

Figure 5.1 Optical micrograph and Raman spectrum of a graphene device. (a) Optical micrograph of the device. (b) 633 nm micro-Raman shift spectrum acquired over the device area, with Lorentzian fit to the D' peak, confirming that the device is made from single-layer graphene (vertical scale is same throughout b).

At low carrier density, the conductivity does not vanish linearly, but rather saturates to a constant value near $4e^2/h$ [44]. Early theoretical work [56, 57] on massless Dirac fermions predicted $\sigma_{min} = 4e^2/\pi h$ for vanishing disorder. However, in the presence of charged impurities, a finite conductivity ~$4e^2/h$ is predicted over a plateau of width ΔV_g [50, 52, 53]. Here we measure experimentally the dependence on n_{imp} of σ_{min}, ΔV_g and the gate voltage $V_{g,min}$ at which the minimum conductivity occurs, and find agreement with theoretical predictions [50, 52, 53], indicating that disorder due to charged impurities is the relevant physics at the minimum conductivity point in present samples.

Figure 5.1a shows the graphene device used in this study, and Figure 5.1b shows its micro-Raman spectrum; the single Lorentzian D' peak confirms that the device is single-layer graphene [76] (see Methods). To vary the density of charged impurities, the device was dosed with a controlled potassium flux in sequential 2-second intervals at a sample temperature T = 20 K in ultra-high vacuum (UHV). The gate-voltage-dependent conductivity $\sigma(V_g)$ was measured *in situ* for the pristine device, and again after each doping interval. After several doping intervals, the device was annealed in UHV to 490 K to remove weakly adsorbed potassium [86], then cooled to 20 K and the doping experiment repeated; four such runs (Runs 1-4) were performed in total.

Figure 5.2 shows the conductivity vs. gate voltage for the pristine [38] device and at three different doping concentrations at 20K in UHV for Run 3 (see also Supplementary Information for measurements on a second device). Upon K-doping, (1) the mobility decreases, (2) $\sigma(V_g)$ becomes more linear, (3) the mobility asymmetry

for holes vs. electrons increases, (4) the gate voltage of minimum conductivity $V_{g,min}$ shifts to more negative gate voltage, (5) the width of the minimum conductivity region in V_g broadens, and (6) the minimum conductivity σ_{min} decreases, at least initially (see also Figure 5.5). In addition, (7) the linear $\sigma(V_g)$ curves extrapolate to a finite σ_{res} at $V_{g,min}$. All of these features have been predicted [49-53, 83, 84] for charged impurity scattering in graphene, we will discuss each in detail below.

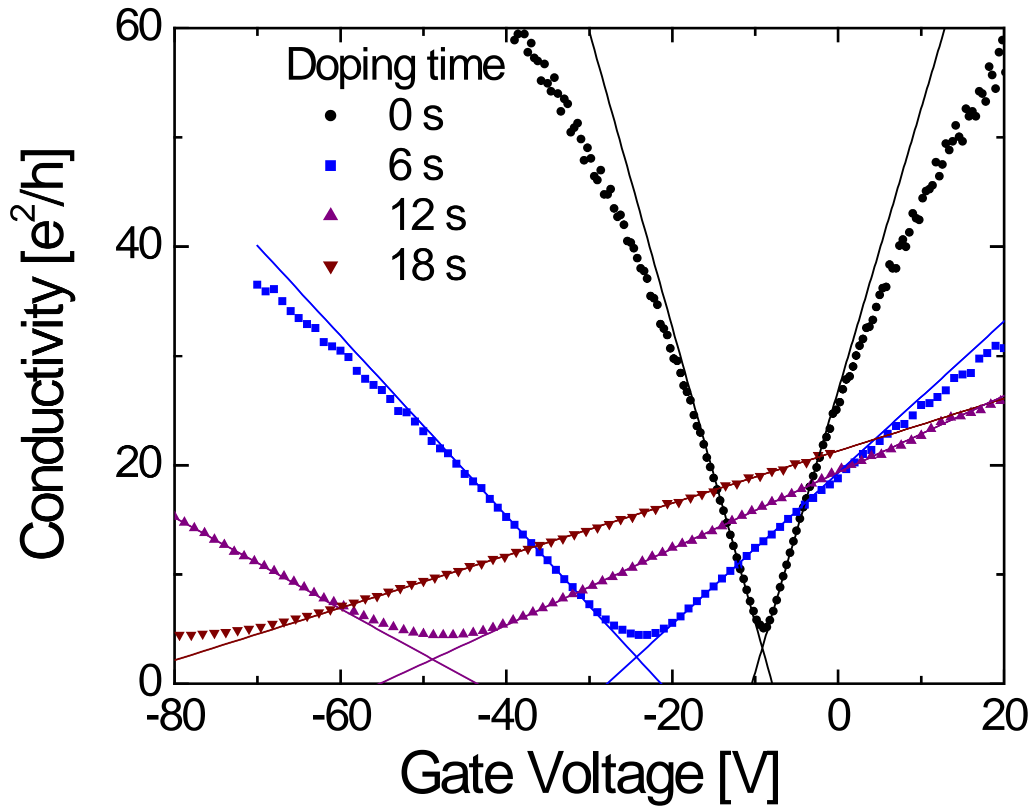

Figure 5.2 Potassium doping of graphene. The conductivity (σ) vs. gate voltage (V_g) curves for the pristine sample and three different doping concentrations taken at 20K in ultra high vacuum are shown. Data are from Run 3. Lines are fits to equation (1), and the crossing of the lines defines the points of the residual conductivity and the gate voltage at minimum conductivity (σ_{res}, $V_{g,min}$) for each data set. The variation of σ_{min} with impurity concentration is shown in Figure 5.5.

Effects (4) and (5) was observed in a previous study in which graphene was exposed to molecular species [87]. However, the authors reported no changes in mobility, concluding that charged impurity scattering contributes negligibly to the mobility of graphene. As discussed further in Supplementary Information, the previous experiments did not control the environment and had low initial sample mobility. The failure to observe effects (1) - (3) therefore is most likely due to the presence of significant concentrations of *both* positively and negatively charged impurities[87, 88], though the presence of water and resist residue[38] may also be contributing factors[87].

We first examine the behavior of $\sigma(V_g)$ at high carrier density. For V_g not too near $V_{g,min}$, the conductivity can be fit (see Figure 5.2) by

$$\sigma(V_g) = \begin{cases} \mu_e c_g \left(V_g - V_{g,\min}\right) + \sigma_{res} & V_g > V_{g,\min} \\ -\mu_h c_g \left(V_g - V_{g,\min}\right) + \sigma_{res} & V_g < V_{g,\min} \end{cases} \tag{5.2}$$

where μ_e and μ_h are the electron and hole field-effect mobilities, and c_g is the gate capacitance per unit area, 1.15×10^{-4} F/m^2, and σ_{res} is the residual conductivity which is determined by the fit. The mobilities are reduced by an order of magnitude during each run, and recover upon annealing. The electron mobilities ranged from 0.081 to 1.32 m^2/Vs over the four runs, nearly covering the range of mobilities reported to date in the literature (~0.1 to 2 m^2/Vs) [31, 44, 85].

For uncorrelated scatterers, the mobility depends inversely on the density of charged impurities, $1/\mu \propto n_{imp}$, and equations (1) and (2) are identical. We assume n_{imp} varies linearly with dosing time t as potassium is added to the device. In Figure 5.3 we plot $1/\mu_e$ and $1/\mu_h$ vs. t, which are linear, in agreement with $1/\mu \propto n_{imp}$, hence

verifying that equation (1) describes charged impurity scattering in graphene. We estimate the dosing rate dn_{imp}/dt = $(2.6\sim3.2)\times10^{15}$ $m^{-2}s^{-1}$, and the maximum concentration of $(1.4\sim1.8)\times10^{-3}$ potassium per carbon (see Supplementary Information). From this point, we parameterize the data by $1/\mu_e$, proportional to the impurity concentration (the data set for μ_e is more extensive than μ_h because of the limited V_g range accessible experimentally).

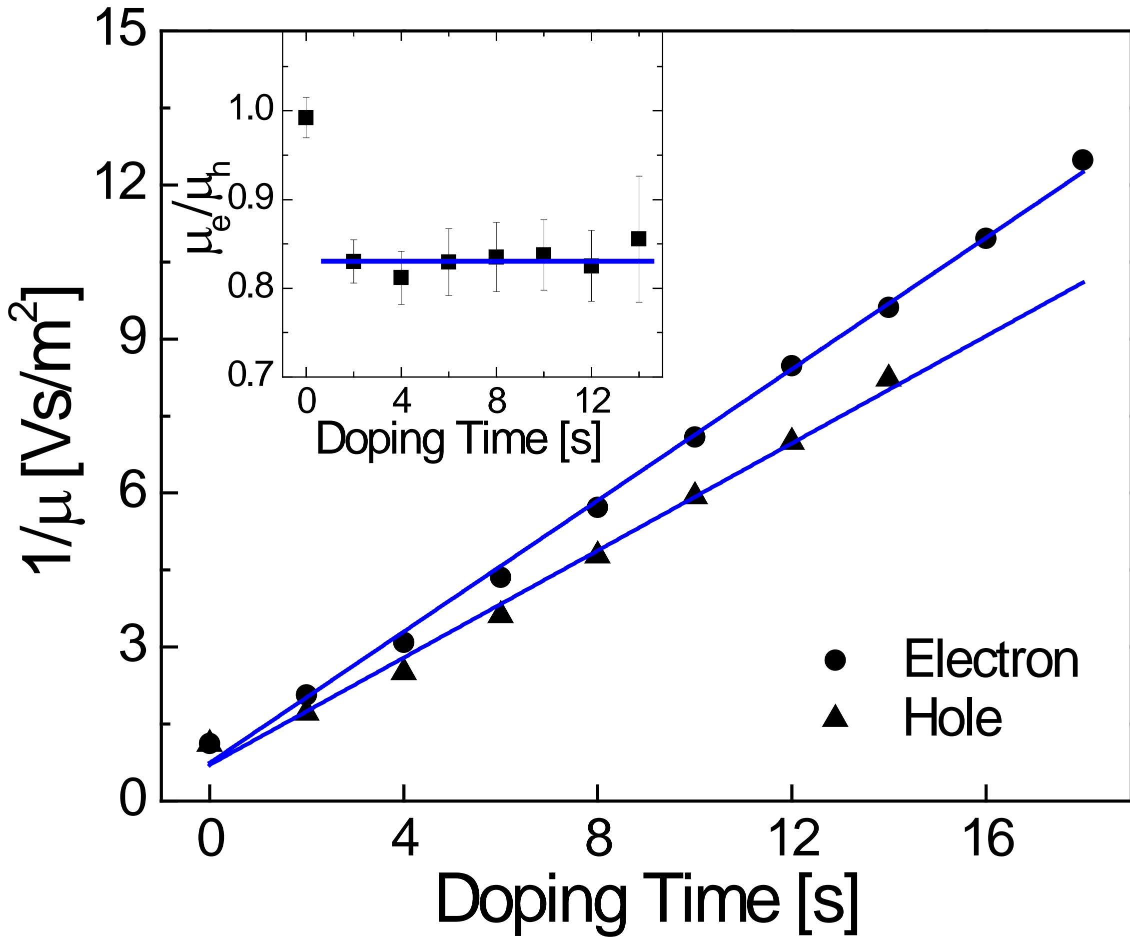

Figure 5.3 Inverse electron mobility $1/\mu_e$ and hole mobility $1/\mu_h$ vs. doping time. Experimental error determined from standard error propagation is less than 4% (see Methods). Lines are linear fits to all data points. Inset: The ratio of μ_e to μ_h vs. doping time. Error bars represent experimental error in determining the mobility ratio from the fitting procedure (see Methods). Data are from run 3 (same as Figure 5.2).

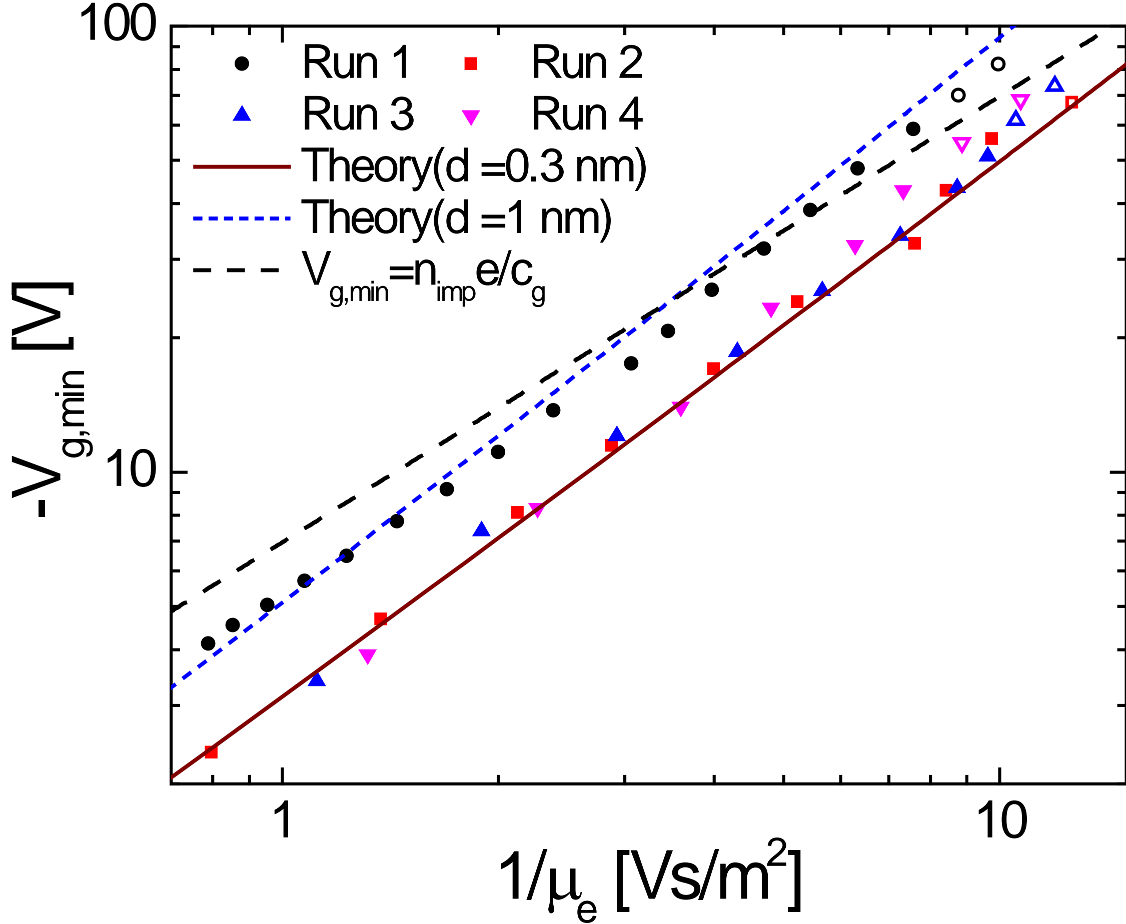

Figure 5.4 Shift of minimum conductivity point with doping. The gate voltage of minimum conductivity $V_{g,min}$ is shown as a function of inverse mobility, which is proportional to the impurity concentration. All four experimental runs are shown. Each data set has been shifted by a constant offset in $V_{g,min}$ in order to make $V_{g,min}(1/\mu_e \rightarrow 0) = 0$, to account for any rigid threshold shift. The offset (in volts) is -10, 3.1, 5.6, and 8.2 for the four runs, respectively, with the variation likely to be due to accumulation of K in the SiO_2 on successive experiments. The open dots are $V_{g,min}$ obtained directly from the $\sigma(V_g)$ curves rather than fits to equation (1) because the linear regime of the hole side of these curves is not accessible due to heavy doping. The solid and short-dashed lines are from the theory of Adam et al.[53] for an impurity-graphene distance d = 0.3 nm (solid line) and d = 1 nm (short-dashed line), and approximately follow power laws with slopes 1.2 and 1.3, respectively. The long-dashed line shows the linear relationship $\Delta V_{g,min} = n_{imp}Ze/c_g$ where n_{imp} = $(5\times10^{15}\ V^{-1}s^{-1})/\mu$ and $Z = 1$.

The inset to Figure 5.3 shows that, although the μ_e and μ_h are not identical, their ratio is fairly constant at μ_e/μ_h = 0.83 ± 0.01 (see Methods). Novikov[54]

predicted $\mu_e/\mu_h = 0.37$ for an impurity charge $Z = 1$, however the asymmetry is expected to be reduced when screening by conduction electrons is included.

As K-dosing increases and mobility decreases, the linear behavior of $\sigma(V_g)$ (see Figure 5.2) associated with charged impurity scattering dominates, as predicted theoretically[52]. At the lowest K-dosing level, sub-linear behavior is observed for large $|V_g - V_{g,min}|$ as anticipated. The dependence of the conductivity on carrier density $n \propto |V_g - V_{g,min}|$ is expected to be $\sigma \propto n^a$ with $a = 1$ for charged impurities, and $a < 1$ for short-range and ripple scattering (see Supplementary Information). Adding conductivities in inverse according to Matthiessen's rule indicates that scattering other than by charged impurities will dominate at large n, with the crossover occurring at larger n as n_{imp} is increased[52]. A previous study[31] also found more linear $\sigma(V_g)$ for devices with lower mobility. Thus, our data indicate that the variation in observed field effect mobilities of graphene devices is determined by the level of unintentional charged impurities.

We now examine the shift of the curves in V_g. Figure 5.4 shows $V_{g,min}$ as a function of $1/\mu_e$. Run 1 differs from Runs 2-4, presumably due to irreversible changes as potassium reacts with charge traps on silicon oxide and/or edges and defects of the graphene sheet. After Run 1, subsequent runs are very repeatable, other than an increasing rigid shift to more negative voltage in the initial gate voltage of minimum conductivity. (The same distinction between first and subsequent experiments is seen in Figure 5.5 as well.) One might expect that the minimum conductivity would occur at the induced carrier density which precisely neutralizes the charged impurity density: $n = -Zn_{imp}$, or $\Delta V_{g,min} = -n_{imp}Ze/c_g$ [87], where e is the

elementary charge, and Ze is the charge of the potassium ion. This prediction is shown as the long-dashed line in Figure 5.4; the experimental data show a distinctly different effective power-law dependence. Adam, et al.[53] proposed that the minimum conductivity in fact occurs at the added carrier density $\bar{n}$ at which the average impurity potential is zero, i.e. $\Delta V_{g,\min} = -\bar{n}e/c_g$, where $\bar{n}$ is a function of n_{imp}, the impurity spacing d from the graphene plane, and the dielectric constant of the SiO_2 substrate. The theory also assumes that $Z = 1$; experimentally, a reasonable evaluation[13] of Z for dilute potassium on graphite is ~0.7. The theoretical lines in Figure 5.4 are given by the *exact result* of Adam et al.[53], and follow an approximate power-law behavior of $\Delta V_{g,\min} \propto n_{imp}^b$ with b = 1.2~1.3, which agrees well with experiment. The only adjustable parameter is the impurity-graphene distance d; we show the results for d = 0.3 nm (a reasonable value for the distance of potassium on graphene[10, 13, 89]), and d = 1.0 nm (the value used by Adam, et al.). Since $\Delta V_{g,\min}$ gives an independent estimate of n_{imp}, the quantitative agreement in Figure 5.4 verifies that $C = 5\times10^{15}$ $V^{-1}s^{-1}$ in equation (1), as expected theoretically.

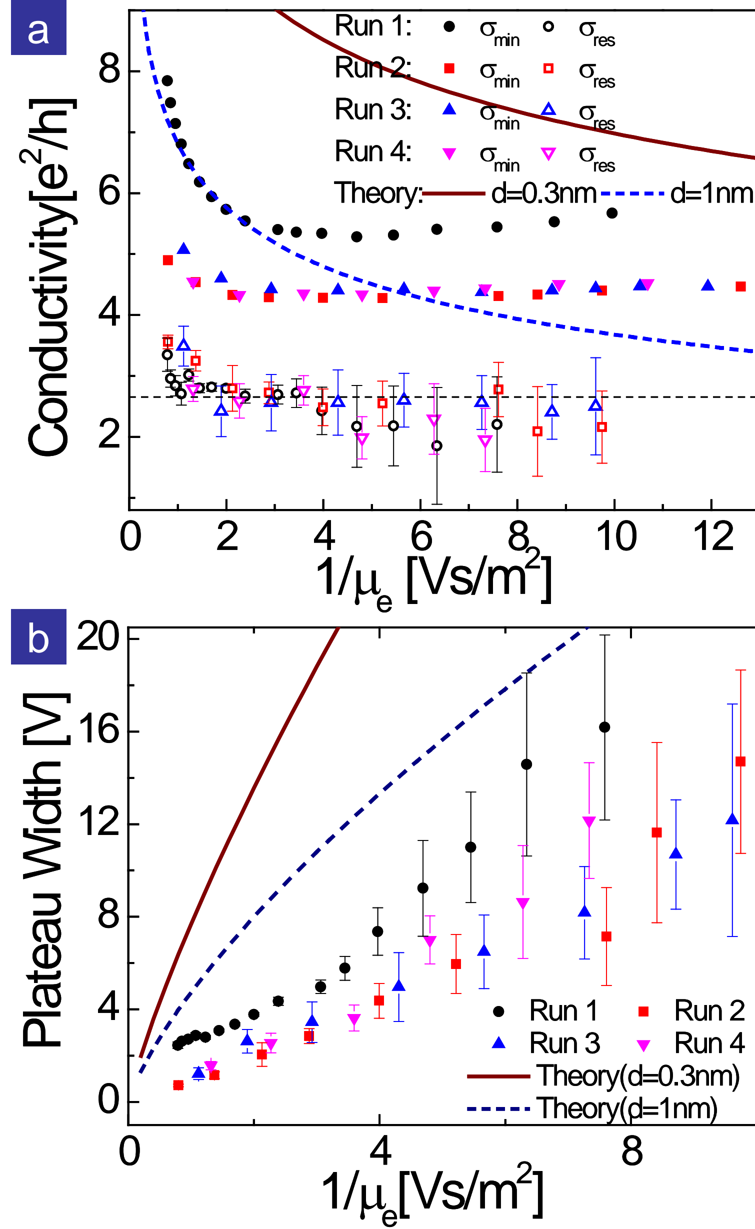

Figure 5.5 Change in behavior near minimum conductivity point with doping. (a) The minimum conductivity and the residual conductivity (defined in text) as a function of $1/\mu_e$ (proportional to the impurity density). (b) The plateau width ΔV_g as a function of $1/\mu_e$. In a and b, data from all four experimental runs are shown, as well as the theoretical predictions of the minimum conductivity and plateau width from Adam et al.[53] for d = 0.3 nm (solid line) and d = 1 nm (short-dashed line). Error bars represent experimental error in determining σ_{res} and ΔV_g from the fitting procedure (see Methods); σ_{min} is measured directly.

We now turn to the behavior near the point of minimum conductivity. Figure 5.5a shows the minimum conductivity σ_{min} and residual conductivity σ_{res} as a function of $1/\mu_e$, and Figure 5.5b shows the plateau width ΔV_g as a function of $1/\mu_e$; ΔV_g is the difference between the two values of V_g for which $\sigma_{min} = \sigma(V_g)$ in equation (2). Also shown are the predictions from the theory of Adam et al.[53] for σ_{min} and ΔV_g. Finite σ_{res} has been predicted theoretically[83, 84] for graphene with charged impurities; however, the magnitude has not been calculated. The minimum conductivity drops upon initial potassium dosing, and shows a broad minimum near $4e^2/h$ before gradually increasing with further exposure. Notably, the cleanest samples show σ_{min} significantly greater than $4e^2/h$, and strongly dependent on charged impurity density, indicating that the universal behavior[56, 57] of σ_{min} associated with the Dirac point is not observed even in the cleanest samples. The irreversible change in the value of σ_{min} between Run 1 and Runs 2-4 is larger than the entire variation within Runs 2-4. This difference between initial and subsequent runs indicates that the initial K-dosing and anneal cycle introduces other types of disorder (possibly short-range scatterers induced by irreversible chemisorption of potassium on defects or reaction of potassium with adsorbates) that have a comparable or greater impact on σ_{min} than charged impurities. That, for some disorder conditions (Run 1), σ_{min} varies significantly with n_{imp}, but for other conditions (Runs 2-4) the decrease in σ_{min} saturates rapidly with increasing n_{imp}, and is nearly constant for a very broad range of doping, suggests that the substantial variations reported in the literature (*i.e.* some groups report that σ_{min} is a universal value[44], while other groups observe variation in σ_{min} from sample to sample[31]) are likely due to poor control of the chemical

environment of the devices measured. The observed residual conductivity σ_{res} is finite and surprisingly constant (see Figure 5.5a); it is only weakly dependent on doping, and shows little variation between the first run and subsequent runs. Finite σ_{res} has been predicted theoretically[83, 84] for graphene with charged impurities; however, the magnitude has not been calculated. The change of ΔV_g with doping (see Figure 5.5b) agrees only qualitatively with the theory, which predicts somewhat larger values and a sublinear dependence on doping. However, the quantitative disagreements between experiment and theory in Figures 5.5a and 5.5b are connected: mobility, minimum conductivity, and residual conductivity determine ΔV_g.

In conclusion, the dependence of conductivity of graphene on the density of charged impurities has been demonstrated by controlled potassium doping of clean graphene devices in UHV at low temperature. The minimum conductivity depends systematically on charged impurity density, decreasing upon initial doping, and reaching a minimum near $4e^2/h$ only for non-zero charged impurity density, indicating that the universal conductivity at the Dirac point[44, 56, 57] has not yet been probed experimentally. The high-carrier density conductivity is quantitatively consistent with theoretical predictions for charged impurity scattering in graphene[49-53, 83, 84]. The addition of charged impurities produces a more linear $\sigma(V_g)$, and reduces the mobility, with the constant $C = \mu n_{imp} = 5\times10^{15}$ $V^{-1}s^{-1}$, in excellent agreement with theory. The asymmetry for repulsive vs. attractive scattering predicted for massless Dirac quasiparticles[54] is observed for the first time. Finally, the minimum conductivity point[53] occurs at the applied gate voltage at which the

average impurity potential is zero and not at the voltage at which the gate-induced carrier density neutralizes the impurity charge.

Other observations indicate the need for fuller experimental and theoretical understanding. The irreversible changes in the behavior around $V_{g,min}$ between the first and subsequent doping runs indicate that the precise value of the minimum conductivity depends on the interplay of more than one type of disorder, and hence cannot be explained by existing theories[49, 50, 52, 53, 60, 65, 81, 83, 84]. An interesting new feature, the residual conductivity, may point to physics beyond the simple Boltzmann transport picture[83, 84]. Further experiments including introducing short-range (neutral) scatterers to graphene will be useful in addressing these questions. Full understanding may require scanned-probe studies of graphene under well-controlled environmental conditions[38], which can completely characterize the disorder due to defects, charged and neutral adsorbates, and ripples, as well as probe the electron scattering from each[90].

Methods

The method of fabricating cleaned graphene devices can be found in chapter 4, section 4.1; the Helitran LT-3B used in the experiment is described in chapter 4, section 4.2; the *in situ* transport measurement in UHV is described in chapter 4, section 4.5.

Experiments are carried out at pressures lower than 5×10^{-10} torr and device temperature T = 20 K. Potassium doping is accomplished by passing a current of 6.5A through a getter (SAES Getters Inc. http://www.saesgetters.com/) for 40 seconds

before the shutter is opened for 2 seconds. The getter temperature during each potassium dosage was 763±5 K as measured by optical pyrometry. The stability of the potassium flux was monitored by a residual gas analyzer positioned off-axis and behind the sample (see Supplementary Information). All measurements shown here were performed on one four-probe device shown in Figure 5.1a, though several two-probe devices showed similar behavior.

Conductivity σ is determined from the measured four-probe sample resistance R using $\sigma = (L/W)(1/R)$. Because the sample is not an ideal Hall bar, there is some uncertainty in the (constant) geometrical factor L/W. We estimate $L/W = 0.80 \pm 0.09$, where the error bars represent ± one standard deviation. This 11% uncertainty in L/W translates into an 11% uncertainty in the vertical axes of Figures 5.2 and 5.3, the horizontal axes of Figures 5.4 and 5.5b, and both axes of Figure 5.5a. Such scale changes are comparable to the spread among different experimental runs, and do not alter the conclusions of the paper. Notably, the uncertainty represents a systematic error, so *relative* changes in e.g. the minimum conductivity with charged impurity density are still correct.

Best fits to equation (1) were determined using a least square linear fit to the steepest regime in the $\sigma(V_g)$ curves. The steepest regime of the $\sigma(V_g)$ curves was determined by examining $d\sigma/dV_g$; the fit was performed over a 2 V interval in V_g around the maximum of $d\sigma/dV_g$. Other criteria for determining the maximum field effect mobility give similar results. The experimental errors in μ_e and μ_h are determined by the fitting procedure described above; the errors in $V_{g,min}$, σ_{res}, the ΔV_g (plateau width), and μ_e/μ_h are then calculated using equation (1) and standard error

propagation. The errors (standard deviation) in μ_e, μ_h and $V_{g,min}$ were typically less than 4%. σ_{min} is measured directly, and has less than 1% error. Errors bars (± one standard deviation) are shown in the inset of Figure 5.2 for the errors in μ_e/μ_h, and in Figure 5.5 for the errors in σ_{res} and ΔV_g. The weighted mean of μ_e/μ_h at non-zero dosing time is 0.83 and the weighted standard deviation of the mean is 0.01.

Chapter 6: Defect scattering in graphene[4]

Abstract

Irradiation of graphene on SiO_2 by 500 eV Ne and He ions creates defects that cause intervalley scattering as evident from a significant Raman *D* band intensity. The defect scattering gives a conductivity proportional to charge carrier density, with mobility decreasing as the inverse of the ion dose. The mobility decrease is four times larger than for a similar concentration of singly charged impurities. The minimum conductivity decreases proportional to the mobility to values lower than $4e^2/\pi h$, the minimum theoretical value for graphene free of intervalley scattering. Defected graphene shows a diverging resistivity at low temperature, indicating insulating behavior. The results are best explained by ion-induced formation of lattice defects that result in mid-gap states.

[4]This chapter was adapted from: J.-H. Chen, W.G. Cullen, C.Jang, M.S. Fuhrer, and E.D. Williams, Phys. Rev. Lett. (in press), preprint at arXiv: 0903.2602 (2009)

The strong carbon-carbon sp^2 bonds which provide graphene with high intrinsic strength [29] and make possible the isolation of single atomic layers [45], also result in a very low density of lattice defects in graphene prepared by mechanical exfoliation [38, 91]. However, lattice defects in graphene are of great theoretical interest [61, 63] as a potential source of intervalley scattering, which in principle transforms graphene from a metal to an insulator [92, 93]. Lattice defects are also likely to be present in various concentrations in graphene synthesized by reduction of graphene oxide [94, 95], chemical vapor deposition [20, 96], or segregation of carbon on the surface of SiC [24], hence it is important to understand their impact on electronic transport.

Here we show that ion irradiation-induced defects in graphene cause a significant intensity in the Raman *D* band associated with intervalley electron scattering [76, 97, 98] and give rise to a constant mobility, similar to the effect of charged impurities, but with a magnitude 4 times lower than for a similar concentration of singly charged impurities. This result is in contrast to the carrier-density-independent conductivity for weak point disorder [39, 42] but consistent with the theory of strong scattering by mid-gap states [61, 63]. Unlike charged impurities [34], lattice defects (1) do not change the residual charge density in electron-hole puddles; (2) greatly depress the minimum conductivity, even below $4e^2/\pi h$ (the theoretical minimum value of the conductivity at the Dirac point in the absence of intervalley scatteing [92]); and (3) induce insulating temperature dependence of the conductivity.

Transport with constant mobility is predicted for both charged impurity scattering and scattering by mid-gap states. Charged-impurity disorder in graphene results in a conductivity

$$\sigma_c = ne\mu_c = \frac{2e^2}{h}\frac{n}{n_c}\frac{1}{G(2r_s)} \qquad (6.1)$$

where e is the electronic charge, h the Planck's constant, n_c the charged impurity density, r_s the Wigner-Seitz radius and $G(2r_s)$ an analytical function of the dimensionless interaction strength in graphene. For graphene on SiO_2, Eq. (6.1) gives $\mu_c \approx 5\times10^{15}\ V^{-1}s^{-1}/n_c$[34, 53]. The random charged impurity potential also gives rise to electron-hole puddles with a characteristic intrinsic carrier density n^*, which is a function only of n_c, d (the impurity-graphene distance) and r_s, resulting in a minimum conductivity $\sigma_{min} = n^*e\mu_c$. However, strong disorder, modeled as a deep potential well of radius R, is predicted to produce midgap states in graphene[61], and a conductivity which is also roughly linear in n[63]:

$$\sigma_d = ne\mu_d = \frac{2e^2}{\pi h}\frac{n}{n_d}\ln^2(k_F R) \qquad (6.2)$$

where n_d is the defect density and k_F is the Fermi wavevector. A third type of scattering in graphene, weak point disorder, is predicted to give rise to a carrier-density-independent resistivity ρ_s [42], which has been observed experimentally [39].

To investigate the dependence of graphene's conductivity on defect density, cleaned graphene on SiO_2 was irradiated with 500 eV He^+ and Ne^+ ions in ultra-high vacuum (UHV) at low temperature (10K for He^+ irradiation and 40-80K for Ne^+ irradiation), and the conductivity measured *in situ* in UHV to prevent subsequent reaction with molecules from the gas phase (more details in Appendix A4). Ion

irradiation of graphite at these energies produces one atomic-scale defect, most likely a carbon vacancy possibly with a trapped noble-gas atom, per incident ion [99, 100].

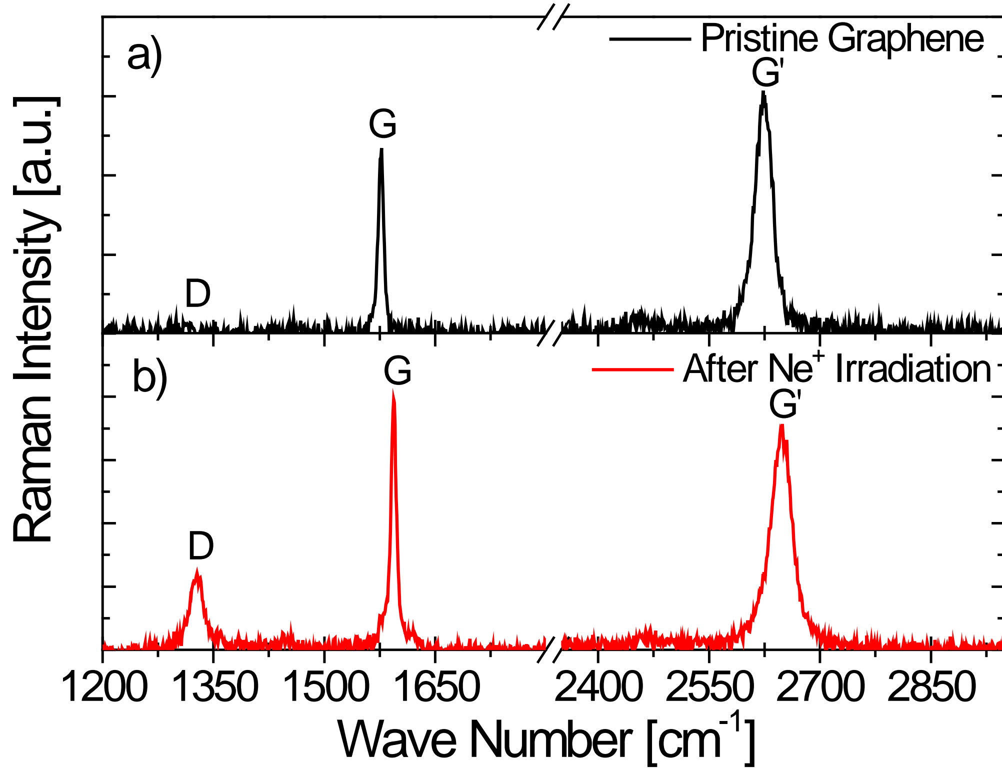

Figure 6.1 Raman spectra (wavelength 633 nm) for (a) pristine graphene and (b) graphene irradiated by 500 eV Ne^+ ions at a dose of 10^{12} cm^{-2}.

Figure 6.1 shows the Raman spectra, taken under ambient conditions, for a representative graphene sample before irradiation, and after irradiation by Ne^+ at a dose of 10^{12} cm^{-2} (~ 1 Ne^+ per 4×10^3 carbon atoms). The pristine sample shows a Lorentzian *G*' band characteristic of single layer graphene, and no detectable *D* band. Upon irradiation, the appearance of the *D* band indicates significant intervalley scattering [97, 98]. A very rough estimate of the defect spacing can be made using

the empirical formula $L_a = \left[2.4\times10^{-10}\text{nm}^{-3}\right]\lambda^4\left(\frac{I_D}{I_G}\right)^{-1}$, which relates the grain size L_a in disordered graphite, to the ratio of the integrated D and G band intensities I_D and I_G, and λ the excitation wavelength (633 nm) [101]. Applying this formula to our irradiated graphene gives L_a ~ 60 nm, larger than the expected defect spacing of 10 nm, but comparable to the transport mean free path of ~50 nm (see below).

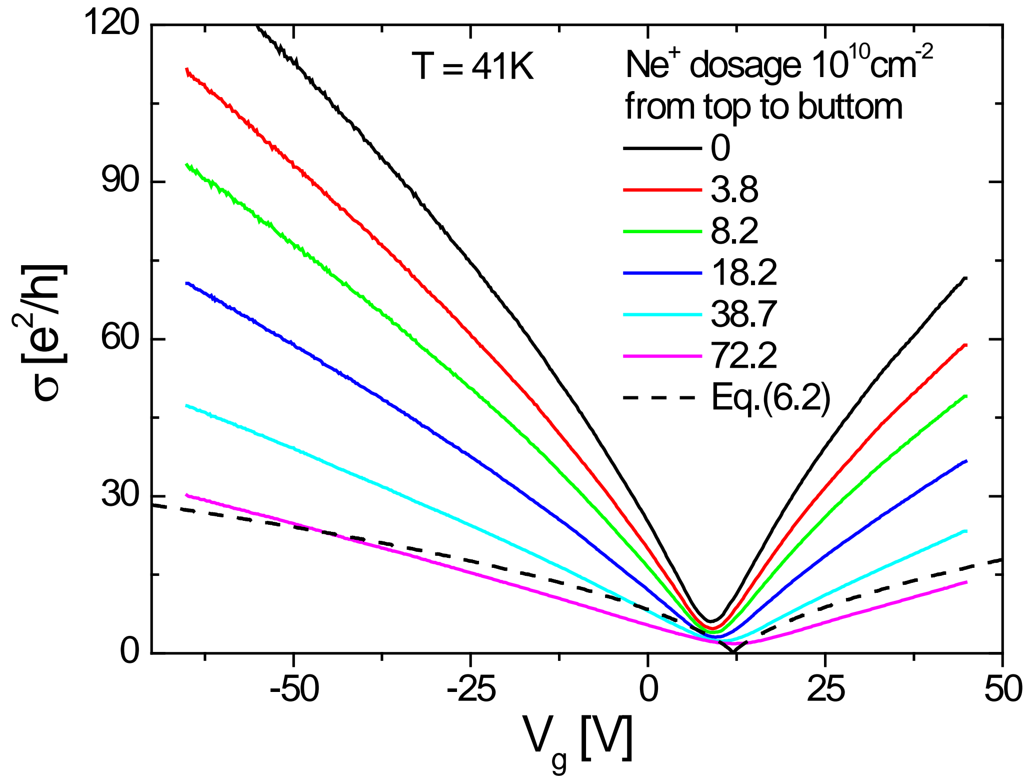

Figure 6.2 Conductivity vs. gate voltage curves for pristine graphene and following Ne^+ ion irradiation doses with cumulative exposures indicated. Irradiation and measurements were performed at $T = 41$K in ultra high vacuum. Dashed curve shows the predictions from Eq. (6.2) with the experimentally extracted defect radius R=2.3Å at defect density $n_d = 7.22\times10^{11}\text{cm}^{-2}$.

Figure 6.2 shows the $\sigma(V_g)$ curves measured for the pristine sample and following sequential Ne^+ irradiation doeses at $T = 41$K in UHV, which is one of the four experimental runs shown in this letter. Also shown are predictions from Eq. (6.2) with the experimentally extracted defect radius R at $n_d = 7.22\times10^{11}$cm^{-2}(see below). Mobility μ and the minimum conductivity σ_{min} partially recover after heating to 485K between each runs, possibly due to annealing or passivation of the defects. To determine μ, and the resistivity ρ_s due to weak point disorder, the $\sigma(V_g)$ curves are fitted to the form $\sigma(V_g)^{-1} = \left[c_g\left(V_g - V_{g.\min}\right)\mu\right]^{-1} + \rho_s$ [39]. We fit the hole side of the $\sigma(V_g)$ curve ($V_g < V_{g,min}$) because the data span a wider V_g range. Figure 6.3a shows $1/\mu$ vs. ion dosage for four experimental runs on two different graphene samples as well as behavior for charged impurities [34, 53]. For the irradiated samples, $1/\mu$ increases linearly with ion dosage as expected for uncorrelated scattering. Fitting yields a proportionality of 7.9×10^{-16} Vs for the Ne^+ irradiation runs and 9.3×10^{-16} Vs for the He^+ irradiation runs and an offset that yields the initial mobility in the graphene prior to each irradiation run (more details in Appendix A4). Assuming mid-gap scattering (Eq. 6.2), at carrier density $n = 2\times10^{12}$ cm^{-2}, the proportionality constant yields the defect radius $R = 2.3$ Å for Ne^+ irradiation and 2.9 Å for He^+ irradiation. If the proportionality is attributed to charged defect scattering (Eq. 6.1), it would require addition of charge Z~4e per incident ion. Figure 6.3b shows the density-independent resistivity ρ_s for the same four experimental runs; ρ_s is very small (on order 10^{-3} h/e^2) and does not change significantly with ion irradiation dose.

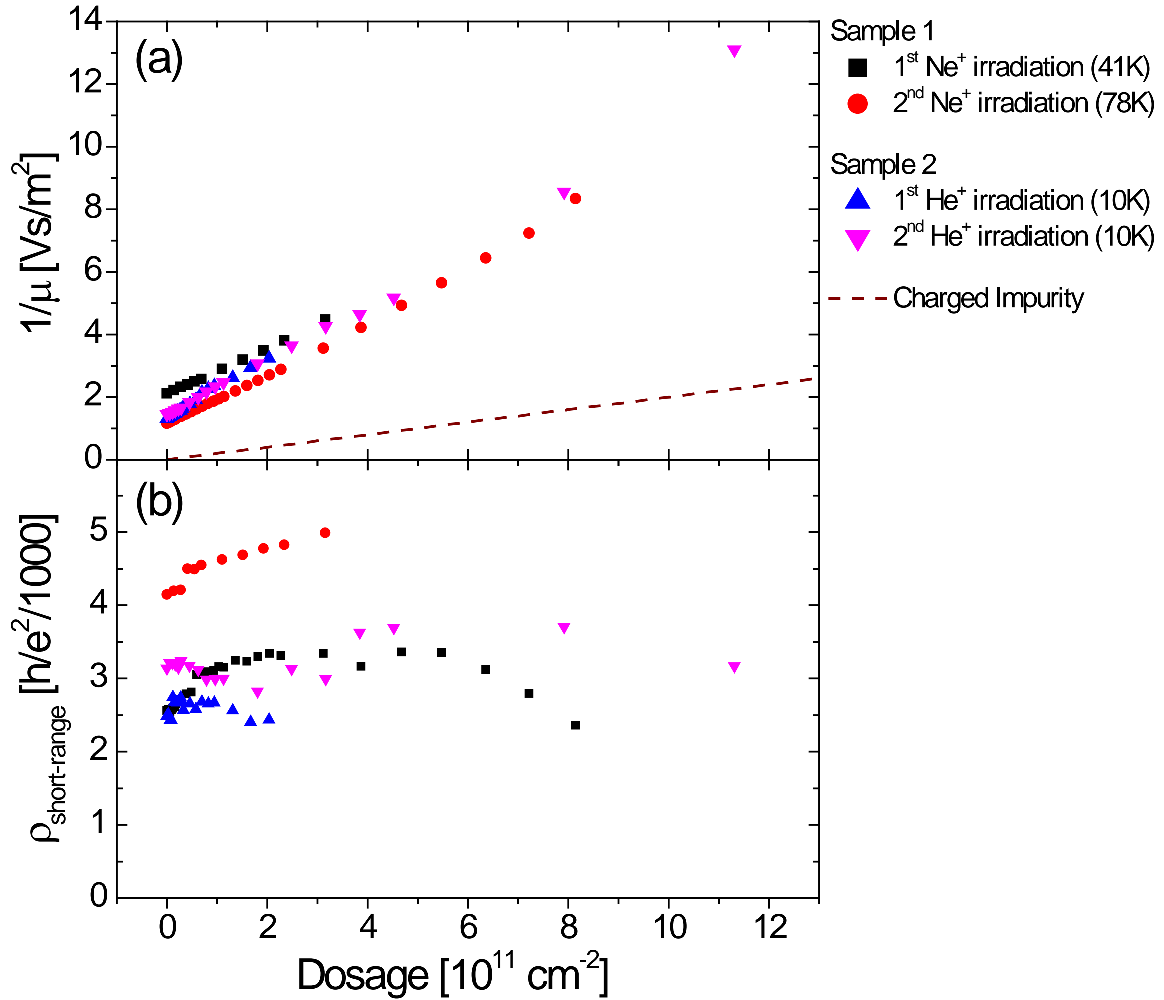

Figure 6.3 (a) Inverse of mobility (1/μ) vs. ion dosage for two Ne^+ irradiation runs on sample 1 and two He^+ irradiation runs on sample 2. Dashed line is behavior for the same concentration of charged impurities (potassium on graphene from Ref. [34]). (b) Density-independent resistivity ρ_s vs. ion dosage.

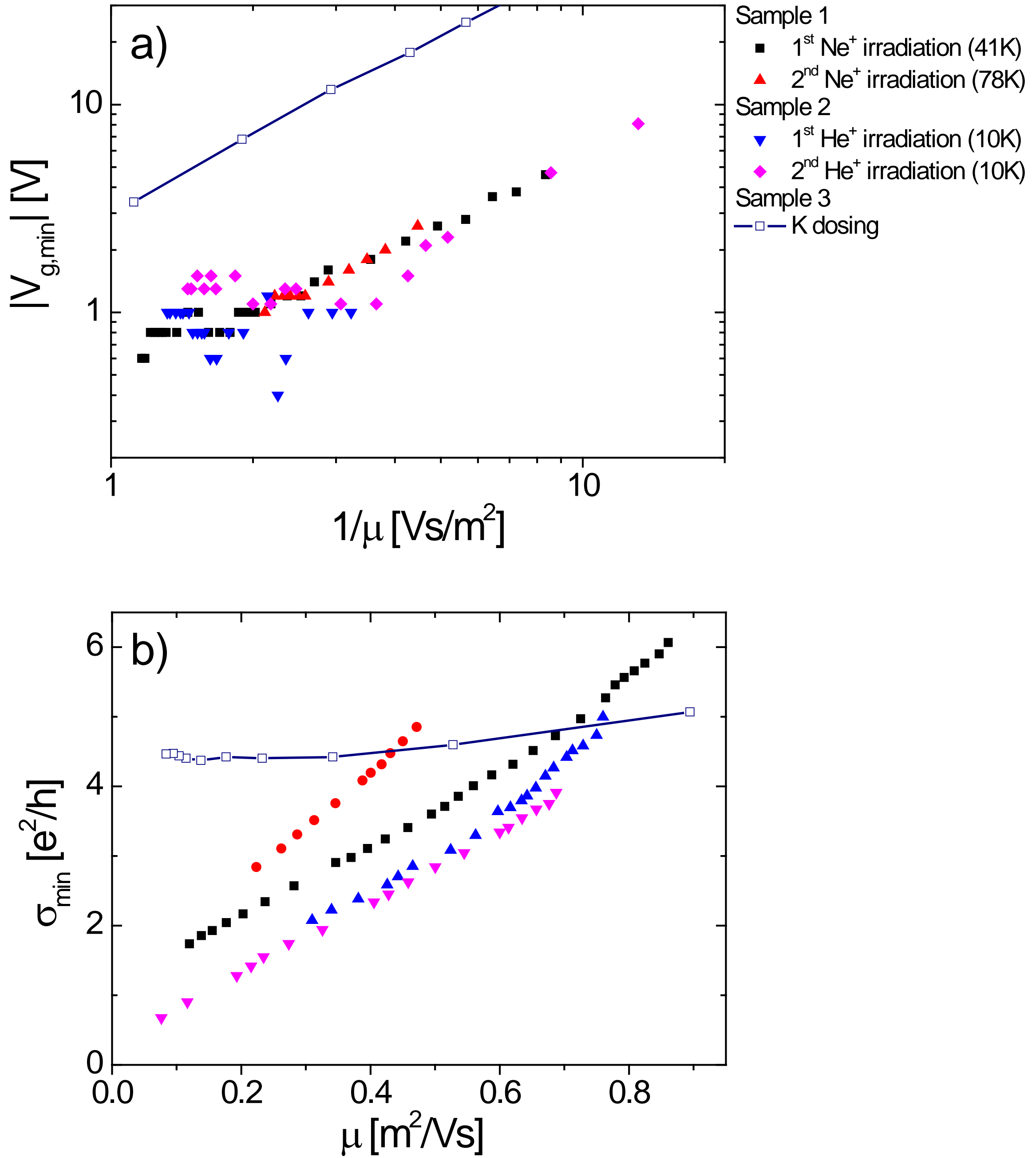

Figure 6.4 (a) Magnitude of the shift in the gate voltage of minimum conductivity ($|\Delta V_{g,min}|$) vs. inverse mobility ($1/\mu$). The shift is with respect to the initial value of $V_{g,min}$, 8.8V and 6.4 V for the Ne^+ and He^+ irradiated samples respectively. (b) Minimum conductivity (σ_{min}) vs. μ for two Ne^+ irradiation runs on sample 1 and two He^+ irradiation runs on sample 2. Data for potassium dosing (Ref.[34]) are shown for comparison. $V_{g,min}$ is positive for ion irradiation, negative for K dosing.

Figure 6.4a shows the change in the voltage of the minimum conductivity $\Delta V_{g,min}$ as a function of the inverse mobility $1/\mu$ (proportional to ion dose) for the four ion irradiation runs. For comparison, the magnitude of $\Delta V_{g,min}$ for potassium (K) dosing (addition of charged impurities) is also shown (data from Ref. [34]), which is 5 times larger than a similar concentration of ion irradiation. Note that $\Delta V_{g,min}$ is positive for ion irradiation, and negative for K dosing. Figure 6.4b shows σ_{min} vs. μ for the same four ion irradiation runs and the K dosing run [34]. In sharp contrast to the charged impurities introduced by K dosing, where $\sigma_{min} = n^* e\mu_c$ varies slowly and non-monotonically because n^* increases with increasing dose (decreasing μ), ion irradiation has a large effect on σ_{min}, reducing σ_{min} roughly proportional to μ.

We now discuss the changes in $\sigma(n)$ upon ion irradiation. The density-independent resistivity (Figure 6.3b) ρ_s~3×10^{-3} h/e^2 and is roughly independent of ion dose; at a carrier density of 10^{12} cm^{-2}, this corresponds to a mean free path >2 μm. The dominant signature, linear $\sigma(n) = ne\mu_d$ with μ_d independent of n, indicates that ion irradiation either creates mid-gap states or charged impurities. However, several observations argue that the observed changes in $\sigma(n)$ are dominated by mid-gap states: (1) The intervalley scattering observed in Raman spectroscopy (Figure 6.1) with scattering length on order 60 nm is inconsistent with ρ_s, but consistent with the associated mobility $\mu = 1300$ cm^2 V^{-1} s^{-1}, at an ambient doping level of ~10^{13} cm^{-2}, from which we calculate a mean free path l ~ 50 nm. This correspondence suggests that the transport mean free path significantly probes intervalley scattering from lattice defects. (2) The sign $\Delta V_{g,min}$ for ion irradiation is positive, opposite to the expectation for deposition of positive ions near the graphene and also opposite to

what was observed for ion-irradiated MOSFETs [102]. (3) The reduction in mobility, if due to charged impurities, would require ~4 added charges per incident ion, while $\Delta V_{g,min}$ indicates only ~1/5 of a net charge per incident ion; this would require a delicate balance between creation of positive and negative impurities, and such balance would need to hold for incident Ne^+ and He^+, which have very different momenta. (4) Within the Boltzmann transport picture, $\sigma_{min} = n^* e\mu$ [53] where the total mobility $\mu = (\mu_d^{-1} + \mu_c^{-1})^{-1}$. The roughly proportional relationship between σ_{min} and μ for ion-irradiated samples indicates that n^*, which is a function of n_c, is nearly independent of ion dose [5].

We therefore conclude that the data of Figure 6.3a are dominated by uncharged lattice defects in graphene. The impurity radius $R \sim 2.3$ Å – 2.9 Å obtained from the linear fits of Figure 6.3 is a reasonable value for single-carbon vacancies generated by ion knock-off [100]. Using this value of R in Eq. (6.2) yields a $\sigma(V_g)$ similar in magnitude to the experimental curve, but with a stronger sublinearty (Figure 6.2). We do not understand this discrepancy, but it may be related to carrier density inhomogeneity persisting to carrier densities much larger than n^* [103], or to the addition of a small amount of deep charged impurities [102] which would contribute a supralinear $\sigma(V_g)$. As discussed in the Appendix A4, the possible trapped noble gas atoms are not likely to contribute significantly to the resistivity in our irradiated graphene sample.

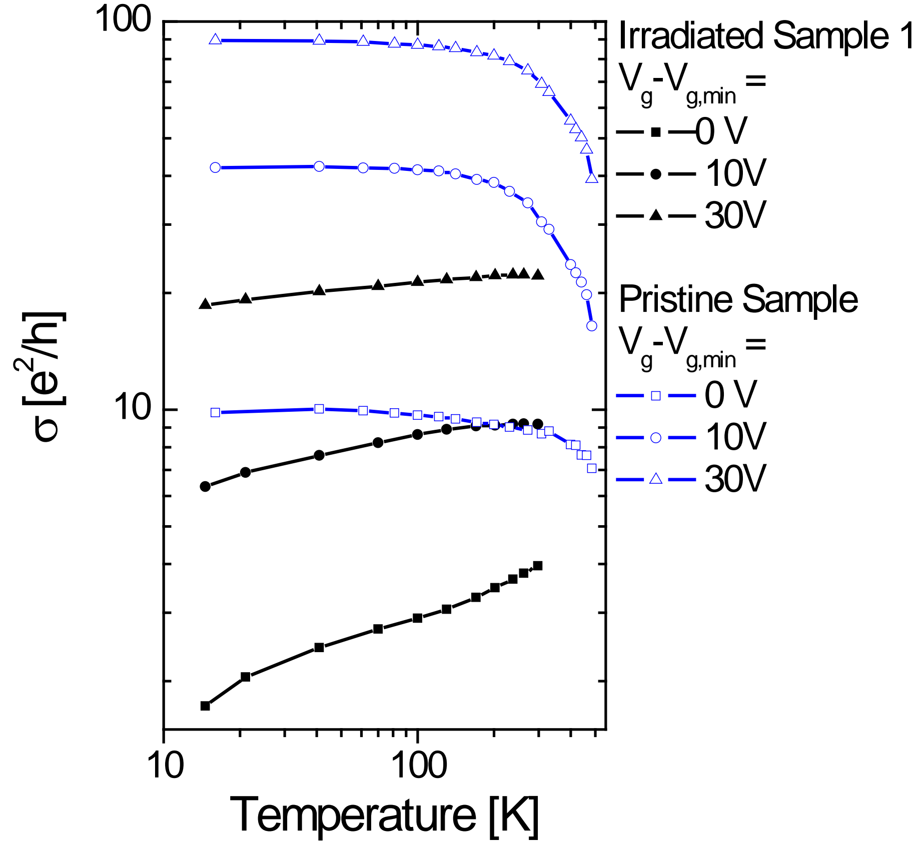

Figure 6.5 Temperature dependence of the conductivity σ(*T*) of pristine (open symbols) and irradiated (solid symbols) graphene at three different gate voltages. σ(*T*) taken on cooling is shown for Sample 1 after Run 1 (irradiation by Ne^+, dose 7×10^{11} cm^{-2}) and annealing to $T = 300$ K. σ(*T*) for the pristine sample is from Ref. [35].

Lastly we discuss the possibility of a metal-insulator transition in graphene with defects. Disorder-free graphene is expected to have a minimum conductivity of $4e^2/\pi h$ [92]. The introduction of intravalley scattering only (e.g. charged impurities) is expected to induce weak *anti*-localization, *increasing* the conductivity [92, 93] with decreasing temperature. However, intervalley scattering (which gives rise to the Raman *D* band) is expected to induce weak localization, and insulating behavior, i.e.

$\sigma \to 0$ as $T \to 0$, in graphene[92, 93]. From Figure 6.4a, we can see that σ_{min} in ion-irradiated samples can be reduced well below $4e^2/\pi h$, the minimum metallic value. Figure 6.5 shows the conductivity of the Ne^+ irradiated graphene sample as a function of temperature for three different gate voltages. The T-dependent conductivity of pristine graphene from Ref. [35] is also shown for comparison. The pristine graphene has metallic behavior, e.g., $d\sigma/dT < 0$. However, even a small amount of irradiation (that changes the room-temperature mobility $< 4\times$) drastically affects the low-temperature behavior. In stark contrast to graphene without irradiation, where σ_{min} is largely temperature independent from $T = 4\text{-}100$ K [44], our irradiated sample is insulating with diverging resistivity as $T \to 0$. More work is needed to understand the exact nature of the insulating state in ion-irradiated graphene, but the data are consistent with the expectation that intervalley scattering produces localization [92].

In conclusion, we have measured charge transport in graphene with defects induced by ion irradiation in ultra high vacuum. Defects cause significant intervalley scattering, as seen in a prominent Raman *D* band. Defects give rise to a constant mobility, with a magnitude ~$4\times$ lower than for similar concentration of potassium ions on graphene, and consistent with scattering by mid-gap states. In contrast to charge impurity disorder, lattice defects reduce the minimum conductivity dramatically, and produce an insulating temperature dependence of the conductivity.

Chapter 7: Phonon scattering and performance limits of graphene on SiO_2 [5]

The linear dispersion relation in graphene [25] gives rise to a surprising prediction: the resistivity due to isotropic scatterers, such as white-noise disorder[42] or phonons[63, 70, 71, 84, 104], is independent of carrier density, n. Here we show that electron-acoustic phonon scattering[63, 70, 71] is indeed independent of n, and contributes only 30 Ω to graphene's room temperature (RT) resistivity. At a technologically-relevant carrier density of 10^{12} cm^{-2}, we infer a mean free path for electron-acoustic phonon scattering of >2 microns, and an *intrinsic* mobility limit of 2×10^5 cm^2/Vs. If realized, this mobility would exceed that of InSb, the inorganic semiconductor with the highest known mobility (~7.7×10^4 cm^2/Vs [105]) and that of semiconducting carbon nanotubes (~1×10^5 cm^2/Vs [106]). A strongly temperature-dependent resistivity contribution is observed above ~200 K [104]; its magnitude, temperature dependence, and carrier density dependence are consistent with *extrinsic* scattering by surface phonons at the SiO_2 substrate[73, 75], and limit the RT mobility to ~4×10^4 cm^2/Vs, pointing out the importance of substrate choice for graphene devices[37].

[5] This chapter was adapted from: J.-H. Chen, C. Jang, S. Xiao, M. Ishigami, and M. S. Fuhrer, Nature Nanotechnology **3**, 206 (2008)

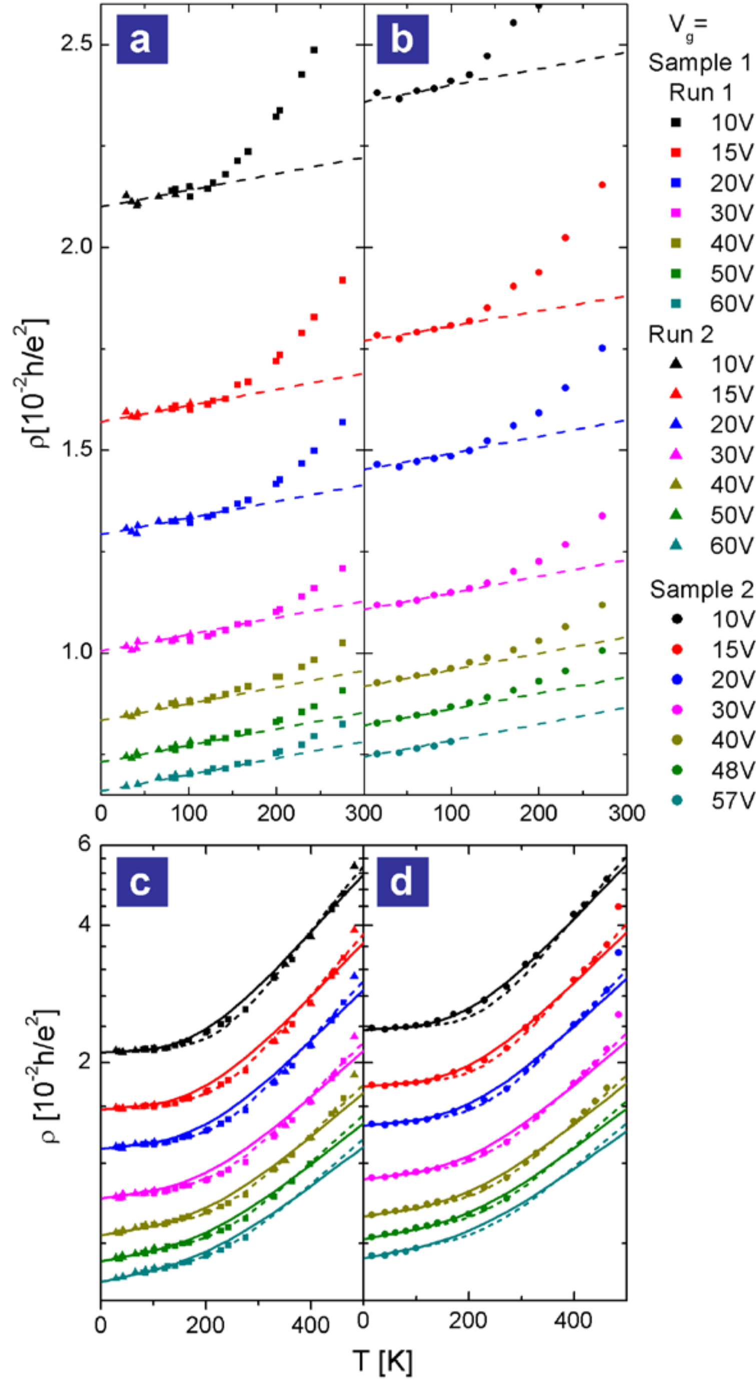

Figure 7.1 Temperature-dependent resistivity of graphene on SiO_2. a,b, Resistivity of two graphene samples (Sample 1, left panel; Sample 2, right panel) as a function of temperature for gate voltages from 10 to 60 V. Short-dashed lines are fits to the linear *T*-dependence (equation (7.1)). c,d, Same data as in a,b on a logarithmic scale. The solid lines are fits to equation (7.2a) (acoustic phonon scattering in graphene plus optical phonon scattering due to the SiO_2 substrate) and the short-dashed lines are fits to equation (7.2b) (the same acoustic phonon scattering term plus a single Bose-Einstein term).

The nature of electron-phonon scattering in graphene has been determined by measuring the four-probe resistivity $\rho(V_g,T)$ of graphene field-effect devices on SiO_2/Si [34, 45] vs. temperature T from 16 K – 485 K, and gate voltage V_g applied to the Si substrate (see Methods). Measurements are performed in ultra-high vacuum (UHV) on cleaned samples to minimize temperature-dependent effects due to molecular adsorption/desorption[34, 87].

The dependence of resistivity on carrier density is investigated by using the gate voltage to tune the carrier density $n = c_g V_g/e$, where $c_g = 1.15 \times 10^{-8}$ F/cm^2 is the gate capacitance, and e the elementary charge. Figure 7.1a and 7.1b show $\rho(V_g,T)$ for two samples at seven different gate voltages plotted on a linear scale. The $\rho(V_g,T)$ curves are linear in temperature at low T with a slope of $(4.0 \pm 0.5) \times 10^{-6}$ h/e^2K as indicated by the short-dashed lines. The slope is independent of carrier density, and is the same for both samples.

Acoustic phonon scattering is expected[63, 70-72] to give rise to a linear resistivity independent of carrier density

$$\rho(V_g,T) = \rho_0(V_g) + \rho_A(T);\;\; \rho_A(T) = \left(\frac{h}{e^2}\right)\frac{\pi^2 D_A^2 k_B T}{2h^2 \rho_s v_s^2 v_F{}^2}, \tag{7.1}$$

where $\rho_0(V_g)$ is the residual resistivity at low temperature, $\rho_A(T)$ is the resistivity due to acoustic phonon scattering, k_B is the Boltzmann constant, $\rho_s = 7.6 \times 10^{-7}$ kg/m^2 is the 2D mass density of graphene, $v_F = 10^6$ m/s is the Fermi velocity, v_s is the sound velocity, and D_A the acoustic deformation potential. For LA phonons, $v_s = 2.1 \times 10^4$ m/s and our experimentally determined slope gives $D_A = 18 \pm 1$ eV, in good agreement with theoretical[71, 72, 107-109] and experimental[110, 111] expectations. At very low temperature $T << T_{BG} \approx (v_s/v_F)T_F$, where T_F is the Fermi temperature, a

crossover to $\rho_A(T) \propto T^4$ is expected[71]; $T_{BG} \approx (8\ \text{K})V_g^{1/2}$ where V_g is measured in V. However, numerical calculations[71] show that $\rho(T)$ is indistinguishable from linear for temperatures above ~20 K even for $V_g = 70$ V, consistent with our measurement. (This is analogous to the familiar result for metals, where the linear temperature-dependent resistivity persists down to temperatures a small fraction of the Debye temperature.)

In contrast to the low-T behavior, the resistivity at higher T is highly non-linear in T, and becomes significantly dependent on V_g, increasing for decreasing V_g. Morozov, et al.[104] noted the non-linear dependence on T but were unable to separate the low-T LA phonon contribution from the high-T contribution, nor to identify the specific dependences on T or V_g for each contribution. The strong (activated) temperature dependence suggests scattering by a high-energy phonon mode or modes. We find that the data can be fitted by adding an extra term $\rho_B(V_g,T)$ representing the activated contribution to the resistivity:

$$\rho(V_g,T) = \rho_0(V_g) + \rho_A(T) + \rho_B(V_g,T); \quad \rho_B(V_g,T) = B_1 V_g^{-\alpha_1}\left(\frac{1}{e^{(59meV)/k_BT}-1} + \frac{6.5}{e^{(155meV)/k_BT}-1}\right), \quad (7.2a)$$

or

$$\rho(V_g,T) = \rho_0(V_g) + \rho_A(T) + \rho_B(V_g,T); \quad \rho_B(V_g,T) = B_2 V_g^{-\alpha_2}\left(\frac{1}{e^{E_0/k_BT}-1}\right), \quad (7.2b)$$

For equation (7.2a), the particular form of the expression in parenthesis in $\rho_B(V_g,T)$ is chosen to match surface phonons in SiO_2 [74, 75]; however, a single Bose-Einstein (BE) distribution as shown in equation (7.2b) can also give a reasonable fit. Figures 7.1c and 7.1d show a global fit to equation (7.2a) (solid lines) and to equation (7.2b)

(short-dashed lines) to the data for two samples. In addition to the low-temperature resistivity ρ_0, and linear term determined above, only two additional global parameters in equation (7.2a) (B_1 = 0.607 $(h/e^2)V^{\alpha_1}$ and α_1 = 1.04) and three global parameters in equation (7.2b) (B_2 = 3.26 $(h/e^2)V^{\alpha_2}$, α_2 = 1.02, and E_0 = 104 meV) are used to fit the seven curves each for two devices.

We now discuss the possible origins of the activated resistivity term $\rho_B(V_g,T)$. Scattering in graphene requires a phonon wavevector $q \approx 0$ (intravalley scattering) or $q \approx$ K (intervalley scattering). The next lowest-energy modes after the $q \approx 0$ acoustic modes are the zone boundary ZA phonon (q = K) at $\hbar\omega \approx 70$ meV and the optical ZO mode (q = 0) at $\hbar\omega \approx 110$ meV[112]. The optical ZO mode is consistent with the observed temperature dependence as per the fit to equation (7.2b), however both modes are out-of-plane vibrations, which are not expected to couple strongly to the electrons[107-110]; for example scattering by these modes is not observed in carbon nanotubes, while scattering by the longitudinal zone-boundary phonon with $\hbar\omega \approx 160$ meV is extremely strong[113] (but our data are poorly fit to a BE distribution with $\hbar\omega \approx 160$ meV). The strong carrier density dependence $\rho_B(V_g,T) \propto V_g^{-1.04}$ is also inconsistent with graphene optical phonon scattering, which should depend very weakly on carrier density[71]. Breaking of the inversion symmetry of the graphene sheet by the substrate induces an additional perturbation potential for the out-of-plane phonon modes, but reasonable estimates of the size of this perturbation are too small to account for the observed $\rho_B(V_g,T)$. Thus we reject optical phonon modes of graphene as the source of $\rho_B(V_g,T)$.

Another possible origin of $\rho_B(V_g,T)$ is remote interfacial phonon (RIP) scattering[73] by the polar optical phonons of the SiO_2 substrate. This has been recently discussed theoretically in the context of graphene by Fratini and Guinea[75]. The two strongest surface optical phonon modes in SiO_2 are calculated to have $\hbar\omega \approx$ 59 meV and 155 meV, with a ratio of coupling to the electrons of 1:6.5 [74, 75]; we used these parameters as inputs to equation (7.2a) above, and the fit shows that they reasonably describe the temperature dependence of $\rho_B(V_g,T)$ (see Figures 7.1c,d). The magnitude of the RIP scattering resistivity predicted by Fratini and Guinea[75] is on order a few $10^{-3}\, h/e^2$ at 300 K, also in agreement with the observed magnitude. RIP results in a long-ranged potential, which gives rise to a density-dependent resistivity in graphene, similar to charged impurity scattering. Specifically, in the simplest case, the electron-phonon matrix $|H_{kk'}|^2$ element is proportional to q^{-1} where q is the scattering wavevector, and the resistivity is proportional to $k_F^{-1} \propto V_g^{-1/2}$. However, finite-$q$ corrections to $|H_{kk'}|^2$ lead to a stronger dependence of $\rho_B(V_g,T)$ on V_g [75], so the observed $\rho_B(V_g,T) \propto V_g^{-1.04}$ is also reasonable. RIP scattering by the polar optical phonons of the SiO_2 substrate therefore naturally explains the magnitude, temperature dependence, and charge carrier density dependence of $\rho_B(V_g,T)$, hence we consider RIP scattering to be the most likely origin of $\rho_B(V_g,T)$.

We note that although our measurements were performed on clean samples in UHV, the *temperature-dependent component* of the resistivity is consistent in magnitude with earlier, more limited studies of $\rho(V_g, T)$ in graphene[84, 104], where resist residue and adsorbed atmospheric species were not rigorously controlled (though the residual resistivity shows larger variations). This supports our conclusion

that the observed temperature-dependent resistivity is intrinsic to the graphene/SiO_2 system. We also note that graphene on SiC should have significantly reduced RIP scattering[75]; this is supported by an estimate of the electron-phonon scattering time for graphene on SiC at $T = 300$ K of $\sim 4 \times 10^{-12}$ s at $n = 3.4 \times 10^{12}$ cm^{-2}[24], compared to $\sim 0.6 \times 10^{-12}$ s at the same carrier density in our samples.

Finally, we note that the published version of Ref. [8] points out that graphene on poly(methyl methacrylate) (PMMA) (studied in Ref. [8]) shows a similar rise in resistivity (at least up to room temperature) as graphene on SiO_2, and takes this as evidence that RIP scattering is unlikely to be the source of the upturn. It is difficult to make any quantitative comparison of our data with those of Ref. [8], since their model and analysis specifically exclude any carrier density dependence of the resistivity upturn, contrary to the experimental observation. However, it is quite plausible that PMMA shows similar RIP scattering to SiO_2 because (1) contrary to the claim of Ref. [8], PMMA and SiO_2 have almost identical low- and high-frequency dielectric constants, and (2) PMMA shows a number of infrared-active phonon modes in the range 60-120 meV (as well as higher energies; see e.g. the Spectral Database for Organic Compounds, AIST, Japan) which could give rise to a resistivity upturn at room-temperature.

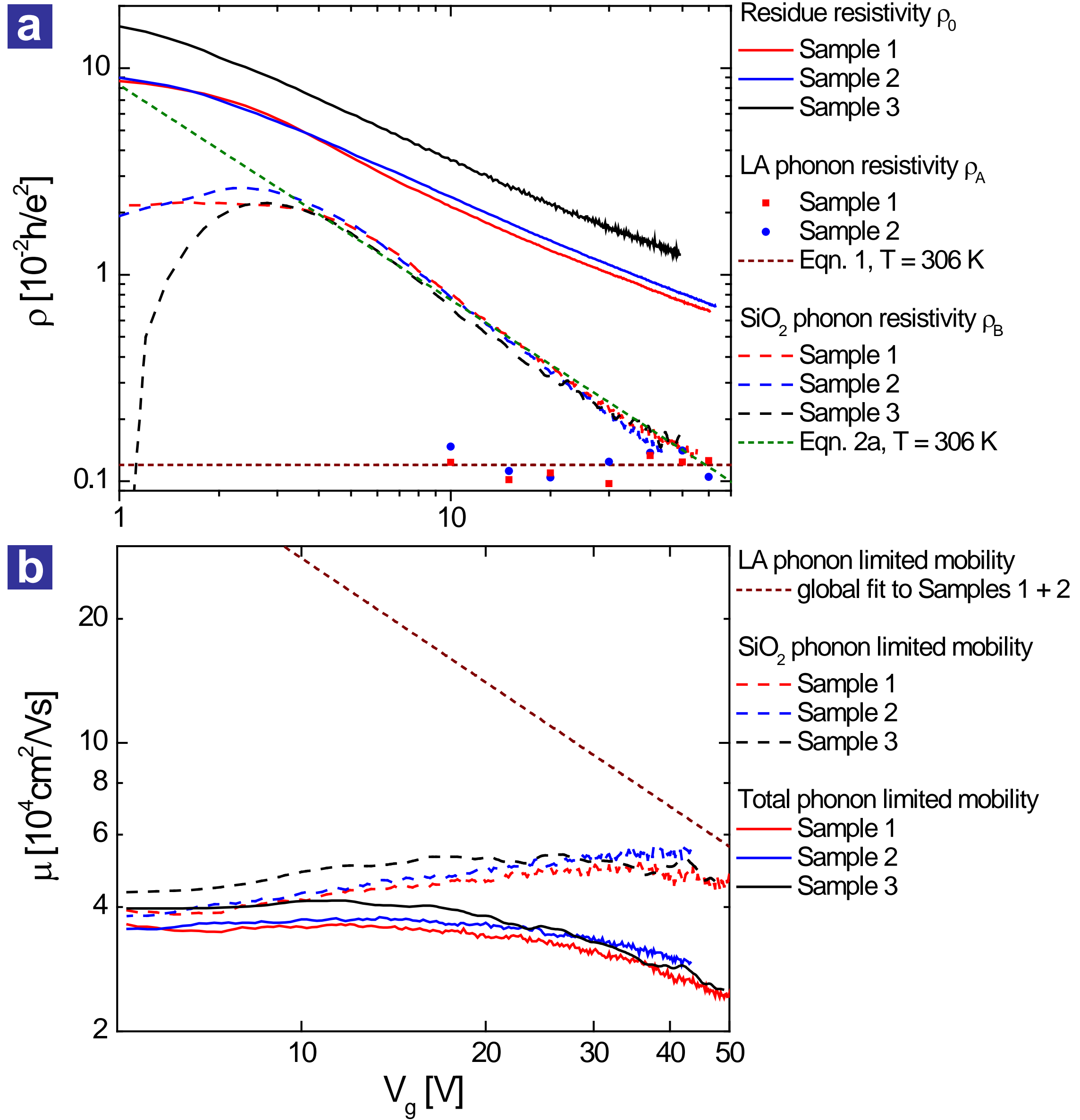

Figure 7.2 Room temperature performance limits of graphene on SiO_2. a, Residual resistivity ρ_0, acoustic phonon resistivity ρ_A, and SiO_2 remote interfacial phonon resistivity ρ_B as a function of gate voltage near room temperature for three samples. b, Gate-voltage-dependent mobility limits at room temperature corresponding to scattering by acoustic phonons (short-dashed line), SiO_2 surface phonons (long-dashed lines), and both phonon contributions (solid lines).

The contributions of the acoustic phonons and remote interfacial phonons can be used to determine the room-temperature intrinsic limits to the resistivity and mobility in graphene, and extrinsic limits for graphene on SiO_2. Figure 7.2a shows

the gate voltage dependence of the three components of the resistivity (ρ_0, ρ_A and ρ_B) corresponding to scattering by impurities, graphene LA phonons, and RIP scattering by SiO_2 phonons, respectively, near room temperature (RT) for three different graphene samples (T = 330K, 308K & 306K for Samples 1, 2 & 3, respectively; Sample 1 and Sample 2 are the same samples shown in Figure 7.1, and Sample 3 is a lower mobility sample for which we have limited temperature dependence data.) The residual impurity resistivity $\rho_0(V_g)$ (solid lines) is estimated, with an error not greater than 1.5%, by taking $\rho(V_g, T)$ at low temperature (T = 29K, 16K & 20K for Sample 1, 2 & 3, respectively). The graphene LA phonon resistivity $\rho_A(306\ \mathrm{K}) = 1.2 \times 10^{-3}\ h/e^2$ (dark red dashed line) is obtained from the global fit to equation (7.1) for Samples 1 and 2; the solid symbols are obtained from individual fits to $\rho(T)$ at various V_g. The RIP scattering resistivity $\rho_B(V_g,\ T \approx \mathrm{RT})$ (long-dashed lines) is obtained by subtracting $\rho_A(T)$ and $\rho_0(V_g)$ from $\rho(V_g, T)$ for each sample. Though $\rho_0(V_g)$ varies by a factor of 1.7X among the three samples, the temperature-dependent resistivities $\rho_B(V_g, T)$ are nearly equal except very close to the MCP (see Appendix A5); this verifies that the temperature-dependent resistivity terms ρ_A and ρ_B arise from phonon scattering which is disorder-independent. The power-law behavior of the activated contribution $\rho_B(V_g, 306\ \mathrm{K}) \propto V_g^{-1.04}$ can also clearly be seen.

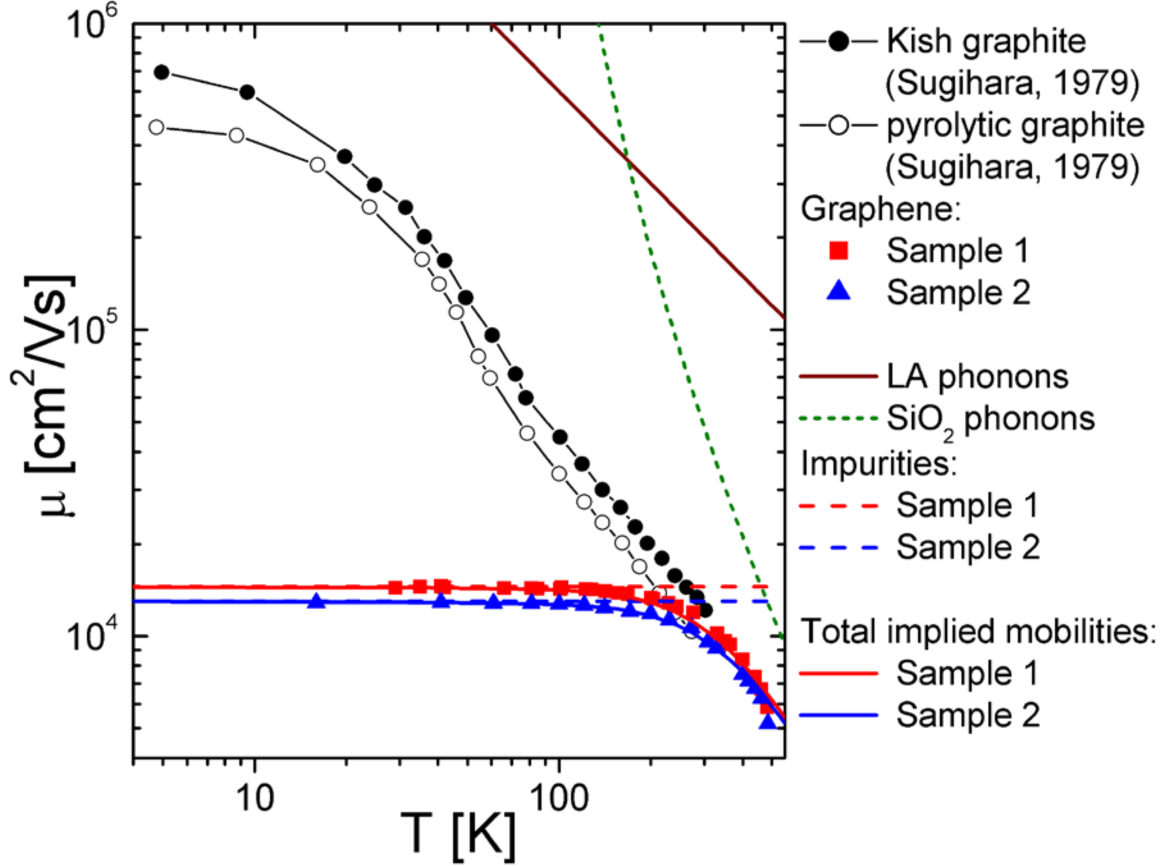

Figure 7.3 Temperature dependence of the mobility in graphene and graphite. The temperature-dependent mobilities of graphene Sample 1 (red squares) and Sample 2 (blue triangles) at V_g = 14 V (n = 10^{12}cm^{-2}) are compared with Kish graphite (solid black circles) and pyrolytic graphite (open black circles)[32]. The mobility limits in graphene determined in this work for scattering by LA phonons (dark red solid line), remote interfacial phonon scattering (dark green short-dashed line), and impurity scattering (red and blue dashed lines) are shown. Red and blue solid lines show the expected net mobility for each sample, according to Matthiessen's rule.

Figure 7.2b shows the corresponding room temperature mobility $\mu = 1/ne\rho = 1/c_g V_g \rho$ calculated for each phonon resistivity contribution in Figure 7.2a as a function of gate voltage. If the properties of graphene were limited by the intrinsic LA phonon scattering as the dominant intrinsic source of resistivity, the room-temperature intrinsic resistivity of graphene would be 30 Ω, independent of carrier density, and the mobility would diverge at low carrier density as n^{-1}. At a

technologically-relevant carrier density n = 10^{12} cm^{-2} (V_g = 14 V), the intrinsic mobility would then be 2×10^5 cm^2/Vs, higher than any known semiconductor. If the only extrinsic limit to the mobility of graphene on SiO_2 were due to RIP scattering, graphene on SiO_2 would still have a room temperature mobility of 4×10^4 cm^2/Vs, which compares favorably to the best InAs and InSb FETs[114]. The dominance of RIP scattering over LA phonon scattering at room temperature poses an interesting tradeoff; high-κ dielectrics may be used to reduce the scattering contribution from defects (i.e. ρ_0) due to increased screening of the impurity potential, but will *increase* scattering due to RIP[75].

Figure 7.3 shows the temperature dependence of the mobility of Sample 1 and Sample 2 at $n = 10^{12}$ cm^{-2} (V_g = 14 V), as well as the limits due to scattering by LA phonons, polar optical phonons of the SiO_2 substrate, and impurities. As shown in Figure 7.3, even for the cleanest graphene devices fabricated to date, impurity scattering is the still the dominant factor limiting the mobility for $T < 400$ K. For comparison, the temperature-dependent mobility in Kish graphite and pyrolytic graphite from ref. [32] are also shown; these are the two materials commonly used as sources for exfoliated graphene on SiO_2. The significantly higher mobility at low temperature in Kish and pyrolytic graphites compared to graphene is a strong indication that the impurity scattering in graphene on SiO_2 is not due to point defects present in the parent material, but rather is likely caused by charged impurities in the SiO_2 substrate[34, 53]. It is important to note that the closeness of the room-temperature mobility values for graphene and bulk graphite is a coincidence, and

removing impurity scattering in graphene will greatly increase not only the low temperature mobility, but the room temperature mobility as well.

Our data give a complete picture of the current limitations and future promise of graphene as an electronic material. Currently, mobility of graphene on SiO_2 at low and room temperature is limited by impurity scattering, likely due to charged impurities in the SiO_2 substrate[34, 53]. If charged impurity scattering can be reduced, the room-temperature mobility, limited by extrinsic RIP scattering due to SiO_2 phonons, could be improved to 4×10^4 cm^2/Vs, comparable to the best field-effect transistors[114]. With proper choice of substrate[24, 37], or by suspending graphene, the intrinsic limit of mobility of 2×10^5 cm^2/Vs at room temperature could be realized. This would dramatically enhance the application of graphene field-effect devices to chemical sensing, high-speed analog electronics, and spintronics. In addition, ballistic transport over micron lengths would open the possibility of new electronic devices based on quantum transport operating at room temperature.

Methods

Experiments were carried out at pressure lower than 2×10^{-9} torr at 490 K and 1×10^{-10} torr below 300 K. The device temperature was tuned from 485 K to room temperature using a heater installed on the cold finger, and controlled liquid helium flow was used to tune the device temperature from 290 K to 16 K, with resistivity vs. gate voltage $\rho(V_g)$ curves taken at various temperature points. Warming experiments were also performed, where the device temperature was raised from 16 K to 243 K by controlling the helium flow. Heater operation was avoided at low temperature to

prevent outgassing of the coldfinger. Transport properties of the samples between cooling and warming are very reproducible, showing no detectable effect of residual gas absorbed on the samples during the experiment; the exception is that small differences in cooling and warming data are occasionally observed very near the minimum conductivity point (MCP); see Appendix A5 for more details.

Resistivity measurements were performed using a standard four-probe technique and error in determining the aspect ratio (and hence the absolute magnitude of the resistivity) is estimated to be 10% [34]. Resistivity vs. gate voltage $\sigma(V_g)$ curves are shifted by a constant threshold voltage V_{th} in order to define $V_g = 0$ as the MCP. V_{th} is small ($V_{th} = 0$ V for Sample 1 and -3 V for Sample 2) and does not change with temperature for cleaned samples that are outgassed sufficiently in UHV. Sample 3 was prepared the same way as Sample 1 and Sample 2, and then multiple potassium deposition and removal cycles were carried out in UHV resulting in an increased density of immobile impurities and lowered mobility[34]. $V_{th} = -8.2$ V for Sample 3.

Chapter 8: Printed graphene circuits[6]

A single layer of graphite, graphene [24, 45], is a truly 2-dimensional semi-metallic material composed of only one atomic layer of carbon atoms. Graphene's peculiar band structure suppresses carrier backscattering, leading to extremely high carrier mobility [24]. Narrow graphene ribbons are predicted to have a semiconducting energy gap tunable by width [115], indicating a path to device fabrication. In addition, because graphene is only one atom in thickness, transport properties are expected to be sensitively influenced by atomic scale defects, adsorbates [87, 88], local electronic environment, and mechanical deformations; consequently, graphene is a promising sensor material. To date, graphene has been obtained by only two methods: mechanical exfoliation of graphite on SiO_2/Si [45] or thermal graphitization of a silicon carbide (SiC) surface [24]. In each case, the substrate strongly influences the graphene properties; charge defects in SiO_2 are thought to limit the mobility, and strong interaction with SiC introduces a large charge density. Furthermore, the substrate can limit the graphene device possibilities; gating of devices on SiC is difficult, and on SiO_2/Si the presence of a conducting backplane (also used as the gate) precludes high-frequency device operation. In this paper, we report the transfer of graphene from one substrate to another to realize flexible, transparent graphene devices with high field effect mobility. This represents the ultimate extension of the printing technology to a single atomic layer.

[6] This chapter was adapted from: J. -H. Chen, M. Ishigami, C. Jang, D. R. Hines, M. S. Fuhrer, and E. D. Williams, Advanced Materials **19**, 3623 (2007)

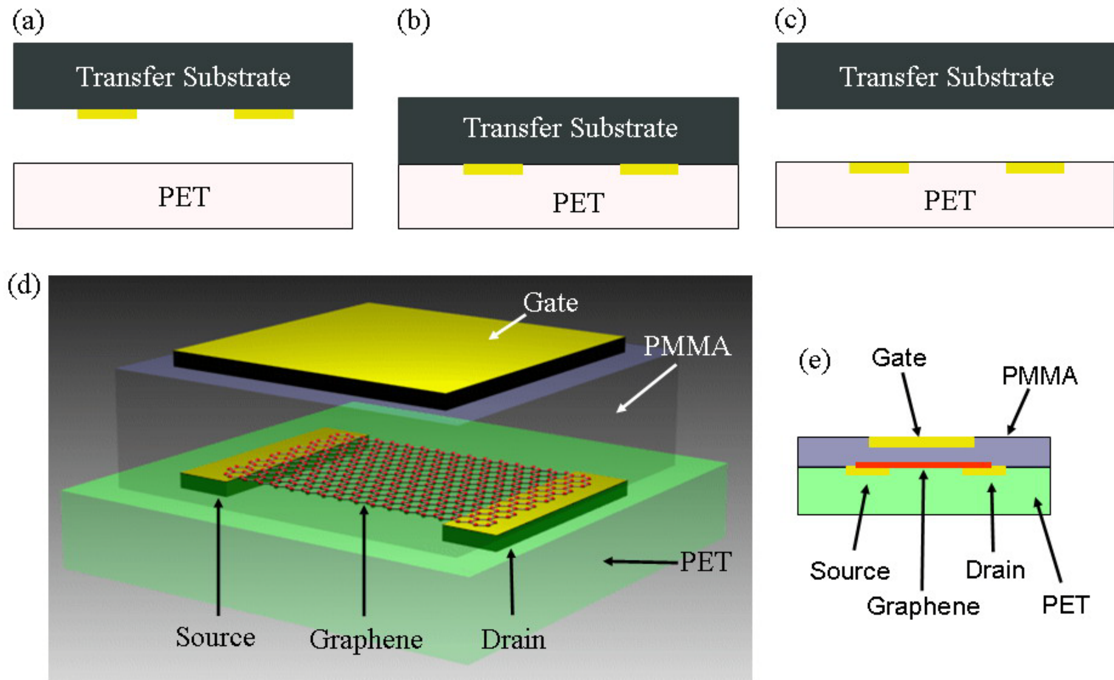

Figure 8.1 (a)-(c) Printing procedure used to print a feature layer. (a) The desired features, e.g. two gold electrodes, are predefined on the transfer substrate. (b) The transfer substrate is brought into contact with the plastic substrate at an elevated temperature and high pressure. Temperature and pressure are optimized to ensure successful transfers for each material process. (c) The transfer substrate is removed from the plastic substrate, leaving the features embedded in the plastic substrate. The process may be repeated to assemble additional components. (d) The 3D schematic and (e) the cross sectional view of the completed graphene device, not drawn to scale.

We employ the transfer printing method [78, 79] to transfer graphene between SiO_2/Si and plastic substrates, as well as to assemble the gate dielectric, and source, drain, and gate electrodes, forming a complete graphene field-effect transistor with local gate on a flexible, transparent substrate. Transfer printing enables device component fabrication and assembly to be performed separately, and has found wide application in printed circuits and flexible electronics research [78, 116-118]. By properly tuning the adhesion of the printed material to the original and target

substrate [78], our technique can in principle enable the transfer of graphene to *any* substrate, thus greatly expanding the possible applications of this material.

Figure 8.1a-c depicts the basic process required to print a patterned layer of material from one substrate (the transfer substrate) over to a second substrate (a PET plastic substrate). The devices require three process steps performed sequentially to assemble (1) source-drain electrodes, (2) graphene, and (3) gate electrode/dielectric. First, photolithography is used to prepare 30 nm thick Au source and drain electrodes on a silicon wafer with an oxidized surface (SiO_2/Si). The electrodes are then transferred onto the PET substrate as described elsewhere [78, 79]. Then, single- and few-layer graphene is obtained from Kish graphite by mechanical exfoliation [45] on 300nm thermally-grown silicon dioxide on silicon substrates, and its thickness and morphology characterized by atomic force microscopy. Mechanical exfoliation yields atomically-clean graphene sheets [91] and our AFM images also indicate that the graphene sheet is free of nanometer-scale contaminants. In addition, chemical contamination caused by exposure to photoresist and lift-off chemicals is avoided in this process. The desired graphene sheet is printed at 170 °C at 500 psi from the silicon dioxide substrate to the source-drain electrode assembly on PET. Under these conditions, the PET substrate is above its glass transition temperature, and can conform to the transfer substrate morphology [78]. Finally, the gate assembly consisting of a photolithographically patterned 100 nm Au gate electrode and a 600 nm thick poly(methyl metacrylate) (PMMA) gate dielectric is prepared on SiO_2/Si and transfer printed onto the device substrate at 175 °C at 500 psi. Each subsequent layer is aligned optically to the pre-existing features. Figure 8.1d shows the

schematic of a completed device. An advantage of this method is that it exposes graphene to no chemicals used in conventional lithography processes, by which most of the graphene devices on silicon dioxide are fabricated. Lithography processes have been found to leave residue on the device [38] and might negatively influence transport properties.

The printing process is successful in transferring graphene materials, ranging from monolayer sheets to bulk graphite, from the silicon dioxide substrate to PET and Au. Figure 8.2a shows an optical microscopy image of a graphite film with thicknesses from monolayer to multilayer on a silicon dioxide substrate. Figure 8.2b shows the graphene material printed to the source-drain electrodes on PET (the image is reversed to aid comparison to Figure 8.2a). By comparison of Figures 8.2a and 8.2b, it is clear that the conduction from source to drain electrode takes place through the portions labeled “monolayer” and “bilayer” in Figure 8.2a, in series. (As a visual aid, red dotted lines have been added to Figure 8.2a as an indicator of the location of the edges of the source-drain electrodes (separated by 6 μm) with respect to the graphene before printing.) The thickness of the monolayer portion is confirmed by atomic force microscopy (AFM) before transfer printing as shown in Figures 8.2c-8.2d. Figure 8.2c is an AFM micrograph acquired in the boxed region indicated in Figure 8.2a, which shows the functioning monolayer portion with another monolayer lying across it. The red box in Figure 8.2c shows an area where the top layer steps down from the functioning layer to the substrate, and the step height here is the thickness of the functioning layer. Figure 8.2d shows the height histogram of the area inside the red box in Figure 8.2c. Fitting the histogram by two Gaussian peaks gives

an estimate of the thickness of the monolayer portion to be 3.95±0.09Å, which confirms that the functioning material is single layer graphene [38].

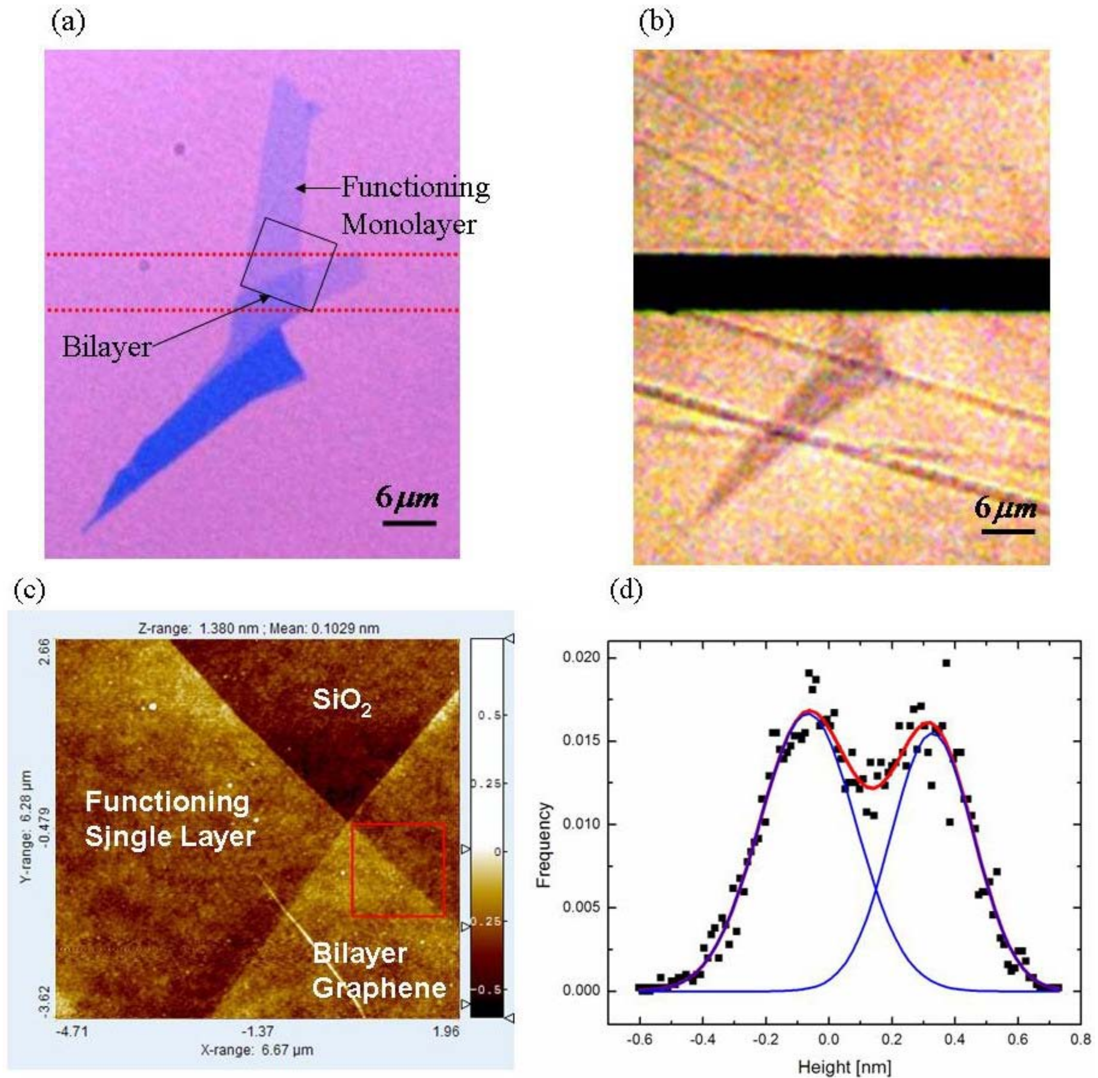

Figure 8.2 (a) Optical microscopy image of a mixed monolayer and multilayer graphene material on silicon dioxide substrate. (b) Optical microscopy image of the same graphene sample transfer printed onto the source/drain electrode assembly (dark area is PET, yellow areas are Au electrodes). The Au source-drain electrodes are bridged by graphene composed of a single-layer portion and a bilayer portion. Note: (b) is left-right reversed to aid comparison to (a). (c) Atomic force micrograph of the selected area (shown by box in (a)) of sample prior to transfer print, used to determine the number of graphene layers. (d) Histogram of the selected area (area inside the red box in (c)) is fitted by two Gaussian peaks. The height difference between the two peaks is 3.95±0.09Å, which indicates that the functioning material is single layer graphene.

After transfer no graphene is observed in optical images on the silicon dioxide substrate; this indicates that graphene adheres more strongly to PET and Au than to the original silicon dioxide substrate, and the interlayer coupling strength of graphite is stronger than its adhesion to the silicon dioxide surface. The presence of the Au source-drain electrodes is not necessary for transfer of graphene materials from silicon dioxide substrates to PET; graphene materials can be transferred to bare PET. Graphene materials are barely visible once transferred onto PET as seen in Figure 8.2b, and can only just be discerned on the source-drain electrodes. Graphene is nearly completely transparent at visible wavelengths.

Measurement of the transport properties is important to assess the usefulness of the transfer printing process. Figure 8.3a shows the room temperature conductivity [119] as a function of gate voltage $\sigma(V_g)$ of the "printed" device shown in Figure 8.2b. As seen in Figures 8.2a and 8.2b, this device consists of two portions (monolayer and bilayer) in series. As graphene sheets are semi-metals with linearly vanishing electronic densities of states at the charge-neutral point, the applied gate voltage modifies the conductivity. The slope of the linear portion of the transfer curve is used to calculate the field effect mobility, $\mu = \frac{1}{c_g}\frac{d\sigma}{dV_g}$, where c_g is the gate capacitance per unit area (4.4 nF/cm^2). This particular device shows a maximum field effect mobility of 1.0×10^4 cm^2/Vs for holes and 4×10^3 cm^2/Vs for electrons. Another device composed solely of a monolayer material showed similar field effect mobilities. These values are comparable to the best field effect mobilities measured for graphene devices on SiO_2 at room temperature, for example $2 \times 10^3 – 5 \times 10^3$ cm^2/Vs reported by Novoselov et al. [45], and $2 \times 10^3 – 1.5 \times 10^4$ cm^2/Vs reported by Tan et al. [31],

suggesting that the transfer method does not damage the graphene and no chemical bonding was established between graphene and plastic substrates.

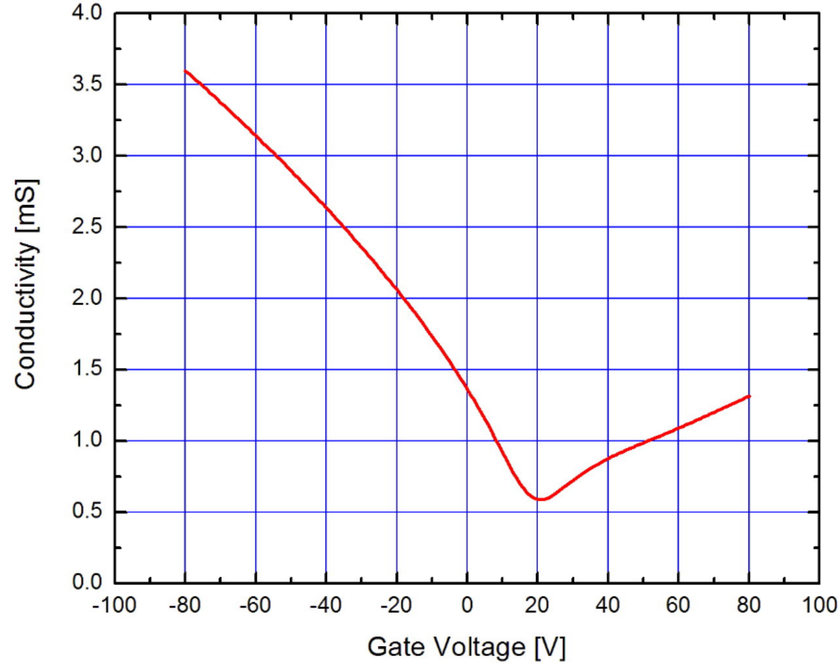

Figure 8.3 Conductivity as a function of gate voltage for the device in Figure 8.2b measured at 297 K. The minimum conductivity is about 0.6 mS or $\approx 8G_0$ at the Dirac neutral point $V_D = 21$V, where $G_0 = \frac{2e^2}{h}$ is the quantum of conductance. The capacitance of PMMA dielectric used is 4.4 nF/cm^2. 21 V applied across the PMMA dielectric induces the same amount of charge density as 8V across 300nm silicon dioxide dielectric. Source-drain bias of 10 mV was applied while acquiring the above data.

The minimum conductivity for the "printed" graphene device, shown in Figure 8.3 is approximately 0.6 mS $\approx 8\ G_0$, where $G_0 = \frac{2e^2}{h}$ is the quantum of conductance. The minimum conductivity reported for monolayer [44] and bilayer [120] graphene-based devices is often near $2G_0$ (but may be higher in clean samples [53]). The high value of the minimum conductivity for the printed devices indicates

that the contact resistance is small in the transfer-printed devices. Overall, the results show that transfer printing graphene can yield electronic devices equaling the performance of the conventional silicon dioxide-supported devices.

The Dirac neutral point of the printed device (see Figure 8.3) is about 21V (a second printed single layer graphene device showed the same shift), which corresponds to net positive charge density of 5.8 $x10^{11}$ cm^{-2}. One possible explanation is that this shift originates from excess positive trapped charge in the polymer substrate [121-124]. The same amount of charge density would be induced by applying 8V of gate voltage on 300nm silicon dioxide dielectric. A shift of this magnitude is not uncommon in graphene devices on silicon dioxide [25], but smaller values have been reported [47]. For comparison, the density of charge traps has been reported to be $2x10^{11}cm^{-2}$ in PET [122, 124], $5x10^{8}$ cm^{-2} in PMMA [121, 123], and $5x10^{11}$ cm^{-2} in thermally grown silicon dioxide [125]. If the Dirac point shift is predominately determined by trapped charge, these observations would suggest that the PET/PMMA sandwich creates an excess of positive trapped charge and a net charge density comparable to the best observed devices on SiO_2. Alternatively, other mechanisms such as a surface dipole moment, work-function difference between graphene and gate, or chemical doping may also be involved.

Finally, electronic [50, 53, 88] and structural [38] disorder imposed by the substrate, are expected to determine the graphene transport properties, including the mobility, minimum conductivity, and the shift of the Dirac point. The PET/PMMA sandwich substrates in the printed devices nominally [121-125] have net trap densities similar to silicon dioxide substrates. The RMS roughness of the substrate is

larger for the PET substrates (1.2 nm in a 5 μm × 5 μm area) than for the silicon dioxide substrates (0.25 nm in a 5 μm × 5 μm area). There are two anomalous features in the transport measurements. First, the minimum conductivity is unusually high at $8G_0$ even for the solely monolayer printed devices. This indicates that the reported universality [44] of the minimum conductivity at $2G_0$ is not correct, and the $2G_0$ value may be specific only to certain silicon dioxide-supported devices. In addition, the devices on the plastic substrates always have higher hole mobility (e.g., they do not have electron-hole symmetry). Such asymmetry has not been reported previously for graphene devices. The present transport theory [50, 52, 53, 81], which focuses on short range or long range scatterers to describe the transport properties, is incapable of explaining such a large asymmetry. The roughness of the PET substrate and the observed high mobility of the printed devices suggest either that the graphene morphology play little role in determining the transport properties, or that the graphene sheet does not closely conform to the underlying PET morphology. Further work correlating the transport characteristics with systematic variation of substrate charge density and roughness is needed to identify the mechanism behind the differences.

The transfer-printed devices represent the first realization of a local electrostatic gate on graphene-on-insulator. Local gating enables the reduction of gate-source capacitance, which is necessary for high-frequency device operation. Local gating can also be used to explore p-n junctions in graphene, which are predicted to have unusual properties [62, 126, 127], and may form the basis of new bipolar transistor devices [126]. In addition, graphene may represent the ultimate

transparent electrode; the resistivity of our graphene at high gate voltage is less than 300 Ω/square, while graphene on PET is so transparent as to be nearly undetectable in the optical microscope.

In conclusion, we have fabricated transparent electronic devices based on graphene materials with thickness down to a single atomic layer by the transfer printing method. The resulting printed graphene devices retain high field effect mobility and have low contact resistance. The results show that the transfer printing method is capable of high-quality transfer of graphene materials from silicon dioxide substrates, and the method thus will have wide applications in manipulating and delivering graphene materials to desired substrate and device geometries. Since the method is purely additive, it exposes graphene (or other functional materials) to no chemical preparation or lithographic steps, providing greater experimental control over device environment for reproducibility and for studies of fundamental transport mechanisms. Finally, the transport properties of the graphene devices on the PET substrate demonstrate the non-universality of minimum conductivity and the incompleteness of the current transport theory.

Chapter 9: Summary and future outlook

9.1 Summary

Graphene is a fascinating material because it is only one atom thick (thus consists of all surface atoms) and highly ordered. On the electronic side, charge carriers in graphene are chiral massless Dirac fermions that can travel thousands of interatomic distances without scattering [48], but environment does have dramatic effect on its charge transport properties [27, 33-36]. Our data give a complete picture of the current limitations and future promise of graphene as an electronic material. At the present state-of the art of materials preparation, the mobility of graphene on SiO_2 at low and room temperature is limited by charged impurity scattering, likely due to charged impurities in the SiO_2 substrate [34, 53], although the possibility that it may also be influenced by impurities deposited on graphene during the fabrication process cannot be ruled out. Atomic-scale defects, which are likely to be present in future commercial graphene products, possibly made from expitaxial graphene or wet exfoliated graphene, affect mobility at least 4 times more strongly than a similar concentration of charged impurities [33]. Above 200K, polar optical phonons from the SiO_2 substrate become an important limiting factor to the overall mobility[35]. Corrugations in graphene on SiO_2 should produce a very small limiting resistivity that is only weakly dependent of density [36, 38, 65], and together with weak short-ranged scatterers [39], have minor contribution to device resistivity.

Increasing the low-temperature mobility of graphene can be accomplished by either (1) reducing the number of charged impurities, or (2) reducing their effect. The

former has been demonstrated by removing the substrate altogether, followed by high current annealing of graphene to produce samples with mobility on order 200,000 cm^2/Vs at low temperature [27]. Reducing the effect of charged impurities can be accomplished by increasing the dielectric constant of the graphene environment; as shown in Appendix A3, a modest increase of the average dielectric constant from 2.45 to 3.55 resulted in an increase of mobility of over 30% [39].

If charged impurity scattering can be reduced, the room-temperature mobility, limited by the extrinsic remote interfacial phonon scattering due to SiO_2 phonons could be improved to 4×10^4 cm^2/Vs, comparable to the best field-effect transistors [114]. Reduction of charged impurity scattering by use of a high-κ dielectric substrate or overlayer may also increase remote interfacial phonon scattering at room temperature, canceling any gains in mobility [128], though some substrates, such as SiC with very high frequency optical modes, may avoid this problem [75, 128]. With proper choice of substrate [24, 37], or by suspending graphene [27], the intrinsic limit of mobility of 2×10^5 cm^2/Vs at room temperature could be realized [35]. This would dramatically enhance the application of graphene field-effect devices to chemical sensing, high-speed analog electronics, and spintronics. In addition, ballistic transport over micron lengths would open the possibility of new electronic devices based on quantum transport operating at room temperature.

Transfer-printing is shown [37] to be an invaluable technique in manipulating graphene. It is capable of high quality transfer of graphene to flexible substrates [37] that could have substantially smaller density of charged impurities; in principle one could transfer graphene to an inorganic target substrate which has very high

frequency of optical phonon modes in order to reduce the remote interfacial scattering; novel device structure such as vertical integration [129], locally gated devices, suspended graphene devices could also be made by transfer-printing.

In addition, since the transfer printing method is purely additive, it exposes graphene to no chemical preparation or lithographic steps, providing greater experimental control over device environment for reproducibility and preservation of high carrier mobility in the graphene device.

9.2 Future outlook

The research progress in graphene has been very rapid since its first isolation, but there are many open questions remain to be solved for scientific understanding and technological applications of graphene. In this section, I will briefly discuss three potential high impact research directions to give readers a flavor of the conquered frontier of this attractive electronic material.

Opening a bandgap in graphene

One of the important directions in graphene research is to open a bandgap in the (originally) zero-gap semiconductor, which could extend the current application of graphene from high speed analog devices to high speed digital devices.

A bandgap is in principle possible to be generated by quantum confinement in one of the two dimensions of the material, e.g. making a graphene nanoribbon [130-132]. It is experimentally shown that graphene nanoribbon, from e-beam lithographic patterning [133, 134] or from sonication of a graphite liquid suspension [135, 136],

indeed showed a transport gap (at which the electrical conduction is effectively turned off). However, it is found that the mobility gap observed experimentally might be due to Coulomb blockade instead of a real bandgap [137]. An atomically smooth edge is needed to produce a spatially uniformed bandgap, which is beyond the capability of current device patterning technology, and new technology has to be developed to meet the challenge.

Another way to open a bandgap is to break the A-B sublattice symmetry [138, 139], which is in principle possible by the adsorption of a certain type of molecule on the graphene surface [140]. The type of molecule, the condition of the adsorption and the binding energy between the adsorbed layer and graphene (which will determine the strength of the perturbation and thus the bandgap) remain open questions.

Many other methods are proposed to open a bandgap in graphene systems. For example, it is argued that electric field normal to the basel plane of a Bernel stacking bilayer graphene (A-B stacking of two graphene layers) device could introduced enough perturbation to open a bandgap [119, 141]. Experimentally, solid evidence of a sizable bandgap is still lacking [142].

The mass production of graphene flakes

Another important technological question is the mass production of high quality graphene. Mechanical exfoliation of graphite provides the highest quality graphene that is of great scientific value; however, it is not a scalable technique, and the scientific and technical community will have to find a low cost way to mass produce graphene. As mentioned in Chapter 1, the expitaxial methods are able to

mass produce graphene, but it suffered from strong bonding of graphene to the substrate [19-21], or multilayer growth [23, 24]. "Wet exfoliation" of graphite is a promising approach because it is low cost and easily scalable [135, 143-145]. The challenge remains for the "wet exfoliation" approach to produce, with higher yield, high quality graphene and the deposition of which on desired substrates.

Graphene as a spintronic material

Important potential applications of graphene involves the spin degree of freedom of the conduction electrons [146-148]. The long electronic mean free path [149] and small spin-orbit coupling [150] should lead to very long spin scattering time [151]. It is experimentally demonstrated that spin-polarized current in graphene could travel hundreds of nanometers without losing the spin information [152, 153]. What remains an open question is how to efficiently inject spin into graphene [154], or how the electrons in graphene interact with a localized spin [155]. A controlled study of the interaction of magnetic atoms with graphene will provide important insight into this issue.

A1: Atomic structure of graphene on SiO_2[7]

Abstract

We employ scanning probe microscopy to reveal atomic structures and nanoscale morphology of graphene-based electronic devices (i.e. a graphene sheet supported by an insulating silicon dioxide substrate) for the first time. Atomic resolution STM images reveal the presence of a strong spatially dependent perturbation, which breaks the hexagonal lattice symmetry of the graphitic lattice. Structural corrugations of the graphene sheet partially conform to the underlying silicon oxide substrate. These effects are obscured or modified on graphene devices processed with normal lithographic methods, as they are covered with a layer of photoresist residue. We enable our experiments by a novel cleaning process to produce atomically-clean graphene sheets.

[7]This chapter was adapted from: M. Ishigami, J.-H. Chen, W.G. Cullen, M.S. Fuhrer and E.D. Williams, Nano Lett. **7**, 1643 (2007)

Graphene[24, 45], a single layer of graphite, is an unique material with exotic electronic properties[24, 25, 45, 47, 87, 156, 157]. A hexagonal two-dimensional network of carbon atoms composes graphene; it is exactly one atom in thickness and every carbon atom is a surface atom. Therefore, substrate-induced structural distortion[158], adsorbates[87], local charge disorder[52], atomic structure at the edges[157, 159], and even atomic scale defects [160] could be very important for transport properties of graphene. Specifically, lowered carrier mobility[158] and suppression of weak localization[158] in graphene-based devices have been attributed to corrugation of the graphene. Consequently, understanding the atomic and nanoscale structures of graphene in the configuration in which it is measured is crucial to explaining the observed transport properties.

Experimentally, controlling the environment of graphene in a device configuration is difficult. Graphene on the common gate dielectric, SiO_2, is subject to the effects of trapped oxide charges[161], which are highly dependent on sample preparation. In addition, graphene devices are typically fabricated using electron beam lithography, exposing the graphene to photoresist that can leave behind contaminants which, like any chemical adsorbate, may modify electronic transport properties[88], may play a large role in reported graphene response to gas exposure[87], etc.. For instance, a freestanding graphene sheet has been reported to have intrinsic 3-D structure or ripples due to the instability of 2-D crystals[26, 162]. However, the structures characterized had been exposed to photoresist, leaving the possibility that effects of chemical residues may have influenced the observed structure. Carefully controlling the experimental variables such as the influence of the substrate and the presence of impurities is necessary to interpret observed transport properties correctly.

In this letter, we report atomic structure and nanoscale morphology of monolayer graphene sheets and nanotubes in the most commonly used device configurations (i.e. on an insulating SiO_2 substrate with conducting back gate and fabricated electrical contacts). We find that acrylic lithography resists, commonly used in the device fabrication procedure, introduce unknown and uncontrollable perturbations, which must also apply to the majority of previously reported graphene-

devices. The removal of the residue is necessary for uncovering intrinsic structural properties of the graphene sheet. Upon removing the resist residue, we are able to acquire atomic-resolution images of the graphene lattice, which shows both triangular and hexagonal lattice patterns in close proximity, indicating significant scattering of the electron waves. The atomic-resolution images also prove that our graphene devices are clean to atomic-scale, enabling controlled analysis of the structural properties. Finally, we measure the thickness of a graphene film in ultra high vacuum (UHV) and in ambient, and show that the large height measured in ambient is due to significant presence of atmospheric species under and/or on the graphene film.

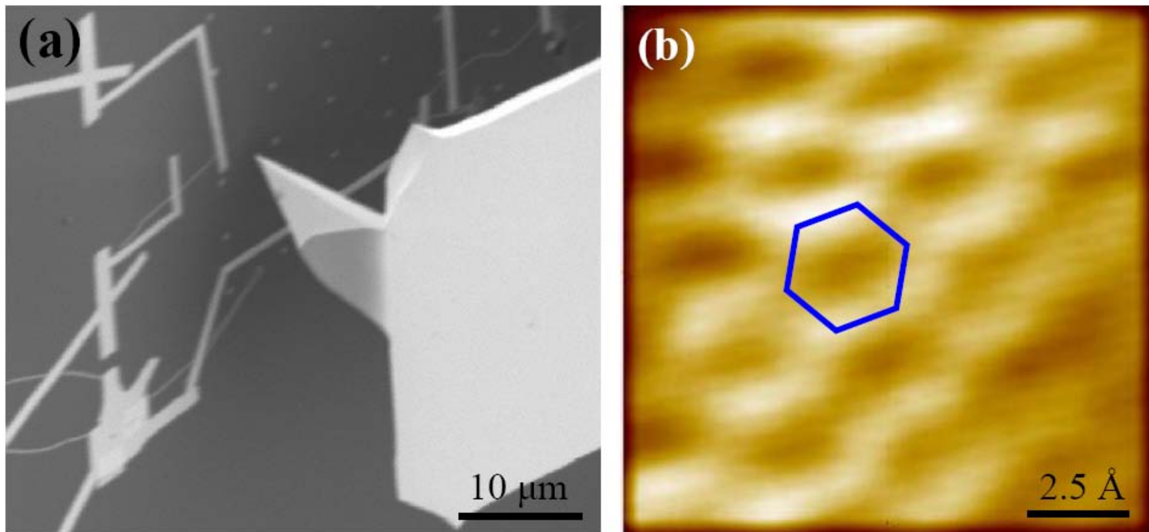

Figure A1.1 (a) Scanning electron micrograph of a carbon nanotube device, showing our experimental setup. The triangular shape to the right of the image is the tip of the scanning probe. The nanotubes were grown using chemical vapor deposition following reference[163] and the electrodes were patterned using a standard two-step electron-beam lithography process[34] The device substrate is 500 nm thick thermal SiO_2 grown on a heavily-doped silicon wafer. Wide, near vertical lines on the left are electrical contacts. Thin white lines are the nanotubes lying on the surface of SiO_2. (b) An STM image of a nanotube in the device configuration, showing atomic structure. $V_{source}=V_{drain}=1.4$ v, $V_{gate}= 0$ v, and $I_{tunnel}=18$ pA.

We use scanning tunneling microscopy (STM) to achieve atomic-scale resolution, while we compare nanoscale morphologies of graphene and silicon dioxide substrate by non-contact atomic force microscopy (AFM). Unless otherwise noted, our microscopy studies were performed in UHV. In graphene devices, only

the electronic contacts and graphene are conducting while the gate dielectric, which is insulating, composes the vast majority of the device substrate. Since STM requires conductive substrates, the STM tip must be positioned exactly above only the conductive areas, which extend laterally only several nanometers to microns for graphene devices. We use a commercial ultra high vacuum (UHV) system[164], which features a field emission scanning electron microscope (SEM) combined with AFM and STM for rapid, reproducible placement of scanned probe. Figure A1.1a is an SEM image showing the scanned-probe tip approaching a representative carbon nanotube device to demonstrate our tip placement capability. In Figure A1.1a, the nanotubes appear as thin curved white lines and the source/drain electrodes as the wider near-vertical lines, and a conductive AFM cantilever[37] is visible on the right. Coarse positioning of the cantilever within several microns of the nanotube is performed using SEM. We then utilize non-contact frequency-shift AFM[165] to locate the nanotube and to place the cantilever within several nanometers of the nanotube. Finally, the cantilever is employed as the STM tip; the tunneling current travels from the cantilever into the nanotube and along the nanotube into the electrodes. STM imaging is limited to the nanotube. As shown in Figure A1.1b, this integrated technique is successful in resolving the atomic structure of nanotubes in the device configuration.

Figure A1.2a is an AFM image of the graphene-based device, which we discuss in this paper. The wide white line, approximately 1 μm in width, is one electrode. The contacted graphitic material varies in the thickness but the large section appearing to the lower left is uniformly one monolayer thick, as will be shown later.

We find that a continuous film covers the surface of the graphene devices after the lift-off procedure, and it is not possible to obtain atomic resolution images via STM. A similar film was seen on the majority of nanotube segments in the nanotube devices, with only localized clean segments suitable for imaging. A control experiment using the same resist deposition[19] and acetone resist liftoff procedures on highly oriented pyrolytic graphite (HOPG) yields the same film, confirming its origin as residue from the resist. This indicates that the resist residue covers all graphene

devices fabricated using similar photoresist process. Standard solvents such as Nano Remover PG[27] and glacial acetic acid do not perturb the residue. Known resist cleaning processes are inadequate for completely removing the resist residue.

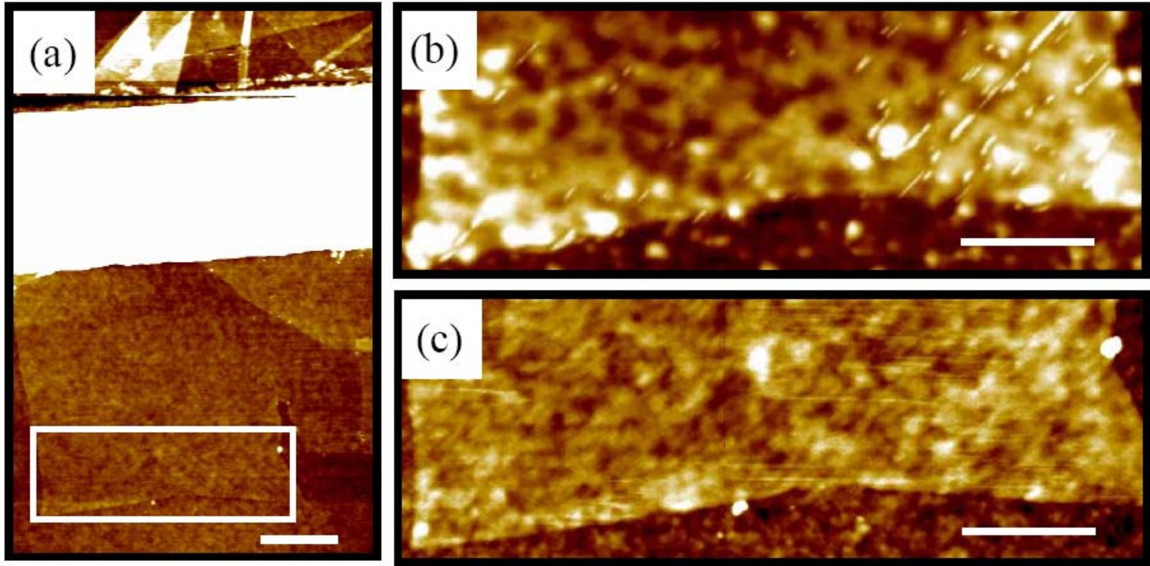

Figure A1.2 (a) AFM topography of graphene deposited on SiO_2. Thin graphite flakes are generated using the mechanical exfoliation technique[45] on thermally grown SiO_2 with the thickness of 300 nm. Monolayer graphite flakes (graphene) are located using optical and atomic force microscopy[47]. The e-beam lithography defined electrode[34], approximately 80 nm in height and 1.5 μm in width, is the white area nearly horizontal to the image. The black square indicates the region shown in Figures A1.1b and A1.1c. The scale bar is 500 nm. (b) Graphene sheet prior to the cleaning procedure described in text. The scale bar is 300 nm. (c) Graphene sheet after the cleaning procedure. The standard deviation of the height variation in a square of side 600 nm is approximately 3 Å after the treatment compared to 8 Å before the treatment. The scale bar is 300 nm. Images (a)-(c) were acquired using intermittent-contact mode AFM in air.

We are able to remove the photoresist residue in argon/hydrogen atmosphere at 400 °C[43]. Figure A1.2c shows the AFM image of the same area shown in Figure A1.2b, after the heat treatment. The graphene sheet now appears with finer, smoother corrugations. A representative large-area STM image of the cleaned graphene sheet is shown in Figure A1.3. The atomic-scale pattern is visible in Figure A1.3a, and can be imaged clearly at higher resolution as shown in Figure A1.3b and A1.3d. The meandering of atomic rows seen in Figure A1.3d is due to the curvature of the surface

[166]. The observed lattice spacing is consistent with the graphene lattice, and the appearance of both triangular and hexagonal lattice in the image indicates the presence of strong spatially dependent perturbations which interact with graphene electronic states[167, 168]. Such perturbations may be due to the observed film curvature and/or the charge traps on the SiO_2 surface. Significantly, STM images at any position on the device always reveal the graphitic lattice. Therefore, surface impurities have been removed completely from the graphene surface, and the corrugation seen in Figure A1.2c is representative of the clean graphene sheet on SiO_2.

The material thickness is one of the key structural factors in determining the properties of graphene-based devices[156]. Figure A1.4a shows an AFM image of the boundary between the same graphene sheet and SiO_2 substrate. A histogram acquired across the boundary shown in Figure A1.4b shows that the film thickness is 4.2 Å, comparable to the layer-to-layer spacing in bulk graphite of 3.4 Å. Therefore, the imaged graphene device area is a monolayer. Similar analysis performed in air for the same area, before our experiments in UHV, shows the thickness to be 9 Å, consistent with a previous measurement of a monolayer material in air[45, 47]. The discrepancy between the air/vacuum measurements of 4.6 Å in thickness indicates a significant presence of ambient species (nitrogen, oxygen, argon, or water) between SiO_2 and the graphene sheet and/or on the graphene sheet.

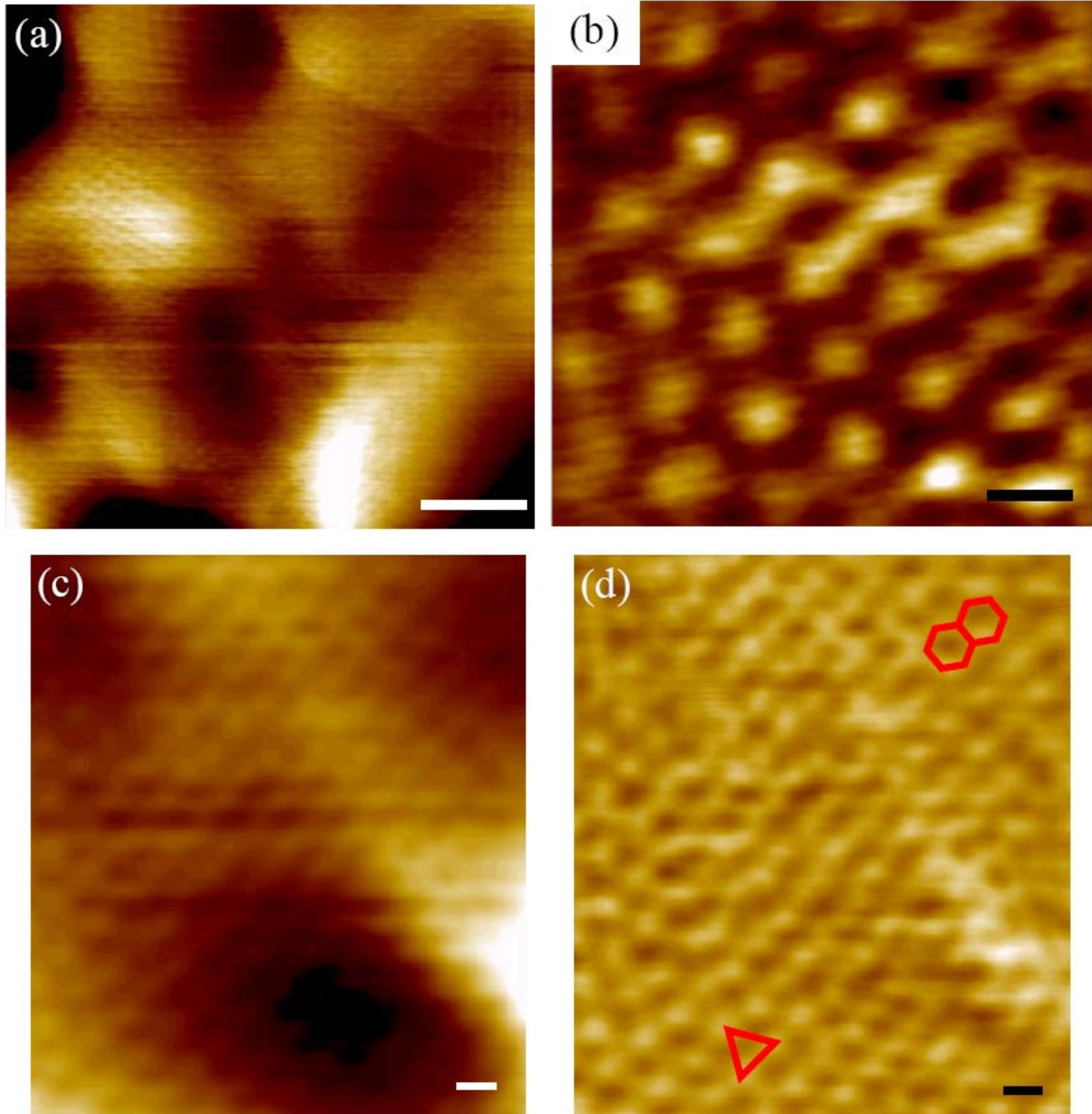

Figure A1.3 (a) A typical large-area STM image of the graphene sheet shown in Figure A1.2a. Peak-to-peak height variation of the image is approximately 2.5 nm. V_{sample} = 1.1 V and I_{tunnel} = 0.3 nA. The scale bar is 2 nm. (b) Atomically-resolved image of a graphene sheet. V_{sample} = 1.0 V and I_{tunnel} = 24 pA. The scale bar is 2.5 Å. (c) STM image of another area. The scale bar is 2.5 Å.V_{sample} = 1.2v and I_{tunnel} = 0.33 nA. (d) A high-pass filtered image of the large area scan shown in (c). Both triangular and hexagonal patterns are observed. The orientations of the red triangle and hexagons are same. The scale bar is 2.5 Å.

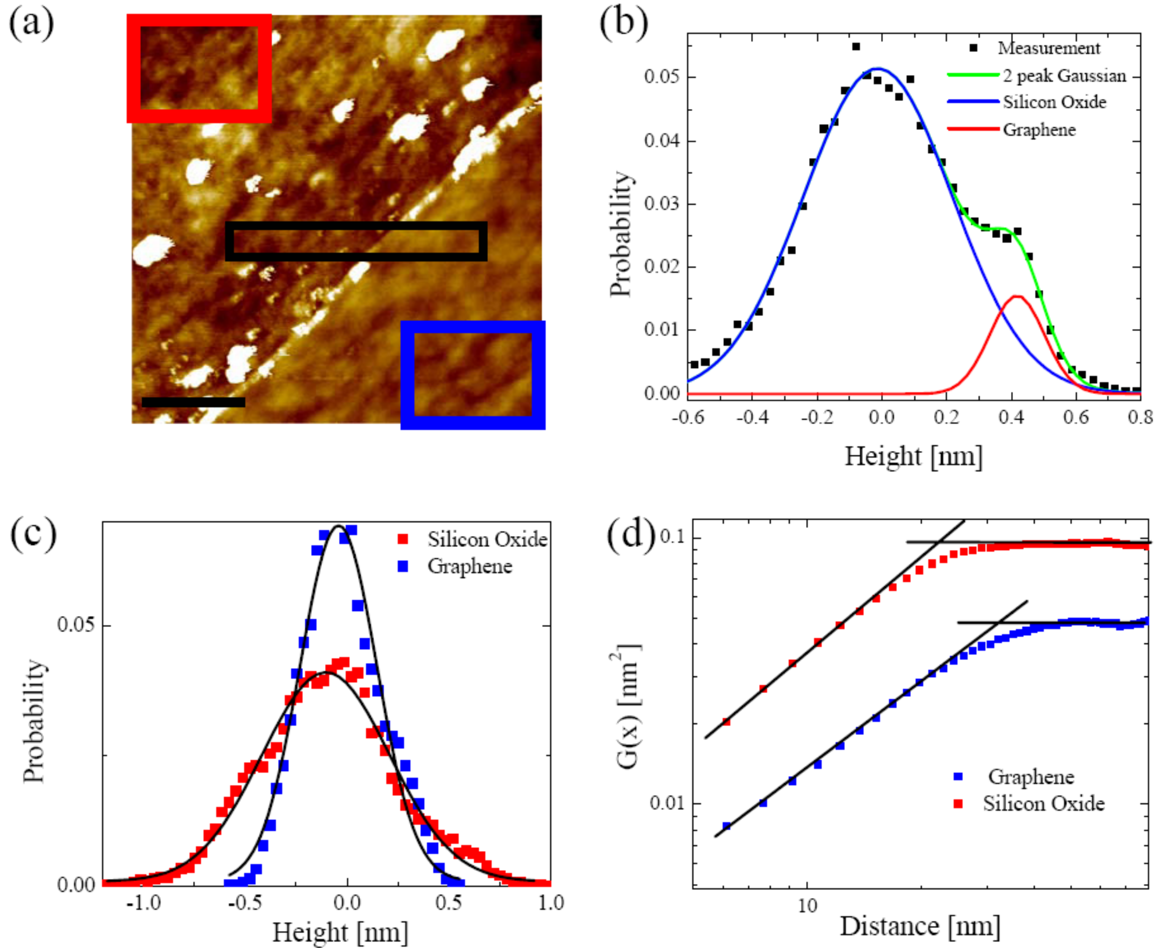

Figure A1.4 (a) Non-contact mode AFM image, acquired in UHV, of a boundary between the graphene sheet and SiO_2 substrate. The graphene sheet occupies the lower right area of the image. The scale bar is 200 nm. The black rectangle indicates the area for the histogram shown in Figure A1.4b, and red and blue rectangles indicate the area where the histograms shown in Figure A1.4c has been acquired. (b) Height histogram acquired across the graphene-substrate boundary (black rectangle in Figure A1.4a). The data are fit by two Gaussian distributions (solid red and blue lines; green line is sum), with means separated by 4.2 Å. (c) Height histograms acquired on graphene and SiO_2 (red and blue squares respectively in Figure A1.4a). The histograms are well-described by Gaussian distributions (black lines) with standard deviations of 1.9 Å and 3.1Å for graphene and SiO_2, respectively. (d) The height-height correlation function (see text) of the graphene sheet and SiO_2 surface. The lines are fits to the large and small length behaviors (power-law and constant, respectively), and the point of intersection indicates the correlation length. This analysis is performed by selecting data from Figure A1.4a, showing both graphene and SiO_2 surfaces. Therefore, the tip morphology is the same for both curves and the tip-related artifact effect does not contribute to the analysis.

We now turn our attention to the 3-D morphology of the graphene sheet, important for the transport properties [158]. Figure A1.4c shows histograms of the heights over graphene and SiO_2. The graphene sheet is approximately 60% smoother than the oxide surface; the standard deviations of the measured height variations are 1.9 Å and 3.1 Å for the graphene and oxide surface. The height-height correlation function, $g(x) = \left\langle (z(x_0 + x) - z(x_0))^2 \right\rangle$, is a useful measure for characterizing the surface morphology[68, 169, 170]. Figure A1.4d shows the height-height correlation function[15] for the graphene and SiO_2 surface. Both correlation functions rapidly increase as $g \sim x^{2H}$ at short distances, as expected [169]: 2H = 1.11 ± 0.013 for graphene and 2H = 1.17 ± 0.014 for SiO_2. A value of the exponent 2H ~ 1 indicates a domain structure with short-range correlations among neighboring domains [68] and is not surprising for SiO_2. A value of 2H = 2 is expected[67] for a thermally-excited flexible membrane under the influence of an interaction (e.g. van der Waals) with the substrate. Consequently, the observed 2H value demonstrates that the observed graphene morphology is not representative of the intrinsic structure. A rollover at the correlation length and saturation at mean square roughness at large distances follow the short-distance behavior. As seen in the figure inset, interpolating the intersection of the power-law and saturated regimes yields values of the correlation length[169], which are $\xi = 32 \pm 1$ nm for graphene and $\xi = 23 \pm 0.6$ nm for SiO_2. The similar exponents and slightly larger correlation length of the graphene sheet is consistent with the graphene morphology being determined by the underlying SiO_2 substrate. The larger correlation length and smaller roughness of the graphene surface would arise naturally due to an energy cost for graphene to closely follow sharp orientation changes on the substrate. Freestanding graphene has been reported to have larger static nanoscale corrugations[26, 162] attributed to intrinsic structural instability of 2D materials. However, the free-standing graphene was treated with a resist process[26, 162], and the resulting resist residue could certainly prevent the graphene sheet from reaching its equilibrium structural corrugation.

The observed corrugations in our study indicate a maximum local strain of approximately 1 %. Using the Young's modulus of 1 TPa [171] and graphene thickness of 3.4 Å, the corresponding stored energy density due to the induced

deformation is ~1 meV/Å^2. We estimate the graphene-SiO_2 interaction energy to be >6 meV/Å^2 based on the interlayer van der Waals interaction in graphite [172] of 20 meV/Å^2 at the distance of 3.4 Å. The estimated interaction energy between the graphene sheet and SiO_2 substrate is thus sufficient to overcome the energy cost of the corrugations needed for graphene to follow the SiO_2 morphology.

Corrugations comparable to those observed here have been postulated to be responsible for the lack of low-field magnetoresistance observed in graphene on SiO_2 via suppression of weak localization due to the introduction of an effective random magnetic field [158]. Indeed, "flatter" graphene films, prepared on SiC with the film coherence length of 90 nm, show weak localization [24]. The corrugations in graphene on SiO_2 were later attributed to intrinsic corrugations in the graphene itself [162]. However, our findings indicate that the graphene corrugations that are relevant for interpreting many reports of device performance (e.g. for graphene on SiO2) are due to partial conformation of the graphene to the SiO_2, not to the intrinsic corrugation of graphene.

We have resolved atomic structures of oxide-supported graphene-based electronic devices using a novel combined SEM/AFM/STM technique. We obtain real-space images of the single-layer graphene atomic lattice for the first time, and characterize the thicknesses and nanoscale corrugation of a clean graphene sheet devoid of any impurities. Our observation shows that the graphene primarily follows the underlying morphology of SiO_2 and thus does not have intrinsic, independent corrugations on SiO_2. The graphene sheets *do* have finite intrinsic stiffness, which prevents the sheets from conforming completely to the substrate. In addition, we demonstrate that resist residues are ubiquitous on lithographically-fabricated graphene devices, and their presence should be considered in interpreting transport and structural measurements of earlier studies. Our quantitative measure of the extrinsic corrugations of graphene on SiO_2 can be used as input to theoretical models of strain-induced disorder in graphene and its effect on transport properties. Furthermore, our observation that graphene can conform to substrate morphology suggests new experimental directions: the use of controlled substrate morphologies (e.g. a patterned SiO_2 substrate, or alternative dielectric materials) may be a useful

approach to investigate how the corrugation-induced strain impacts the transport properties of graphene. Finally, our technique (the novel integrated microscopy allied with the resist cleaning process) can be applied to resolve atomic structures of nanoelectronic devices in general; the technique finally enables studies of the impact of atomic scale defects and adsorbates on nanoscale transport properties.

A2: Corrugation effects of graphene on SiO_2[8]

To determine the role of corrugations in charge carrier scattering, the surface corrugation of graphene on SiO_2 was measured by non-contact mode AFM and STM in UHV. Figure A2.1 (a) shows an AFM image of graphene as well as the neighboring SiO_2 substrate, and Figure A2.1(b) shows the corresponding Fourier spectra of rectangular areas in the graphene region and the bare SiO_2 region. The Fourier spectra is obtained from a 230 nm × 393 nm area in graphene (blue rectangle in Figure A2.1(a)) and a 230 nm × 258 nm area in SiO_2 (red rectangle in Figure A2.1(a)), by taking the one-dimensional Fourier spectra of each horizontal line (fast scan direction) and average the spectra from the lines in the same rectangular area together [69]. The rectangular areas are chosen to avoid any dirt particles and edges while getting the largest data set for averaging. The fact that the Fourier amplitude of the graphene topography closely follows that of the SiO_2 topography, and shows no additional structure, strongly suggests that graphene is not perturbed by the AFM measurement [69, 173], which might not be the case in STM measurements where the tip-sample interaction force could be large enough to perturb graphene [69, 174]. Figure A2.1(c) shows the height-height correlation function for the graphene and SiO_2 surface [38]. Notably, graphene is smoother than the SiO_2 substrate, suggesting that the finite stiffness of graphene acts to smooth out corrugations. Both correlation functions rapidly increase as $g(r) \sim r^{2H}$ at short distances, with similar effective exponents $2H = 1.11 \pm 0.013$ for graphene and $2H = 1.17 \pm 0.014$ for SiO_2. A

[8] This chapter was adapted from a section of: J.-H. Chen, C. Jang, M. Ishigami, S. Xiao, W.G. Cullen, E. D. Williams, and M. S. Fuhrer, Solid State Communications **149**, 1080 (2009)

crossover at the correlation length and saturation at mean square roughness at large distances follow the short-distance behavior. As seen in the figure inset, interpolating the intersection of the power-law and saturated regimes yields values of the correlation length [169], which are $\xi = 32 \pm 1$ nm for graphene and $\xi = 23 \pm 0.6$ nm for SiO_2. The similar exponents and slightly larger correlation length of the graphene sheet is consistent with the graphene morphology being *determined* by the underlying SiO_2 substrate; the larger correlation length and smaller roughness of the graphene surface arise naturally due to the energy cost for out-of-plane deformation of graphene. The measured effective exponent of $2H \sim 1$ for graphene on SiO_2 indicates that corrugations of graphene on SiO_2 should result in a conductivity nearly independent of charge carrier density according to equation 3.3, therefore similar to short-ranged scattering [65], which may contribute to the carrier-density-independent term σ_{sr} discussed in Section 4.

A quantitative evaluation of the impact of the ripples requires a realistic understanding of their structure and amplitude[69]. The one-dimensional Fourier transform *A(q)*, shown in Figure A2.1(b) allows us to estimate the local radius of curvature as $\rho = 1/q^2 A(q)$. Using the minimum measured amplitude, at the maximum wave-vector sampled $q_{max} = 2$ nm^{-1}, the minimum local radius of curvature is ~ 27 nm. This value is limited by the ability of the tip to respond at small lateral spacings. By extrapolating the power-law region in Figure A2.1(b) to q_{max} an upper estimate for the minimum local radius of curvature range is found, ~ 61 nm. The resistivity due to scattering from such corrugations σ_{corr}^{-1} is expected to be proportional to *qA(q)* [65, 175], which is ~ 0.008 to 0.018 in this case. The small value of *qA(q)* suggests that

that σ_{corr}^{-1} is small in magnitude and unlikely to contribute significantly to the sum in equation 1.1.

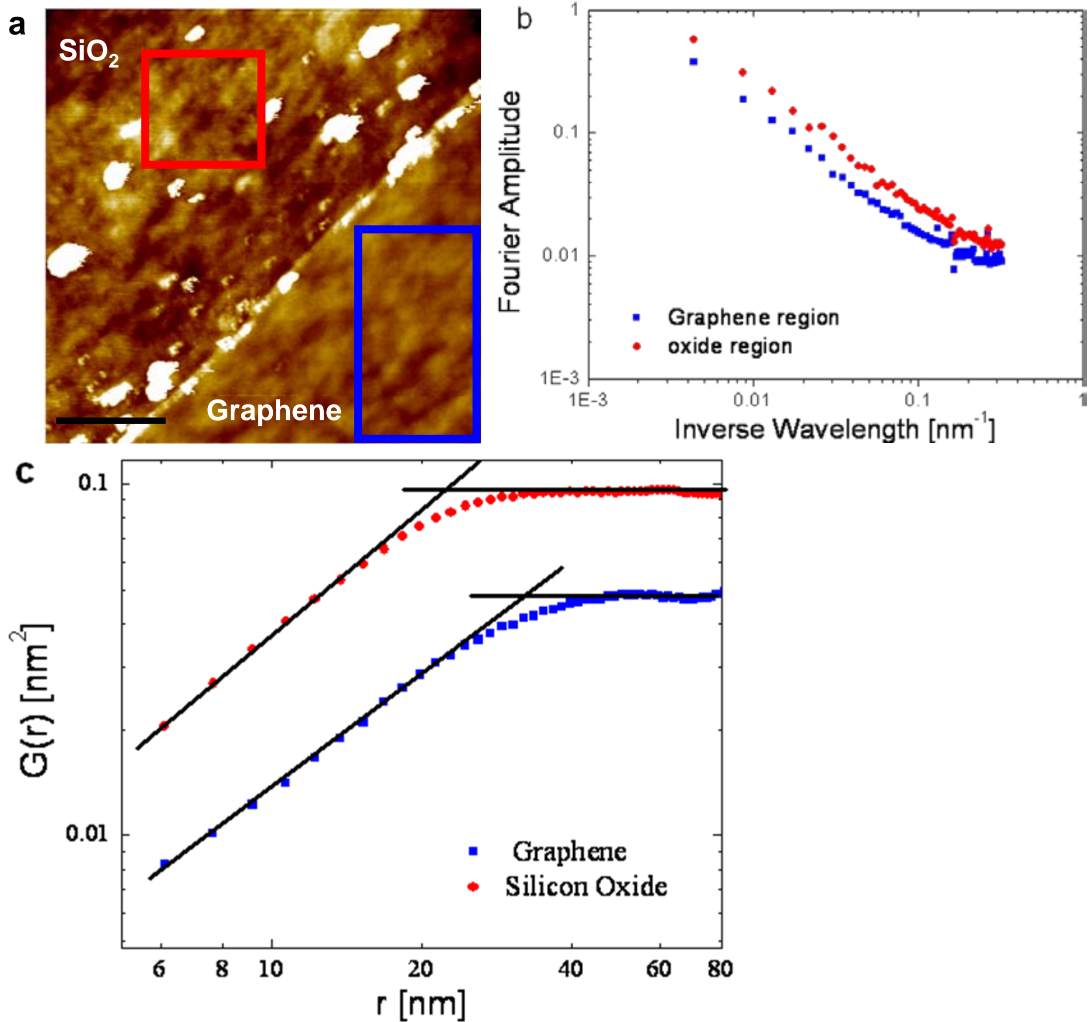

Figure A2.1 (a) Non-contact mode AFM image, acquired in UHV, of a boundary between the graphene sheet and SiO_2 substrate. The graphene sheet occupies the lower right area of the image. The scale bar is 200 nm. (b) The Fourier spectra of rectangular areas in the bare SiO_2 region (red rectangle) and the region covered with graphene (blue rectangle). (c) The height-height correlation function (G(r), see text) of the graphene sheet and SiO_2 surface. The lines are fits to the large and small length behaviors (power-law and constant, respectively), and the point of intersection indicates the correlation length. This analysis is performed by selecting data from Figure A2.1(a), showing both graphene and SiO_2 surfaces in one scan, thus excluding the contribution of any tip-related artifact to the analysis.

A3: Tuning the effective fine structure constant in graphene[9]

Abstact

We reduce the dimensionless interaction strength α in graphene by adding a water overlayer in ultrahigh vacuum, thereby increasing dielectric screening. The mobility limited by long-range impurity scattering is increased over 30%, due to the background dielectric constant enhancement leading to a reduced interaction of electrons with charged impurities. However, the carrier-density-independent conductivity due to short-range impurities is decreased by almost 40%, due to reduced screening of the impurity potential by conduction electrons. The minimum conductivity is nearly unchanged, due to canceling contributions from the electron-hole puddle density and long-range impurity mobility. Experimental data are compared with theoretical predictions with excellent agreement.

[9] This chapter is adapted from: C. Jang, S. Adam, J.-H. Chen, E.D. Williams, S. Das Sarma, and M.S. Fuhrer, Phys. Rev. Lett. **101**, 146805 (2008)

Most theoretical and experimental work on graphene has focused on its gapless, linear electronic energy dispersion $E = hv_F k/2\pi$. One important consequence of this linear spectrum is that the dimensionless coupling constant α (or equivalently r_s, defined here as the ratio between the graphene Coulomb potential energy and kinetic energy) is a carrier-density independent constant [49, 176, 177], and as a result, the Coulomb potential of charged impurities in graphene is renormalized by screening, but strictly maintains its long-range character. Thus there is a clear dichotomy between long-range and short-range scattering in graphene, with the former giving rise to a conductivity linear [49, 52, 177] in carrier density (constant mobility), and the latter having a constant conductivity independent of carrier density. Charged impurity scattering necessarily dominates at low carrier density, and the minimum conductivity at charge neutrality is determined by the charged impurity scattering and the self-consistent electron and hole puddles of the screened impurity potential [31, 34, 52, 53].

Apart from the linear spectrum, an additional striking aspect of graphene, setting it apart from all other two-dimensional electron systems, is that the electrons are confined to a plane of atomic thickness. This fact has a number of ramifications which are only beginning to be explored [178, 179]. One such consequence is that graphene's properties may be tuned enormously by changing the surrounding environment. Here we provide a clear demonstration of this by reducing the dimensionless coupling constant α in graphene by more than 30 percent through the addition of a dielectric layer (ice) on top of the graphene sheet. Upon addition of the ice layer, the mobility limited by long-range scattering by charged impurities

increases by 31 percent, while the conductivity limited by short-range scatterers *decreases* by 38 percent. The minimum conductivity value remains nearly unchanged. The opposing effects of reducing α on short-and long-range scattering are easily understood theoretically. The major effect on long-range scattering is to reduce the Coulomb interaction of electrons with charged impurities, reducing the scattering [180]. In contrast, the dielectric does not modify the atomic-scale potential of short-range scatterers, and there the leading effect is the reduction of screening by the charge carriers, which increases scattering resulting in lower high-density conductivity. Such screening of short-range potentials has been predicted theoretically [125, 181], although in other 2D systems, this effect is difficult to observe experimentally. The minimum conductivity is nearly unchanged due to competing effects of increased mobility and reduced carrier concentration in electron-hole puddles due to reduced screening [53, 103].

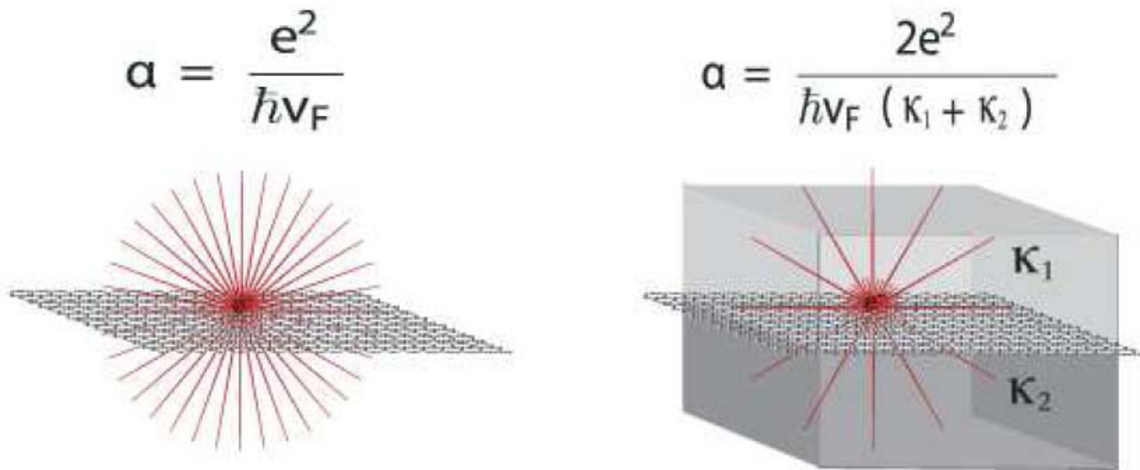

Figure A3.1 Schematic illustrating dielectric screening in graphene. The dielectric environment controls in the interaction strength parameterized by the coupling constant α.

Figure A3.1 illustrates the effect of the dielectric environment on graphene. For graphene sandwiched between two dielectric slabs with κ_1 and κ_2,

$$\alpha = \frac{4\pi e^2}{(\kappa_1 + \kappa_2) h v_F} \quad \text{(A3.1)}$$

where e is the electronic charge, h is the Planck's constant, and v_F is the Fermi velocity, which we take to be 1.1×10^6 ms^{-1} [44, 47, 182]. Typically, graphene transport experiments [31, 34, 44, 47] are performed on a SiO_2 substrate with $\kappa_1 \approx 3.9$ and in air/vacuum $\kappa_2 \approx 1$, making graphene a weakly interacting electron system with $\alpha \approx 0.8$ (although very recently work on substrate-free graphene [27] explored the strong coupling regime with $\alpha \approx 2$). Here we deposit ice ($\kappa_2 \approx 3.2$ [183]) on graphene on SiO_2, decreasing α from ≈ 0.81 to ≈ 0.56.

Graphene is obtained by mechanical exfoliation of Kish graphite on a SiO_2 (300 nm)/Si substrate [44]. The heavily n-doped silicon substrate is used as a back gate. Graphene monolayers are identified from the color contrast in an optical microscope image and confirmed by Raman spectroscopy [76]. The final device (see Figure A3.2 inset) was fabricated by patterning electrodes using electron beam lithography and thermally evaporated Cr/Au, followed by annealing in Ar/H_2 to remove resist residue (see Refs. [34, 38] for details). The experiments are performed in a cryostat cold finger placed in an ultra high vacuum (UHV) chamber. In order to remove residual adsorbed gases on the device and the substrate, the sample was baked at 430 K over-night in UHV following a vacuum bakeout. The conductivity was measured using a conventional four-probe technique with an ac current of 50 nA at a base pressure ~ 10^{-10} torr and device temperature ~ 77 K. Deionized nano-pure water was introduced through a leak valve attached to the chamber. The water gas pressure

(determined by a residual gas analyzer) was $5 \pm 3 \times 10^{-8}$ torr. The amount of ice deposited was estimated by assuming a sticking coefficient of unity and the ice I_h layer density of 9.54×10^{14} cm^{-2} [184, 185].

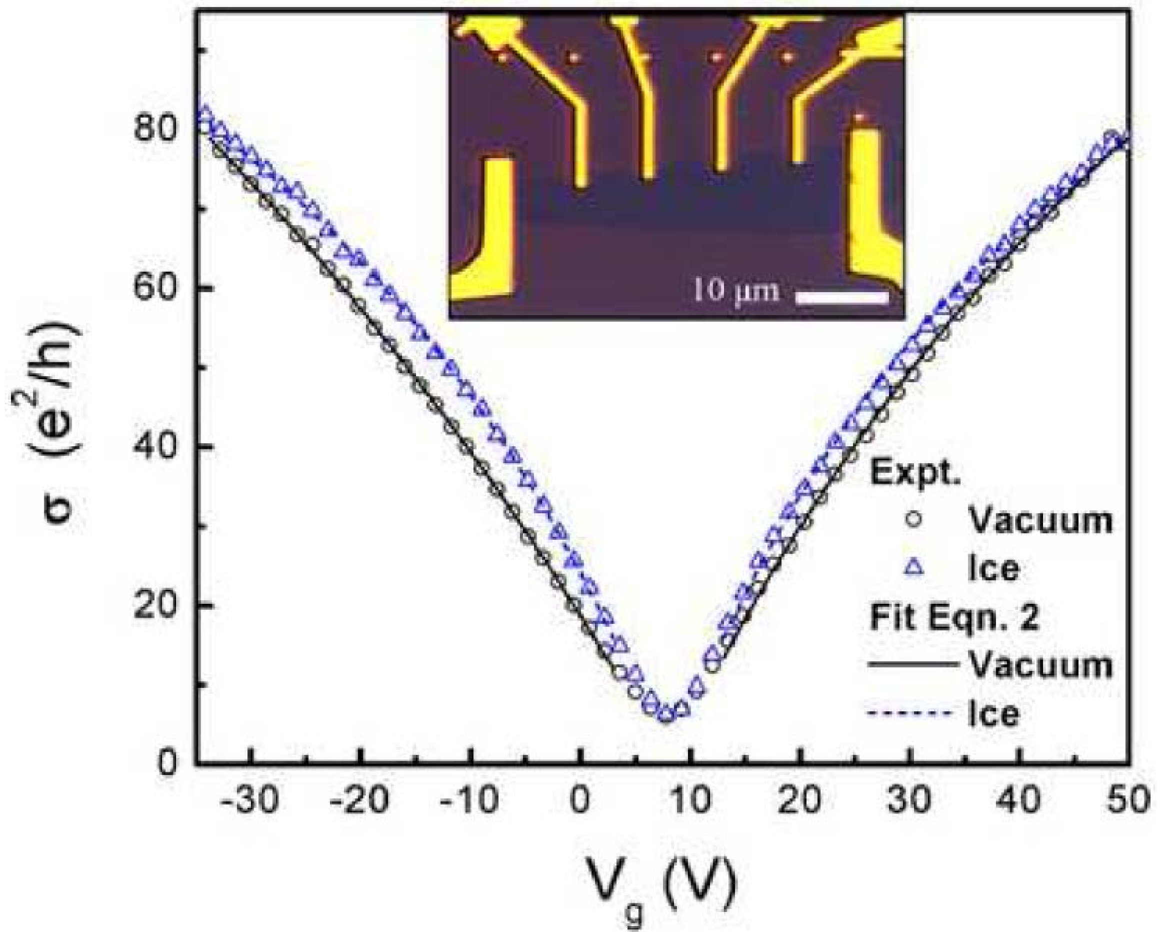

FigureA3.2 Conductivity of the graphene device as a function of back-gate voltage for pristine graphene (circles) and after deposition of 6 monolayers of ice (triangles). Lines are fits to Eq.A3.2. Inset: Optical microscope image of the device.

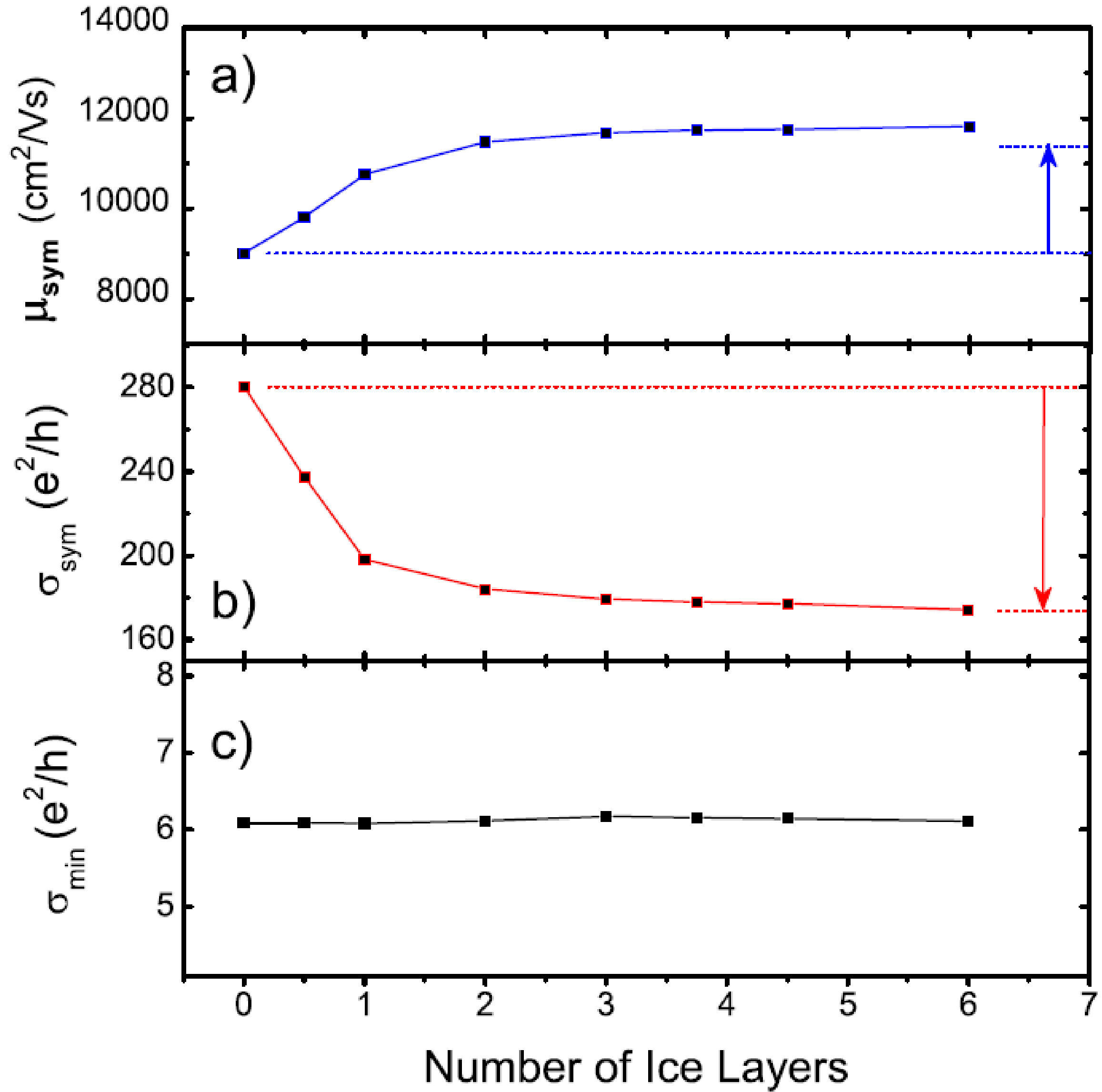

Figure A3.3 μ_{sym}, σ_{sym} and σ_{min} as a function of number of ice layers. Dashed lines show the values for pristine graphene and corresponding theoretical expectations for the ice-covered device.

Figure A3.2 shows conductivity as a function of gate voltage for two different sample conditions, pristine graphene and ice-covered graphene. We observe several interesting effects of adding ice: (i) The offset gate voltage at which the conductivity is a minimum $V_{g,min}$ remains unchanged; (ii) the minimum conductivity σ_{min} value remains unchanged, (iii) the maximum slope of $\sigma(V_g)$ becomes steeper, and (iv) the

curve $\sigma(V_g)$ in the presence of ice is more non-linear and crosses that of the pristine sample at some large carrier density. All these features can be understood qualitatively from the physical picture described above, and we show below that they are in quantitative agreement with the predictions of Boltzmann transport theory including screening within the Random Phase Approximation (RPA).

In order to interpret the experimental results quantitatively, we fit the conductivity data to [104]

$$\sigma^{-1}(V_g, \alpha) = (ne\mu)^{-1} + \sigma_s^{-1}, \tag{A3.2}$$

where $n = c_g |V_g - V_{g,min}|$, e is the electric charge and $c_g = 1.15 \times 10^{-8}$ V/cm^2 is the gate capacitance per unit area for the 300 nm thick SiO_2. Since the transport curves are not symmetric about the minimum gate voltage, the fitting is performed separately for positive and negative carrier densities (i.e. electron and hole carriers), excluding data close to the Dirac point conductivity plateau ($V_{g,min} \pm 5$V). We report both the symmetric μ_{sym} (σ_{sym}) and anti-symmetric μ_{asym} (σ_{asym}) contributions to the mobility (conductivity). Shown also in Figure A3.2 is the result of the fit for pristine graphene and after deposition of 6 monolayers of ice.

Figure A3.3 shows μ_{sym}, σ_{sym} and σ_{min} as a function of number of ice layers. The mobility (Figure A3.3a) of pristine graphene is 9,000 cm^{2}V^{-1}s^{-1}, which is typical for clean graphene devices on SiO_2 substrates at low temperature. As the number of water layers increases, the mobility *increases*, and saturates after about 3 layers of ice to about 12,000 cm^{2}V^{-1}s^{-1}. In contrast, the conductivity due to short-range scatterers (Figure A3.3b) decreases from 280e^2/h to 170e^2/h. The decrease in conductivity due to short-range scatterers shows a similar saturation behavior as the mobility,

suggesting they have the same origin[10]. The absence of any sharp change in the conductivity or mobility at very low ice coverage rules out ice itself acting as a significant source of short- or long-range scattering. This is corroborated by the absence of a shift in the gate voltage of the minimum conductivity, consistent with physisorbed ice [184] not donating charge to graphene [31, 34, 53]. Figure A3.3c shows that the minimum conductivity is essentially unchanged during the addition of ice.

		Theory	Experiment
Long-range (symmetric): $\frac{\mu_{sym}^{ice}}{\mu_{sym}^{vac}} = \frac{F_l(\alpha^{vac})}{F_l(\alpha^{ice})}$	Ref.[53]	1.26	1.31
Short-range (symmetric): $\frac{\sigma_{sym}^{ice}}{\sigma_{sym}^{vac}} = \frac{F_s(\alpha^{vac})}{F_s(\alpha^{ice})}$	Ref.[175]	0.62	0.62
Minimum Conductivity: $\frac{\sigma_{\min}^{ice}}{\sigma_{\min}^{vac}} = \frac{n^*(\alpha^{ice})F_l(\alpha^{vac})}{n^*(\alpha^{vac})F_l(\alpha^{ice})}$	Ref.[53]	0.99	1.00
Long-range (anti-symmetric): $\frac{\mu_{asym}^{ice}}{\mu_{asym}^{vac}} = \frac{F_l(\alpha^{vac})\alpha^{ice}}{F_l(\alpha^{ice})\alpha^{vac}}$	Ref.[54]	0.87	0.17
Short-range (anti-symmetric): $\frac{\sigma_{asym}^{ice}}{\sigma_{asym}^{vac}}$	Ref.[186]		0.13

Table A3.1 Summary of our results in corresponding theoretical predictions.

[10] The saturation behavior shown in Fig. A3.3 indicates that the ice film is continuous well before the formation of 6 full ice layers, and has reached a constant value of the dielectric constant. Bulk dielectric constant has been observed in ultrathin films of SiO2, see K. Hirose et al., Phys. Rev. B 67, 195313 (2003), and it is reasonable to assume that these ultrathin ice layers have the bulk dielectric constant of ice.

We now analyze the experimental results within Boltzmann transport theory. The conductivity of graphene depends strongly on the coupling constant α. For screened long-range impurities within RPA, we have [53]

$$\sigma_l = \frac{2e^2}{h}\frac{n}{n_{imp}}\frac{1}{F_l(\alpha)},$$
$$F_l(\alpha) = \pi\alpha^2 + 24\alpha^3(1-\pi\alpha) + \frac{16\alpha^3(6\alpha^2-1)\arccos(1/2\alpha)}{\sqrt{4\alpha^2-1}}, \qquad \text{(A3.3)}$$

where in the last term, for $\alpha < 0.5$ both $arcos(1/(2\alpha))$ in the numerator and $\sqrt{4\alpha^2-1}$ in the denominator are purely imaginary so that $F_l(\alpha)$ is real and positive for all α. For screened short-range impurities, we have [175]

$$\sigma_s = \frac{\sigma_0}{F_s(\alpha)},$$
$$F_s(\alpha) = \frac{\pi}{2} - \frac{32\alpha}{3} + 24\alpha^2 + 320\alpha^3(1-\pi\alpha) + \frac{256\alpha^3(5\alpha^2-1)\arccos(1/2\alpha)}{\sqrt{4\alpha^2-1}},$$

(A3.4)

where similarly $F_s(\alpha)$ is real and positive. Consistent with the physical picture outlined earlier, in the limit $\alpha \rightarrow 0$, $\sigma_l \sim \alpha^{-2}$ which describes the scaling of the Coulomb scattering matrix element, while for short-range scattering, $\sigma_s \approx$ const $(1 + (64/3\pi)\,\alpha)$ where increased screening of the potential by the carriers gives the leading order increase in conductivity. For the experimental values of α, the full functional form of F_s and F_l should be used[11]. Dashed lines in Figures A3.3a-b show the

[11] Results beyond the RPA approximation have been examined in A. V. Shytov et al., Phys. Rev. Lett. 99, 236801 (2007), R. R. Biswas et al., Phys. Rev. B 76, 205122 (2007), V. M. Pereira et al., Phys. Rev. Lett. 99, 166802 (2007), I. S. Terekhov et al., Phys. Rev. Lett. 100, 076803 (2008), M. S. Foster et al. Phys. Rev. B 77, 195413 (2008) and M. Mueller et al., arXiv:0805.1413v1 (2008). We believe that these effects are unobservable in the current experiment. Also M. Trushin et al. Europhys. Lett. 83, 17001 (2008) consider a phenomenological Yukawa potential. Generally one uses a model Yukawa potential in studying systems where the microscopic nature of the screened potential is unknown which is not the case for graphene. For the Yukawa potential, we find $F_y = \pi\alpha^2+8\alpha^3- \pi\alpha(1+4\alpha^2)^{0.5}$ which is qualitatively similar to Eq. A3.3.

theoretical expectations for μ_{sym} and σ_{sym} for vacuum and ice on graphene in quantitative agreement with experiment.

Regarding the magnitude of the minimum conductivity, it was recently proposed [53] that one can estimate σ_{min} by computing the Boltzmann conductivity of the residual density n^* that is induced by the charged impurities. This residual density (i.e. rms density of electrons and hole puddles) has been seen directly in scanning probe experiments [187] and in numerical simulations [103]. We therefore use Eq. A3.3, but replace n with $n^* = \langle V_D^2 \rangle / \left(\pi \left(h v_F / 2\pi \right)^2 \right)$ (where the angular brackets indicate ensemble averaging over configurations of the disorder potential V_D) to give [53]

$$\sigma_{min} = \frac{2e^2}{h} \frac{1}{F_l(\alpha)} \frac{n^*(\alpha)}{n_{imp}},$$
$$\langle V_D^2 \rangle = n_{imp} \left(\frac{h v_F \alpha}{2\pi} \right)^2 \int dq \left(\frac{e^{-qt}}{q\varepsilon(q)} \right)^2, \qquad \text{(A3.5)}$$

where $\varepsilon(q)$ is the RPA dielectric function and $d \approx 1$ nm is the typical impurity separation from the graphene sheet. The dominant contribution to both the disorder potential $\langle V_D^2 \rangle$ and $F_l(\alpha)$ is the Coulomb matrix element, giving $n^* \sim n_{imp}\alpha^2$ and $1/F_l(\alpha) \sim 1/\alpha^2$ so that to leading order, σ_{min} is unchanged by dielectric screening[12].

---

[12] Estimating the charged impurity density $n_{imp} \approx 5.5\times10^{10}$ cm^2 (which is comparable to similar experiments [31] Y.-W. Tan, Y. Zhang, K. Bolotin, *et al.*, *Measurement of Scattering Rate and Minimum Conductivity in Graphene*, Phys. Rev. Lett. **99**, 246803 (2007)[34] J.-H. Chen, C. Jang, M. S. Fuhrer, *et al.*, *Charged Impurity Scattering in Graphene*, Nat. Phys. **4**, 377 (2008).) we find [53] S. Adam, E. H. Hwang, V. M. Galitski, *et al.*, *A self-consistent theory for graphene transport*, Proc. Natl. Acad. Sci. USA **104**, 18392 (2007). σ_{min}(ice) = σ_{min}(vac) ≈ 6.66/6.72 ≈ 0.99. The minimum conductivity (Fig. A3.3c) shows almost no variation with ice layers, in agreement with this theoretical expectation. We ignore quantum coherent effects such as localization (see e.g. I. Aleiner and K. Efetov, Phys. Rev. Lett. 97, 236801 (2006)) which are not expected to be important at 77 K, and are not experimentally observed [31] Y.-W. Tan, Y. Zhang, K. Bolotin, *et al.*, *Measurement of Scattering Rate and Minimum Conductivity in Graphene*, Phys. Rev. Lett. **99**, 246803 (2007)[34] J.-

The experimental data also show a mobility asymmetry (between electrons and holes) of about 10 percent. Novikov [54] argued that for Coulomb impurities in graphene such an asymmetry is expected since electrons are slightly repelled by the negative impurity centers compared to holes resulting in slightly higher mobility for electrons (since $V_{g,min} > 0$, we determine that there are more negatively charged impurity centers, see also Ref. [34]}); and that for unscreened Coulomb impurities $\mu_{usc}(\pm V_g) \sim [C_2 \alpha^2 \pm C_3 \alpha^3 + C_4\alpha^4 + \ldots]^{-1}$. From the magnitude of the asymmetry, we know that $C_3\alpha^3 << C_2\alpha^2$, but if we further assume that $C_4 \alpha^4 << C_3\alpha^3$ (although, in the current experiment, we cannot extract the value of C_4), then including the effects of screening gives $\mu_{asym} \sim \alpha/F_1(\alpha)$.

In Table A3.1 we show all the experimental fit parameters and compare them to theoretical predictions. The quantitative agreement for μ_{sym}, σ_{min} and σ_{sym} is already highlighted in Figure A3.3, while we have only qualitative agreement for μ_{asym}, probably because the condition $C_4 \alpha^4 << C_3 \alpha^3$ does not hold in our experiments. There is no theoretical expectation of asymmetry in σ_s; the experimental asymmetry (about 30 percent) could be explained by contact resistance [186] which we estimate to be a 20 percent correction to σ_s for our sample geometry.

In conclusion we have observed the effect of dielectric environment on the transport properties of graphene. The experiment highlights the difference between long-range and short-range potential scattering in graphene. The enhanced μ_l (i.e. the

---

H. Chen, C. Jang, M. S. Fuhrer, *et al.*, *Charged Impurity Scattering in Graphene*, Nat. Phys. **4**, 377 (2008)[44] K. S. Novoselov, A. K. Geim, S. V. Morozov, *et al.*, *Two-dimensional gas of massless Dirac fermions in graphene*, Nature **438**, 197 (2005)[47] Y. Zhang, Y.-W. Tan, H. L. Stormer, *et al.*, *Experimental observation of the quantum Hall effect and Berry's phase in graphene*, Nature **438**, 201 (2005)[104] S. V. Morozov, K. S. Novoselov, M. I. Katsnelson, *et al.*, *Giant Intrinsic Carrier Mobilities in Graphene and Its Bilayer*, Phys. Rev. Lett. **100**, 016602 (2008). down to 30 mK (see: Ref. [84] Y.-W. Tan, Y. Zhang, H. L. Stormer, *et al.*, *Temperature Dependent Electron Transport in Graphene*, Eur. Phys. J. **148**, 15 (2007).).

slope of σ against density) and reduced σ_s (i.e. the constant conductivity at high density) are attributed to the decreased interaction between charged carriers and impurities and decreased screening by charge carriers, respectively, upon an increase in background dielectric constant with ice deposition in UHV. These variations quantitatively agree with theoretical expectations for the dependence of electron scattering on graphene's "fine structure constant" within the RPA approximation. This detailed knowledge of the scattering mechanisms in graphene is essential for design of any useful graphene device, for example, use of a high-κ gate dielectric will increase the transconductance of graphene at the expense of linearity, an important consideration for analog applications. As demonstrated here, dielectric deposition only improved mobility by 30 percent, however the use of high-κ dielectric overlayers could significantly enhance this result.

A4: Supplementary information for Chapter 6

A4.1 Experimental Methods

Cleaned graphene devices are fabricated according to methods described in chapter 4. Electronic transport experiments were carried out at base pressures lower than 5×10^{-10} torr and $T = 10$ K for He^+ irradiation and 40-80 K for Ne^+ irradiation, to avoid Ne adsorption on graphene. A sputter gun ionized He or Ne gas and accelerated the ions to 500 eV. A shutter controlled the irradiation time and allowed measurement of $\sigma(V_g)$ *in situ* between irradiation doses. The pressure of the inert gas, up to $5*10^{-8}$ torr for Ne and up to $2.5*10^{-7}$ torr for He, was monitored by a residual gas analyzer and the ion flux calibrated by a Faraday cup mounted at the same location as the sample in a control experiment. After irradiation, each device was annealed at 485K overnight before further experimental runs were performed.

The Raman spectra of pristine and defected graphene were acquired in ambient condition before and after the transport measurement which was done in continuous high vacuum to ultra high vacuum condition. The comparison between L_a (from the Raman I_D/I_G value, see text) and the transport mean free path was made using the Raman spectra and the $\sigma(V_g)$ curves, both acquired in ambient condition.

A4.2 Derivation of Equation 6.2 in main text

Eq. (6.2) is obtained by putting $\tau_d = \frac{k_F}{\pi^2 v_F n_d}\ln^2(k_F R)$ (Eq. (54) from Ref. [63]) and $k_F = \sqrt{\pi n}$ into $\sigma_d = \frac{2e^2}{h} k_F v_F \tau_d$, where k_F is the Fermi wavevector, v_F the

Fermi velocity, R the defect radius, n the carrier density, n_d the defect density and τ_d the defect scattering time.

A4.3 Interpretation of the offset in the dependence of 1/μ on ion dosage

Assuming the initial disorder is due to charged impurities, the offset yields [53] values of $n_c \sim 4\times10^{11}$ cm^{-2} and $\sim 5\times10^{11}$ cm^{-2} respectively for the samples exposed to Ne^+ and He^+ ion irradiation. If such offset were ascribed to lattice defect scattering, extrapolating to $1/\mu\rightarrow0$, it would indicate a defect concentration on order of 10^{11}cm^{-2}. However, lattice defects at this concentration should produce a prominent Raman D band, and depress the minimum conductivity. Additionally, experiments to tune the dielectric constant in graphene [39] indicate that the native impurities in exfoliated graphene are charged impurities. The mobility of 200,000 cm^2/Vs achieved in suspended graphene samples [27] can be used to estimate an upper bound on the native lattice defect density of exfoliated graphene of $\sim 6\times10^9$ cm^{-2}.

A4.4 Possible trapped noble-gas atoms at the graphene-SiO_2 interface

Although we expect the majority of noble-gas ions to implant into the SiO_2 substrate after reaching the graphene layer, some incident noble gas ions might become neutral atoms and stay at the graphene-SiO_2 interface after the irradiation and subsequent annealing. There are two possible effects that a trapped noble gas atom could have on the transport properties of graphene: it could scatter electrons by 1) acting like a weak short-range scatter or 2) increase the roughness (rippling) of graphene. We are convinced, however, that such trapped gas atoms would not affect

the transport properties significantly because 1) as illustrated in Figure 6.3b, the density-independent resistivity ρ_s does not change significantly with increasing dosage; 2) As shown by Marton et al. [188], a trapped noble gas atom induce a very mild bump on graphene, with the local radius of curvature comparable to that induced by the SiO_2 substrate [36], which should have negligible effect on the electronic transport properties of graphene [36].

A5: Supplementary information for Chapter 7

A5.1 Sample Geometry and Raman Spectra

Figures A5.1a – A5.1c show optical micrographs of the three devices used in this study. Figures A5.1d – A5.1f show the corresponding Raman spectra of the devices acquired over the device area using a confocal micro-Raman spectrometer with 633 nm excitation wavelength. The single Lorentzian 2D peak indicates the samples are single-layer graphene[76].

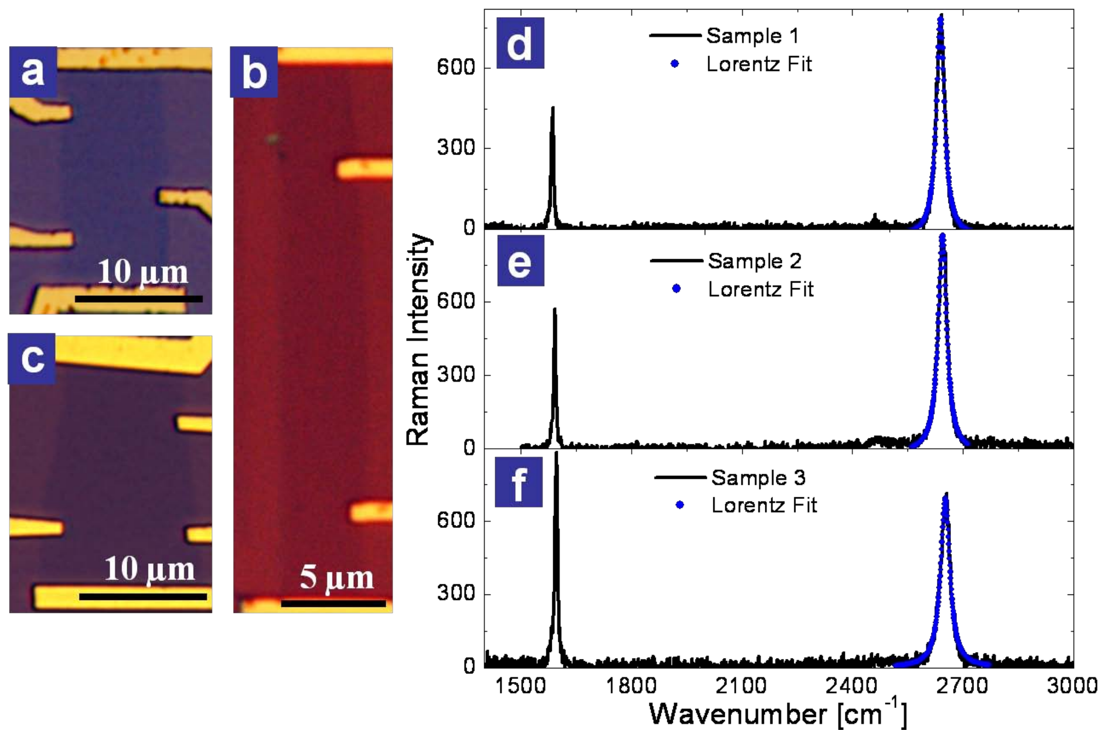

Figure A5.1 Optical micrographs and Raman Spectra of the three graphene samples. a, b, c, Optical micrographs of Sample 1, 2 and 3, respectively. d, e, f, Raman spectra of Sample 1, 2 and 3, respectively. The blue dots are fits to Lorentzian lineshapes.

A5.2 Temperature Dependence of the maximum resistivity

The resistivity at the minimum conductivity point (MCP) behaves very differently from the resistivity at higher carrier density ($V_g > 10$ V). Figure A5.2 shows the maximum resistivity as a function of temperature $\rho_{max}(T)$ for the two samples presented in Figure 7.2 and one lower-mobility sample (Sample 3) for which we have more limited temperature-dependent data. $\rho_{max}(T)$ is highly sample-dependent, increasing with T for Samples 1 and 2, and decreasing with T for Sample 3. The latter behavior is expected for increased screening of the impurity potential by excited carriers[49, 51] and the relative size of this effect should depend on the impurity density. This effect is expected to scale with T/T_F, and hence should be largest near the MCP. Furthermore, the effect is predicted to be small for $T < T_F = [363\text{ K}]\times[V_g(\text{V})]^{1/2}$, which is well-satisfied except very near the MCP; which justifies the exclusion of screening in the analysis of the temperature dependence at non-zero V_g. The data for $\rho_{max}(T)$ for Sample 1 are also slightly different on warming and cooling, perhaps due to gases adsorbed on the sample at low T, consistent with $\rho_{max}(T)$ being highly dependent on the disorder in the sample. Taken together, the $\rho_{max}(T)$ data suggest an interplay of impurity screening and phonon scattering; more work will be need to disentangle these effects.

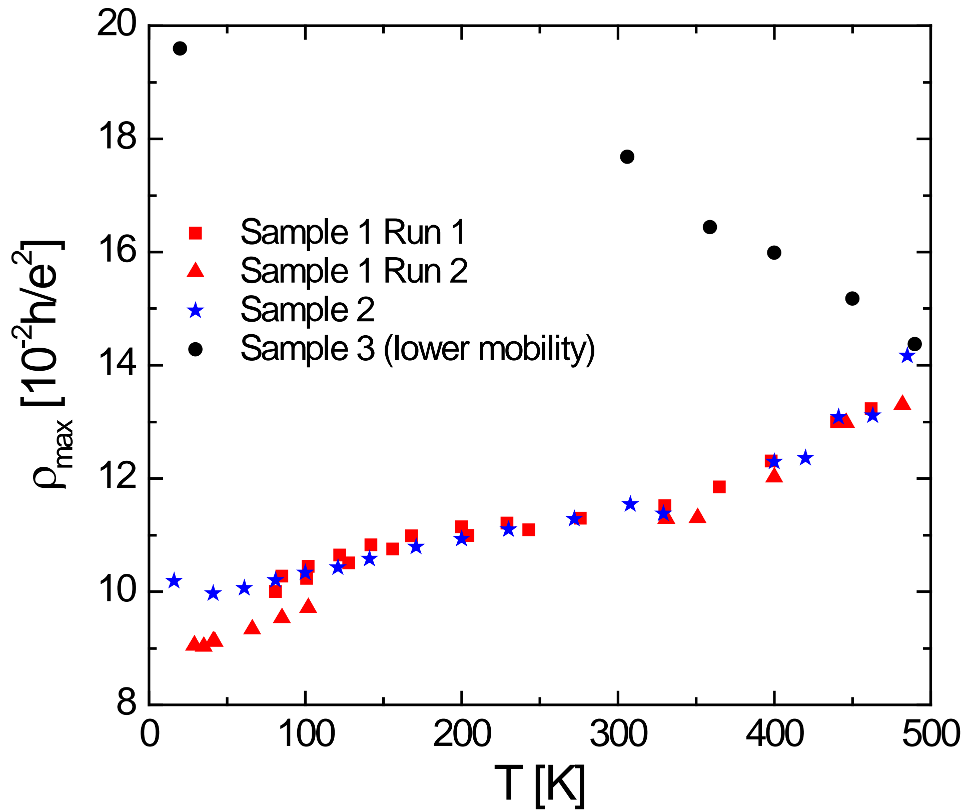

Figure A5.2 Temperature dependence of the maximum resistivity. The maximum resistivities $\rho(V_g = 0,T)$ of graphene Sample 1, 2 and 3 are shown as a function of temperature. Sample 1 and Sample 2 show increasing conductivity with temperature, though the functional form differs from Equation 7.2. Sample 3 has lower mobility than Sample 1 and Sample 2, and shows a decreasing conductivity with increasing temperature.

Bibliography

1. J. Wiseman, United States Patent, (1844), Vol. US 00043444.
2. E. D. McCracken, United States Patent, (1870), Vol. US 105351.
3. W. M. Canfield, United States Patent, (1870), Vol. US 110432.
4. B. C. Brodie, *Researches on the atomic weight of graphite*, Quart. J., Chem. Soc. **12**, 261 (1860).
5. F. C. Calvert, *On the composition of a carbonaceous substance existing in grey cast iron*, Quart. J., Chem. Soc. **14**, 199 (1862).
6. P. R. Wallace, *The Band Theory of Graphite*, Phys. Rev. **71**, 622 (1947).
7. J. C. Slonczewski and P. R. Weiss, *Band Structure of Graphite*, Phys. Rev. **109**, 272 (1958).
8. J. W. McClure, *Diamagnetism of Graphite*, Phys. Rev. **104**, 666 (1956).
9. T. Inoshita, K. Nakao, and H. Kamimura, *Electronic Structure of Potassium-Graphite Intercalation Compound: C_8K*, J. Phys. Soc. Jpn. **43**, 1237 (1977).
10. M. S. Dresselhaus and G. Dresselhaus, *Intercalation compounds of graphite*, Advances in Physics **30**, 139 (1981).
11. N. Emery, C. Hérold, M. dAstuto*, et al.*, *Superconductivity of Bulk CaC_6*, Phys. Rev. Lett. **95**, 087003 (2005).
12. Q. M. Zhang and J. Z. Larese, *Melting of monolayer argon adsorbed on a graphite substrate*, Phys. Rev. B **43**, 938 (1991).
13. M. Caragiu and S. Finberg, *Alkali metal adsorption on graphite: a review*, J. Phys.: Condens. Matter **17**, R995 (2005).
14. H. Ulbrichta, R. Zachariab, N. Cindirc*, et al.*, *Thermal desorption of gases and solvents from graphite and carbon nanotube surfaces*, Carbon **44**, 2931 (2006).
15. C. R. Clemmer and T. P. Beebe, Jr., *Graphite: A Mimic for DNA and Other Biomolecules in Scanning Tunneling Microscope Studies*, Science **251**, 640 (1991).
16. R. E. Peierls, *Quelques proprietes typiques des corpses solides*, Ann. I. H. Poincare **5**, 177 (1935).
17. L. Landau, Physikalische Zeitschrift der Sowjetunion **11**, 26 (1937).
18. N. D. Mermin, *Crystalline Order in Two Dimensions*, Phys. Rev. **176**, 250 (1968).
19. A. E. Karu and M. Beer, *Pyrolytic Formation of Highly Crystalline Graphite Films*, J. Appl. Phys. **37**, 2179 (1966).
20. M. Eizenberg and J. M. Blakely, *Carbon monolayer phase condensation on Ni(111)*, Surf. Sci. **82**, 228 (1979).
21. C. Oshima and A. Nagashima, *Ultra-thin epitaxial films of graphite and hexagonal boron nitride on solid surfaces*, J. Phys.: Condens. Matter **9**, 1 (1997).
22. J. W. May, *Platinum surface LEED rings*, Surf. Sci. **17**, 267 (1969).

[23] I. Forbeaux, J. M. Themlin, and J. M. Debever, *Heteroepitaxial graphite on 6H-SiC(0001): Interface formation through conduction-band electronic structure*, Phys. Rev. B **58**, 16396 (1998).
[24] C. Berger, Z. Song, X. Li, *et al.*, *Electronic Confinement and Coherence in Patterned Epitaxial Graphene*, Science **312**, 1191 (2006).
[25] K. S. Novoselov, A. K. Geim, S. V. Morozov, *et al.*, *Electric Field Effect in Atomically Thin Carbon Films*, Science **306**, 666 (2004).
[26] J. C. Meyer, A. K. Geim, M. I. Katsnelson, *et al.*, *The structure of suspended graphene sheets*, Nature **446**, 60 (2007).
[27] K. I. Bolotin, K. J. Sikes, Z. Jiang, *et al.*, *Ultrahigh electron mobility in suspended graphene*, Solid State Commun. **146**, 351 (2008).
[28] J. S. Bunch, A. M. van der Zande, S. S. Verbridge, *et al.*, *Electromechanical Resonators from Graphene Sheets*, Science **315**, 490 (2007).
[29] C. Lee, X. Wei, J. W. Kysar, *et al.*, *Measurement of the Elastic Properties and Intrinsic Strength of Monolayer Graphene*, Science **321**, 385 (2008).
[30] R. R. Nair, P. Blake, A. N. Grigorenko, *et al.*, *Fine Structure Constant Defines Visual Transparency of Graphene*, Science **320**, 1308 (2008).
[31] Y.-W. Tan, Y. Zhang, K. Bolotin, *et al.*, *Measurement of Scattering Rate and Minimum Conductivity in Graphene*, Phys. Rev. Lett. **99**, 246803 (2007).
[32] K. Sugihara, K. Kawamura, and T. Tsuzuku, *Temperature Dependence of the Average Mobility in Graphite*, J. Phys. Soc. Jpn. **47**, 1210 (1979).
[33] J.-H. Chen, W. G. Cullen, C. Jang, *et al.*, *Defect Scattering in Graphene*, Phys. Rev. Lett. (in press), preprint at arXiv:0903.2602 (2009).
[34] J.-H. Chen, C. Jang, M. S. Fuhrer, *et al.*, *Charged Impurity Scattering in Graphene*, Nat. Phys. **4**, 377 (2008).
[35] J.-H. Chen, C. Jang, S.Xiao, *et al.*, *Intrinsic and extrinsic performance limits of graphene devices on* SiO_2, Nat. Nanotechnol. **3**, 206 (2008).
[36] J.-H. Chen, C. Jang, M. Ishigami, *et al.*, *Diffusive Charge Transport in Graphene on* SiO_2, Solid State Commun. **149**, 1080 (2009).
[37] J.-H. Chen, M. Ishigami, C. Jang, *et al.*, *Printed Graphene Circuits*, Adv. Mater. **19**, 3623 (2007).
[38] M. Ishigami, J.-H. Chen, W. G. Cullen, *et al.*, *Atomic Structure of Graphene on SiO2*, Nano Lett. **7**, 1643 (2007).
[39] C. Jang, S. Adam, J.-H. Chen, *et al.*, *Tuning the Effective Fine Structure Constant in Graphene: Opposing Effects of Dielectric Screening on Short- and Long-Range Potential Scattering*, Phys. Rev. Lett. **101**, 146805 (2008).
[40] C. Schonenberger, *Bandstructure of Graphene and Carbon Nanotubes: An Exercise in Condensed Matter Physics*, Tutorial at <http://pages.unibas.ch/phys-meso/Education/Teaching/Nanotubes/LCAO-NT.pdf> (2000).
[41] C. L. Kane and E. J. Mele, *Size, Shape, and Low Energy Electronic Structure of Carbon Nanotubes*, Phys. Rev. Lett. **78**, 1932 (1997).
[42] N. H. Shon and T. Ando, *Quantum Transport in Two-Dimensional Graphite System*, J. Phys. Soc. Jpn. **67**, 2421 (1998).
[43] P. L. McEuen, M. Bockrath, D. H. Cobden, *et al.*, *Disorder, Pseudospins, and Backscattering in Carbon Nanotubes*, Phys. Rev. Lett. **83**, 5098 (1999).

[44] K. S. Novoselov, A. K. Geim, S. V. Morozov, *et al.*, *Two-dimensional gas of massless Dirac fermions in graphene*, Nature **438**, 197 (2005).

[45] K. S. Novoselov, D. Jiang, F. Schedin, *et al.*, *Two-dimensional atomic crystals*, Proc. Natl. Acad. Sci. U. S. A. **102**, 10451–10453 (2005).

[46] Y. Zhang, J. P. Small, W. V. Pontius, *et al.*, *Fabrication and electric-field-dependent transport measurements of mesoscopic graphite devices*, Appl. Phys. Lett. **86**, 073104 (2005).

[47] Y. Zhang, Y.-W. Tan, H. L. Stormer, *et al.*, *Experimental observation of the quantum Hall effect and Berry's phase in graphene*, Nature **438**, 201 (2005).

[48] A. K. Geim and K. S. Novoselov, *The rise of graphene*, Nat Mater **6**, 183 (2007).

[49] T. Ando, *Screening Effect and Impurity Scattering in Monolayer Graphene*, J. Phys. Soc. Jpn. **75**, 074716 (2006).

[50] K. Nomura and A. H. MacDonald, *Quantum Transport of Massless Dirac Fermions*, Phys. Rev. Lett. **98**, 076602 (2007).

[51] V. V. Cheianov and V. I. Fal'ko, *Friedel Oscillations, Impurity Scattering, and Temperature Dependence of Resistivity in Graphene*, Phys. Rev. Lett. **97**, 226801 (2006).

[52] E. H. Hwang, S. Adam, and S. Das Sarma, *Carrier Transport in Two-Dimensional Graphene Layers*, Phys. Rev. Lett. **98**, 186806 (2007).

[53] S. Adam, E. H. Hwang, V. M. Galitski, *et al.*, *A self-consistent theory for graphene transport*, Proc. Natl. Acad. Sci. USA **104**, 18392 (2007).

[54] D. S. Novikov, *Numbers of donors and acceptors from transport measurements in graphene*, Appl. Phys. Lett. **91**, 102102 (2007).

[55] P. Van Mieghem, *Theory of band tails in heavily doped semiconductors*, Rev. Mod. Phys. **64**, 755 (1992).

[56] E. Fradkin, *Critical behavior of disordered degenerate semiconductors. I. Models, symmetries, and formalism*, Phys. Rev. B **33**, 3257 (1986).

[57] A. W. W. Ludwig, M. P. A. Fisher, R. Shankar, *et al.*, *Integer quantum Hall transition: An alternative approach and exact results*, Phys. Rev. B **50**, 7526 (1994).

[58] M. I. Katsnelson, *Zitterbewegung, chirality, and minimal conductivity in graphene*, Eur. Phys. J. B **51**, 157 (2006).

[59] J. Tworzydlo, B. Trauzettel, M. Titov, *et al.*, *Sub-Poissonian Shot Noise in Graphene*, Phys. Rev. Lett. **96**, 246802 (2006).

[60] K. Ziegler, *Robust Transport Properties in Graphene*, Phys. Rev. Lett. **97**, 266802 (2006).

[61] M. Hentschel and F. Guinea, *Orthogonality catastrophe and Kondo effect in graphene*, Phys. Rev. B **76**, 115407 (2007).

[62] M. I. Katsnelson, K. S. Novoselov, and A. K. Geim, *Chiral tunnelling and the Klein paradox in graphene*, Nat. Phys. **2**, 620 (2006).

[63] T. Stauber, N. M. R. Peres, and F. Guinea, *Electronic transport in graphene: A semi-classical approach including midgap states*, Phys. Rev. B **76**, 205423 (2007).

[64] A. Fasolino, J. H. Los, and M. I. Katsnelson, *Intrinsic ripples in graphene*, Nat Mater **6**, 858 (2007).

[65] M. I. Katsnelson and A. K. Geim, *Electron scattering on microscopic corrugations in graphene*, Phil. Trans. R. Soc. A **366**, 195 (2008).
[66] R. C. Thompson-Flagg, M. J. B. Moura, and M. Marder, *Rippling of Graphene*, http://arxiv.org/abs/0807.2938 (2008).
[67] H. Aranda-Espinoza and D. Lavallee, *Structure factor of flexible membranes*, Europhys. Lett. **43**, 355 (1998).
[68] J. L. Goldberg, X.-S. Wang, N. C. Bartelt, *et al.*, *Surface height correlation functions of vicinal Si(111) surfaces using scanning tunneling microscopy*, Surf. Sci. Lett. **249**, L285 (1991).
[69] W. G. Cullen, J.-H. Chen, M.Ishigami, *et al.*, In preparation (2009).
[70] L. Pietronero, S. Strässler, H. R. Zeller, *et al.*, *Electrical conductivity of a graphite layer*, Phys. Rev. B **22**, 904 (1980).
[71] E. H. Hwang and S. D. Sarma, *Acoustic phonon scattering limited carrier mobility in two-dimensional extrinsic graphene*, Phys. Rev. B **77**, 115449 (2008).
[72] L. M. Woods and G. D. Mahan, *Electron-phonon effects in graphene and armchair (10,10) single-wall carbon nanotubes*, Phys. Rev. B **61**, 10651 (2000).
[73] K. Hess and P. Vogl, *Remote polar scattering in silicon inversion layers*, Solid State Commun. **30**, 807 (1979).
[74] M. V. Fischetti, D. A. Neumayer, and E. A. Cartier, *Effective electron mobility in Si inversion layers in metal-oxide-semiconductor systems with high-k insulator: The role of remote phonon scattering*, J. Appl. Phys. **90**, 4587 (2001).
[75] S. Fratini and F. Guinea, *Substrate-limited electron dynamics in graphene*, Phys. Rev. B **77**, 195415 (2008).
[76] A. C. Ferrari, J. C. Meyer, V. Scardaci, *et al.*, *Raman Spectrum of Graphene and Graphene Layers*, Phys. Rev. Lett. **97**, 187401 (2006).
[77] Advanced Research Systems, LT-3B product description.
[78] D. R. Hines, V. W. Ballarotto, E. D. Williams, *et al.*, *Transfer printing methods for the fabrication of flexible organic electronics*, J. Appl. Phys. **101**, 024503 (2007).
[79] D. R. Hines, S. Mezhenny, M. Breban, *et al.*, *Nanotransfer printing of organic and carbon nanotube thin-film transistors on plastic substrates*, Appl. Phys. Lett. **86**, 163101 (2005).
[80] Stanford Research Systems, Application note # 3.
[81] N. M. R. Peres, F. Guinea, and A. H. Castro Neto, *Electronic properties of disordered two-dimensional carbon*, Phys. Rev. B **73**, 125411 (2006).
[82] E.-A. Kim and A. H. C. Neto, *Graphene as an electronic membrane*, Europhys. Lett. **84**, 57007 (2008).
[83] M. Trushin and J. Schliemann, *The Minimum Electrical and Thermal Conductivity of Graphene: Quasiclassical Approach*, Phys. Rev. Lett. **99**, 216602 (2007).
[84] Y.-W. Tan, Y. Zhang, H. L. Stormer, *et al.*, *Temperature Dependent Electron Transport in Graphene*, Eur. Phys. J. **148**, 15 (2007).

[85] S. Cho and M. S. Fuhrer, *Charge Transport and Inhomogeneity near the Charge Neutrality Point in Graphene*, Phys. Rev. B **77**, 084102R (2008).
[86] P. Sjovall, *Intercalation of potassium in graphite studied by thermal desorption spectroscopy*, Surf. Sci. **345**, L39 (1996).
[87] F. Schedin, A. K. Geim, S. V. Morozov*, et al.*, *Detection of individual gas molecules adsorbed on graphene*, Nat. Mater. **6**, 652 (2007).
[88] E. H. Hwang, S. Adam, and S. D. Sarma, *Transport in chemically doped graphene in the presence of adsorbed molecules*, Phys. Rev. B **76**, 195421 (2007).
[89] E. Ziambaras, J. Kleis, E. Schroder*, et al.*, *Potassium intercalation in graphite: A van der Waals density-functional study*, Phys. Rev. B **76**, 155425 (2007).
[90] G. M. Rutter, J. N. Crain, N. P. Guisinger*, et al.*, *Scattering and Interference in Epitaxial Graphene*, Science **317**, 219 (2007).
[91] E. Stolyarova, K. T. Rim, S. Ryu*, et al.*, *High-resolution scanning tunneling microscopy imaging of mesoscopic graphene sheets on an insulating surface*, Proc. Natl. Acad. Sci. USA **104**, 9209 (2007).
[92] J. H. Bardarson, J. Tworzydlo, P. W. Brouwer*, et al.*, *One-Parameter Scaling at the Dirac Point in Graphene*, Phys. Rev. Lett. **99**, 106801 (2007).
[93] H. Suzuura and T. Ando, *Crossover from Symplectic to Orthogonal Class in a Two-Dimensional Honeycomb Lattice*, Phys. Rev. Lett. **89**, 266603 (2002).
[94] S. Stankovich, D. A. Dikin, R. D. Piner*, et al.*, *Synthesis of graphene-based nanosheets via chemical reduction of exfoliated graphite oxide*, Carbon **45**, 1558 (2007).
[95] S. Gilje, S. Han, M. Wang*, et al.*, *A Chemical Route to Graphene for Device Applications*, Nano Lett. **7**, 3394 (2007).
[96] A. Reina, X. Jia, J. Ho*, et al.*, *Large Area, Few-Layer Graphene Films on Arbitrary Substrates by Chemical Vapor Deposition*, Nano Lett. **9**, 30 (2009).
[97] C. Thomsen and S. Reich, *Double Resonant Raman Scattering in Graphite*, Phys. Rev. Lett. **85**, 5214 (2000).
[98] R. Narula and S. Reich, *Double resonant Raman spectra in graphene and graphite: A two-dimensional explanation of the Raman amplitude*, Phys. Rev. B **78**, 165422 (2008).
[99] G. M. Shedd and P. E. Russell, *The effect of low-energy ion impacts on graphite observed by scanning tunneling microscopy*, J. Vac. Sci. Technol. A **9**, 1261 (1991).
[100] J. R. Hahn, H. Kang, S. Song*, et al.*, *Observation of charge enhancement induced by graphite atomic vacancy: A comparative STM and AFM study*, Phys. Rev. B **53**, R1725 (1996).
[101] L. G. Cancado, K. Takai, T. Enoki*, et al.*, *General equation for the determination of the crystallite size La of nanographite by Raman spectroscopy*, Appl. Phys. Lett. **88**, 163106 (2006).
[102] D. V. McCaughan and V. T. Murphy, *Low-energy ion bombardment of silicon dioxide films on silicon*, J. Appl. Phys. **44**, 2008 (1973).
[103] E. Rossi and S. D. Sarma, *Ground State of Graphene in the Presence of Random Charged Impurities*, Phys. Rev. Lett. **101**, 166803 (2008).

[104] S. V. Morozov, K. S. Novoselov, M. I. Katsnelson, *et al.*, *Giant Intrinsic Carrier Mobilities in Graphene and Its Bilayer*, Phys. Rev. Lett. **100**, 016602 (2008).
[105] H. J. Hrostowski, F. J. Morin, T. H. Geballe, *et al.*, *Hall Effect and Conductivity of InSb*, Phys. Rev. **100**, 1672 (1955).
[106] T. Dürkop, S. A. Getty, E. Cobas, *et al.*, *Extraordinary Mobility in Semiconducting Carbon Nanotubes*, Nano Lett. **4**, 35 (2004).
[107] H. Suzuura and T. Ando, *Phonons and electron-phonon scattering in carbon nanotubes*, Phys. Rev. B **65**, 235412 (2002).
[108] G. Pennington and N. Goldsman, *Semiclassical transport and phonon scattering of electrons in semiconducting carbon nanotubes*, Phys. Rev. B **68**, 045426 (2003).
[109] V. Perebeinos, J. Tersoff, and P. Avouris, *Electron-Phonon Interaction and Transport in Semiconducting Carbon Nanotubes*, Phys. Rev. Lett. **94**, 086802 (2005).
[110] S. Ono and K. Sugihara, *Theory of the Transport Properties in Graphite*, J. Phys. Soc. Jpn. **21**, 861 (1966).
[111] X. Zhou, J.-Y. Park, S. Huang, *et al.*, *Band Structure, Phonon Scattering, and the Performance Limit of Single-Walled Carbon Nanotube Transistors*, Phys. Rev. Lett. **95**, 146805 (2005).
[112] M. Mohr, J. Maultzsch, E. Dobardzic, *et al.*, *Phonon dispersion of graphite by inelastic x-ray scattering*, Phys. Rev. B **76**, 035439 (2007).
[113] Z. Yao, C. L. Kane, and C. Dekker, *High-Field Electrical Transport in Single-Wall Carbon Nanotubes*, Phys. Rev. Lett. **84**, 2941 (2000).
[114] B. R. Bennett, R. Magno, J. B. Boos, *et al.*, *Antimonide-based compound semiconductors for electronic devices: A review*, Solid State Electron. **49**, 1875 (2005).
[115] V. Barone, O. Hod, and G. E. Scuseria, *Electronic Structure and Stability of Semiconducting Graphene Nanoribbons*, Nano Lett. **6**, 2748 (2006).
[116] S. R. Forrest, *The path to ubiquitous and low-cost organic electronic appliances on plastic*, Nature **428**, 911 (2004).
[117] J.-H. Ahn, H.-S. Kim, K. J. Lee, *et al.*, *Heterogeneous Three-Dimensional Electronics by Use of Printed Semiconductor Nanomaterials*, Science **314**, 1754 (2006).
[118] S. Yugang, M. Etienne, A. R. John, *et al.*, *Gigahertz operation in flexible transistors on plastic substrates*, Appl. Phys. Lett. **88**, 183509 (2006).
[119] E. McCann, *Asymmetry gap in the electronic band structure of bilayer graphene*, Phys. Rev. B **74**, 161403 (2006).
[120] K. S. Novoselov, E. McCann, S. V. Morozov, *et al.*, *Unconventional quantum Hall effect and Berry/'s phase of 2[pi] in bilayer graphene*, Nat. Phys. **2**, 177 (2006).
[121] T. Maeno, T. Futami, H. Kushibe, *et al.*, *Measurements and simulation of the spatial charge distribution in electron-beam-irradiated polymers*, *J. Appl. Phys.* **65**, 1147 (1989).

[122] E. R. Neagu, J. N. Marat-Mendes, R. M. Neagu*, et al.*, *Nonisothermal and isothermal discharging currents in polyethylene terephthalate at elevated temperatures*, J. Appl. Phys. **85**, 2330 (1999).

[123] D. Sadovnichii, A. Tuytnev, and Y. Milekhin, *Electron-beam charging of poly(methyl methacrylate)*, High Energy Chem. **39**, 148 (2005).

[124] G. M. Sessler and J. E. West, *Production of High Quasipermanent Charge Densities on Polymer Foils by Application of Breakdown Fields*, J. Appl. Phys. **43**, 922 (1971).

[125] T. Ando, A. B. Fowler, and F. Stern, *Electronic properties of two-dimensional systems*, Rev. Mod. Phys. **54**, 437 (1982).

[126] V. V. Cheianov and V. I. Fal'ko, *Selective transmission of Dirac electrons and ballistic magnetoresistance of n-p junctions in graphene*, Phys. Rev. B **74**, 041403 (2006).

[127] V. V. Cheianov, V. I. Fal'ko, and B. L. Altshuler, *The Focusing of Electron Flow and a Veselago Lens in Graphene p-n Junctions*, Science **315**, 1252 (2007).

[128] A. Konar, T. Fang, and D. Jena, *Effect of high-k dielectrics on charge transport in graphene*, Preprint at <http://arxiv.org/abs/0902.0819v1> (2009).

[129] A. J. Tunnell, V. W. Ballarotto, D. R. Hines*, et al.*, *Vertical Integration on Plastic Substrates using Transfer Printing*, Appl. Phys. Lett. **93**, 193113 (2008).

[130] Y.-W. Son, M. L. Cohen, and S. G. Louie, *Energy Gaps in Graphene Nanoribbons*, Phys. Rev. Lett. **97**, 216803 (2006).

[131] M. Ezawa, *Peculiar width dependence of the electronic properties of carbon nanoribbons*, Phys. Rev. B **73**, 045432 (2006).

[132] L. Brey and H. A. Fertig, *Electronic states of graphene nanoribbons studied with the Dirac equation*, Phys. Rev. B **73**, 235411 (2006).

[133] M. Y. Han, B. Ozyilmaz, Y. Zhang*, et al.*, *Energy Band-Gap Engineering of Graphene Nanoribbons*, Phys. Rev. Lett. **98**, 206805 (2007).

[134] Z. Chen, Y.-M. Lin, M. J. Rooks*, et al.*, *Graphene nano-ribbon electronics*, Physica E **40**, 228 (2007).

[135] X. Li, X. Wang, L. Zhang*, et al.*, *Chemically Derived, Ultrasmooth Graphene Nanoribbon Semiconductors*, Science **319**, 1229 (2008).

[136] X. Wang, Y. Ouyang, X. Li*, et al.*, *Room-Temperature All-Semiconducting Sub-10-nm Graphene Nanoribbon Field-Effect Transistors*, Phys. Rev. Lett. **100**, 206803 (2008).

[137] F. Sols, F. Guinea, and A. H. C. Neto, *Coulomb Blockade in Graphene Nanoribbons*, Phys. Rev. Lett. **99**, 166803 (2007).

[138] S. Y. Zhou, G. H. Gweon, A. V. Fedorov*, et al.*, *Substrate-induced bandgap opening in epitaxial graphene*, Nat. Mater. **6**, 770 (2007).

[139] G. Giovannetti, P. A. Khomyakov, G. Brocks*, et al.*, *Substrate-induced band gap in graphene on hexagonal boron nitride: Ab initio density functional calculations*, Phys. Rev. B **76**, 073103 (2007).

[140] X. Dong, Y. Shi, Y. Zhao*, et al.*, *Symmetry Breaking of Graphene Monolayers by Molecular Decoration*, Phys. Rev. Lett. **102**, 135501 (2009).

[141] D. W. Boukhvalov and M. I. Katsnelson, *Tuning the gap in bilayer graphene using chemical functionalization: Density functional calculations*, Phys. Rev. B **78**, 085413 (2008).
[142] J. B. Oostinga, H. B. Heersche, X. Liu*, et al.*, *Gate-induced insulating state in bilayer graphene devices*, Nat. Mater. **7**, 151 (2008).
[143] V. C. Tung, M. J. Allen, Y. Yang*, et al.*, *High-throughput solution processing of large-scale graphene*, Nat. Nanotechnol. **4**, 25 (2009).
[144] D. Li, M. B. Muller, S. Gilje*, et al.*, *Processable aqueous dispersions of graphene nanosheets*, Nat. Nanotechnol. **3**, 101 (2008).
[145] C. Valles, C. Drummond, H. Saadaoui*, et al.*, *Solutions of Negatively Charged Graphene Sheets and Ribbons*, J. Am. Chem. Soc. **130**, 15802 (2008).
[146] E. W. Hill, A. K. Geim, K. Novoselov*, et al.*, *Graphene Spin Valve Devices*, IEEE Trans. Magn. **42**, 2694 (2006).
[147] K. Tsukagoshi, B. W. Alphenaar, and H. Ago, *Coherent transport of electron spin in a ferromagnetically contacted carbon nanotube*, Nature **401**, 572 (1999).
[148] V. Falko, *Quantum information on chicken wire*, Nat. Phys. **3**, 151 (2007).
[149] T. Dürkop, B. M. Kim, and M. S. Fuhrer, *Properties and applications of high mobility semiconducting nanotubes*, J. Phys.: Condens. Matter **16**, R533 (2004).
[150] C. L. Kane and E. J. Mele, *Quantum Spin Hall Effect in Graphene*, Phys. Rev. Lett. **95**, 226801 (2005).
[151] D. Huertas-Hernando, F. Guinea, and A. Brataas, *Spin relaxation times in disordered graphene*, Eur.Phys.J.,Special Toppics **148**, 177 (2007).
[152] N. Tombros, C. Jozsa, M. Popinciuc*, et al.*, *Electronic spin transport and spin precession in single graphene layers at room temperature*, Nature **448**, 571 (2007).
[153] S. Cho, Y.-F. Chen, and M. S. Fuhrer, *Gate-tunable graphene spin valve*, Appl. Phys. Lett. **91**, 123105 (2007).
[154] V. M. Karpan, G. Giovannetti, P. A. Khomyakov*, et al.*, *Graphite and Graphene as Perfect Spin Filters*, Phys. Rev. Lett. **99**, 176602 (2007).
[155] P. S. Cornaglia, G. Usaj, and C. A. Balseiro, *Localized Spins on Graphene*, Phys. Rev. Lett. **102**, 046801 (2009).
[156] E. V. Castro, K. S. Novoselov, S. V. Morozov*, et al.*, *Biased Bilayer Graphene: Semiconductor with a Gap Tunable by the Electric Field Effect*, Phys. Rev. Lett. **99**, 216802 (2007).
[157] K. Nakada, M. Fujita, G. Dresselhaus*, et al.*, *Edge state in graphene ribbons: nanometer size effect and edge shape dependence*, Phys. Rev. B **54**, 17954 (1996).
[158] S. V. Morozov, K. S. Novoselov, M. I. Katsnelson*, et al.*, *Strong suppression of weak localization in graphene*, Phys. Rev. Lett. **97**, 016801 (2006).
[159] Y. Niimi, T. Matsui, H. Kambara*, et al.*, *Scanning tunneling microscopy and spectroscopy of the electronic local density of states of graphite surfaces near monoatomic step edges*, Phys. Rev. B **73**, 085421 (2006).
[160] T. O. Wehling, A. V. Balatsky, M. I. Katsnelson*, et al.*, *Local electronic signatures of impurity states in graphene*, Phys. Rev. B **75**, 125425 (2007).

[161] R. Jayaraman and C. G. Sodini, *A 1/f Noise Technique to Extract the Oxide Trap Density Near the Conduction Band Edge of Slicon*, IEEE Trans. Elec. Dev. **36**, 1773 (1989).
[162] J. C. Meyer, A. K. Geim, M. I. Katsnelson*, et al.*, *On the roughness of single- and bi-layer graphene membranes.*, Solid State Commun. **143**, 101 (2007).
[163] W. K. Kim, H. C. Choi, M. Shim*, et al.*, *Synthesis of ultralong and high percentage of semiconducting single-walled carbon nanotubes*, Nano Lett. **2**, 703 (2002).
[164] H. Marsh and Warburto.Ap, *Catalysis of Graphitisation*, J. Appl. Chem. U.S.S.R. **20**, 133 (1970).
[165] S. Morita, R. Wiesendanger, and E. Meyer, (Springer-Verlag, Berlin, 2002).
[166] L. C. Venema, V. Meunier, P. Lambin*, et al.*, *Atomic structure of carbon nanotubes from scanning tunneling microscopy*, Phys. Rev. B **61**, 2991 (2000).
[167] D. Tomanek, S. G. Louie, H. J. Mamin*, et al.*, *Theory and observation of highly asymmetric atomic structure in scanning-tunneling-microscopy images of graphite*, Phys. Rev. B **35**, 7790 (1987).
[168] C. L. Kane and E. J. Mele, *Broken symmetries in scanning tunneling images of carbon nanotubes*, Phys. Rev. B **59**, R12759 (1999).
[169] J. Krim, I. Heyvaert, C. V. Haesendonck*, et al.*, *Scanning Tunneling Microscopy Observation of Self-Affine Fractal Roughness in Ion-Bombarded Film Surfaces*, Phys. Rev. Lett. **70**, 57 (1993).
[170] G. Palasantzas, D. Tsamoras, and J. T. M. De Hosson, *Roughening aspects of room temperature vapor deposited oligomer thin films onto Si substrate*, Surf. Sci. **507-10**, 357 (2002).
[171] A. Krishnan, E. Dujardin, T. W. Ebbesen*, et al.*, *Young's modulus of single-walled nanotubes*, Phys. Rev. B **58**, 14013 (1998).
[172] N. G. Chopra, L. X. Benedict, V. H. Crespi*, et al.*, *Fully collapsed carbon nanotubes*, Nature **377**, 135 (1995).
[173] J. Sabio, C. Seoanez, S. Fratini*, et al.*, *Electrostatic interactions between graphene layers and their environment*, Phys. Rev. B **77**, 195409 (2008).
[174] V. Geringer, M. Liebmann, T. Echtermeyer*, et al.*, *Intrinsic and extrinsic corrugation of monolayer graphene deposited on SiO2*, Phys. Rev. Lett. **102**, 076102 (2009).
[175] S. Adam, E. H. Hwang, and S. Das Sarma, *Scattering mechanisms and Boltzmann transport in graphene*, Physica E: Low-dimensional Systems and Nanostructures **40**, 1022 (2008).
[176] N. M. R. Peres, F. Guinea, and A. H. Castro Neto, *Coulomb interactions and ferromagnetism in pure and doped graphene*, Phys. Rev. B **72**, 174406 (2005).
[177] K. Nomura and A. H. MacDonald, *Quantum Hall Ferromagnetism in Graphene*, Phys. Rev. Lett. **96**, 256602 (2006).
[178] H. Min, R. Bistritzer, J.-J. Su*, et al.*, *Room-temperature superfluidity in graphene bilayers*, Phys. Rev. B **78**, 121401 (2008).

[179] Y. Zhang, V. W. Brar, F. Wang, *et al.*, *Giant phonon-induced conductance in scanning tunnelling spectroscopy of gate-tunable graphene*, Nat. Phys. **4**, 627 (2008).

[180] D. Jena and A. Konar, *Enhancement of Carrier Mobility in Semiconductor Nanostructures by Dielectric Engineering*, Phys. Rev. Lett. **98**, 136805 (2007).

[181] S. Das Sarma and B. Vinter, *Effect of impurity scattering on the distribution function in two-dimensional Fermi systems*, Phys. Rev. B **24**, 549 (1981).

[182] Z. Jiang, E. A. Henriksen, L. C. Tung, *et al.*, *Infrared Spectroscopy of Landau Levels of Graphene*, Phys. Rev. Lett. **98**, 197403 (2007).

[183] V. F. Petrenko and R. W. Whiteworth, *The Physics of Ice* (Oxford University Press, Oxford, U.K., 1999).

[184] P. C. Sanfelixa, S. Hollowaya, K. W. Kolasinskib, *et al.*, *The structure of water on the (0 0 0 1) surface of graphite*, Surf. Sci. **532**, 166 (2003).

[185] P. A. Thiel and T. E. Madeyb, *The interaction of water with solid surfaces: Fundamental aspects*, Surf. Sci. Rep. **7**, 211 (1987).

[186] B. Huard, N. Stander, J. A. Sulpizio, *et al.*, *Evidence of the role of contacts on the observed electron-hole asymmetry in graphene*, Phys. Rev. B **78**, 121402 (2008).

[187] J. Martin, N. Akerman, G. Ulbricht, *et al.*, *Observation of electron-hole puddles in graphene using a scanning single-electron transistor*, Nat. Phys. **4**, 144 (2008).

[188] D. Marton, H. Bu, K. J. Boyd, *et al.*, *On the defect structure due to low energy ion bombardment of graphite*, Surf. Sci. **326**, L489 (1995).